ELECTRON-TRANSFER REORGANIZATION ENERGIES OF ISOLATED MOLECULES

Thesis by

Xenia Amashukeli

In Partial Fulfillment of the Requirements

for the Degree of Doctor of Philosophy

California Institute of Technology

Pasadena, California

2002

(Submitted May 6, 2002)

Acknowledgment

I would like to thank my academic advisor, Prof. Harry Gray, for his perpetual support of my research, and for generating such an enthusiastic and stimulating work environment. I am grateful to Prof. Geoffrey Blake for an opportunity to work in his laboratory. Also, I would like to thank Prof. William Goddard for letting me be a SURF student in his group, where I learned computational chemistry.

I would have never become a chemist, if it were not for amazing high school science and math teachers, whose enthusiasm was so contagious that I gave up humanities. In particular, I am grateful to Fred Sculco and Bob Kern from Noble&Greenough. I feel lucky that I was able to pursue my interest in science at Brown. I am grateful to all of Chemistry Department Faculty, who pushed me toward choosing a chemistry option instead of physics. I would like to thank my undergraduate advisor, Prof. Peter Weber, and all of the graduate students in Weber lab, who showed me how to work and think as an independent scientists.

I would like to thank all of my research collaborators. In particular, Prof. Dennis Lichtenberger and his research group at the University of Arizona. Nadine introduced me to the world of photoelectron spectroscopy, and I am very grateful to her for letting me play with their instruments.

I feel lucky to have interacted with so many talented researchers at Caltech. I would like to thank Randy for teaching me organic synthesis when I fist joined the group. I gratefully acknowledge Alex Dunn for many helpful discussions, and for being a wonderful person to share a lab with in the BI. I thank Mike Green for all his help with computational

chemistry. I am grateful to Jay Winkler for the time he spend teaching me laser spectroscopy. Finally, I thank Larry and Mike for their introduction to X-ray crystallography.

In the end, I have many people to thank who are responsible for my happiness during graduate school. The Gray group has been an interesting bunch of people to work with. My spacial thanks go to Joe and Joanna Swayze, who were my American family when I first moved to Boston and who continue to inspire me to do exciting things other than science. I thank Claudine for being a true friend for the last five years. I am in debt to my Mom, Dad, and Grandmother for their love and support. Finally, I want to acknowledge Adrian for all of his encouragement and understanding, and for inspiring and believing in me.

Abstract

Electron-transfer reorganization energies of isolated organic molecules and biologically relevant porphyrins are obtained from analyses of their photoelectron spectra. The assignments of experimental ionization energies are aided by *ab initio* calculations, and comparisons between He I and He II ionization data. It is established that in unsymmetrically substituted metalloporphyrins, i.e., Zn(II) protoporphyrin IX, the highest occupied molecular orbital has appreciable nitrogen character (Chapter 3). Quantum-mechanical and semiclassical analyses of vibrational progressions observed in photoelectron spectra yield gas-phase reorganization energies. Favorable agreement is reached between experimental and calculated values of reorganization energies (Chapters 2 and 3). This observation is not surprising, however, since density functional theory calculations, employed in this thesis, are successful at reproducing experimental molecular geometries. Indeed, X-ray structural parameters of dibenzo[a,c]phenazine are in excellent agreement with calculated results (Chapter 6). Vibrational frequencies of organic molecules are also calculated (Chapter 5) to aid mode-specific quantum-mechanical analyses of fine structure observed in photoelectron spectra. Given the success of *ab initio* calculations of reorganization energies of organic molecules, the same computational approach is employed to obtain reorganization energies of six-coordinate metalloporphyrin model systems (Chapter 4). The results show that large reorganization energies are associated with charged ligands, which are most frequently found in protein redox catalytic sites; small reorganization energies, on the other hand, are calculated for the molecules with neutral ligands, commonly located in the protein active sites that facilitate electron transfer.

Table of Contents

Chapter 1

Introduction

Review of Electron-Transfer Theoretical Models

According to classical Marcus theory,[1] the rates of electron-transfer (ET) reactions depend on three parameters: the standard free energy change, ΔG^0, the preexponential frequency, A, and the reorganization energy, λ (where $\lambda = \lambda_o + \lambda_i$, the outer- and inner-sphere contributions).[1] In the semiclassical theory, when long-distance intramolecular ET reactions are considered,[2] A is defined in terms of the electronic coupling matrix element, H_{AB} (Eq. 1.1):[3]

$$k_{ET} = \left(\frac{4\pi^3}{h^2 \lambda k_B T}\right)^{1/2} (H_{AB})^2 \exp\left(\frac{-(\Delta G^0 + \lambda)^2}{4\lambda k_B T}\right), \qquad \text{Eq. 1.1}$$

where h is a Planck's constant, k_B is a Boltzmann's constant, and T is temperature. The inner-sphere reorganization energy, λ_i, is estimated from the intramolecular vibrational force constants, f_i, and the change in the equilibrium positions between reactants and products, $\Delta q_{e,i}$, (Eq. 1.2):[1]

$$\lambda_i = \frac{1}{2} \sum_i f_i \Delta q_{e,i}^2 \qquad \text{Eq. 1.2}$$

The semiclassical expression (Eq. 1.1) is often used to describe the electron tunneling model of ET, where all nuclear coordinates are treated classically. According to this model, the rates of ET reactions greatly depend on the magnitude of H_{AB} (Figure 1.1). The value of H_{AB} is exponentially dependent on the distance between electron donors and acceptors in a chemical system.[4]

In the nuclear tunneling model,[5] both solvent and intramolecular coordinates are either

Figure 1.1. Plot of free energy vs. reaction coordinate for an ET reaction. The splitting at the intersection of the reactant and product potential energy curves is $2H_{AB}$, where H_{AB} is the electronic coupling matrix element. The reaction free energy is designated as ΔG^0.

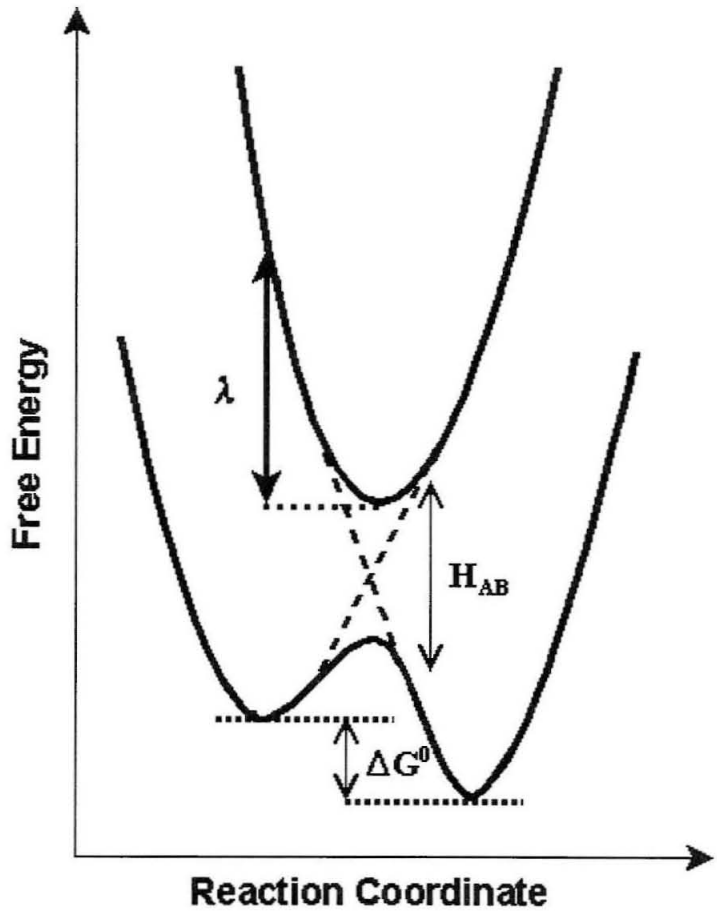
Free Energy
λ
H_{AB}
ΔG^0
Reaction Coordinate

treated quantum-mechanically or the inner-sphere coordinates are treated quantum-mechanically and solvent modes are treated classically. In the latter case (where $k_BT \ll \hbar\varpi$), the ET rate constant is given in Eq. 1.3:[6]

$$k_{ET} = \frac{2\pi}{\hbar(4\pi\lambda_o k_B T)^{1/2}}(H_{AB})^2 \sum_n |\langle 0|n\rangle|^2 \exp\left(\frac{-(\Delta G^0 - n\hbar\varpi + \lambda_o)^2}{4\lambda_o k_B T}\right), \quad \text{Eq. 1.3}$$

where n is a vibrational state, and ϖ is a vibrational frequency. In this model, the rates of ET reactions depend also on the magnitude of Franck-Condon factors (Eq. 1.4).[6]

$$|\langle 0|n\rangle|^2 = \left(\frac{S^n}{n!}\right)\exp(-S) \quad \text{Eq. 1.4}$$

S is a distortion parameter which is related to λ_i according to Eq. 1.5:[7]

$$\lambda_i = \sum_k S_k \hbar\varpi_k, \quad \text{Eq. 1.5}$$

where ϖ_k is the vibrational frequency of mode k. In solution, the experimental values of S are estimated from fine structure analyses of UV-visible spectra (e.g., fluorescence).

Inner-Sphere Reorganization Energies in Solution

In solution, reorganization energies (λ_o and λ_i) can be obtained from band-shape analyses of UV-visible spectra. These analyses, however, are usually complicated by the presence of solvent (i.e., the vibrational progressions are either poorly resolved or not

observed at all). In cases when fine structure is present, the fit yields values of S, which are then related to the inner-sphere reorganization energies (Eq. 1.5).[8] More frequently, however, vibrational structure is not observed; thus, the spectral bands are fit differently, and the reorganization energies are obtained indirectly (i.e., an average value for the intramolecular vibrational frequency is assumed).[9] For example, the stationary fluorescence spectra for the radiative charge transfer recombination in a series of barrelene-based molecules have been measured; the reorganization energies have been evaluated from fits of standard Franck-Condon factors[10] to the entire fluorescence band shape.[11] In the analysis, a single high-frequency intramolecular mode ($\hbar\varpi$= 1300 cm^{-1}) was successfully utilized in conjunction with solvent modes, yielding a satisfactory fit of the band shape. However, this analysis produced reorganization energies in nonpolar solvents that were unphysically large. The authors had to include an intramolecular medium mode ($\hbar\varpi$ = 500 cm^{-1}) to obtain reasonable values of λ_o and λ_i.

Gas-Phase ET

Review of Charge-Shift Reactions

In the absence of solvent, the interaction between inner-sphere and solvent modes is replaced by the coupling between intramolecular vibronic levels of charge-localized (CL) and charge-separated (CS) states of the molecule.[12] This substitution is valid when the ground electronic level of CS is quasi-degenerate with the CL electronic states. Therefore, the rate

of gas-phase ET is the same as the rate of intramolecular radiationless transition, a commonly encountered photophysical process (e.g., internal conversion or intersystem crossing).[13] Importantly, there is Coulombic interaction between positively and negatively charged parts in the CS molecule, which in most cases is energetically unfavorable for the formation of CS species in the gas phase.[14] Therefore, most of the experimental gas-phase ET work has been focused on charge-shift reactions in donor-bridge-acceptor (DBA) systems, $DBA^+ \rightarrow D^+BA$, because in these molecules there is no Coulombic interaction between donor and acceptor (Figure 1.2). Two examples of gas-phase charge-shift reactions in DBA and in peptides are described below.

Resonantly enhanced two photon ionization (RE2PI) method has been successfully used by Levy *et al.* to generate a positive charge on D.[15] The dynamics of the ionic state was then probed by resonantly fragmenting molecules with a second laser pulse. The changes in the absorption spectrum of an ion were monitored as a function of the time delay between the two laser pulses. It was possible to observe definite changes in the spectrum (i.e., from the donor- to the acceptor-like), but the limits of time resolution (2 ns) prevented the extraction of any kinetics data from these measurements.

Schlag *et al.* have examined ET in peptide cations in the gas phase, showing that the amino acid composition has an impact on the efficiency of ET processes.[16] Similar to DBA studies, peptide cations are formed by UV RE2PI of aromatic chromophores. In the cations, ET is initiated by absorption of a first visible photon, and probed by a second visible photon. As in the case of DBA, the process is monitored by dissociation. Schlag *et al.* concluded that charge transfer is a through-bond process, involving energetically accessible electronic states

Figure 2.1. Schematic representation of a charge-shift reaction, DBA → DBA^+ → ^+DBA, in gas phase. Acceptor, A, energy levels are red. Donor, D, energy levels are green. A is selectively ionized in RE2PI ($h\nu_1$) experiment. The energy of the first excited state of A, $S_1(A)$, is half that of the ionization energy of A, IE(A). The ionization energy of D, IE(D), is less or equal to IE(A). The first excited state of D, $S_1(D)$, is higher in energy than $S_1(A)$ to insure selective ionization of A. ET from D to A is monitored by dissociation ($h\nu_2$).

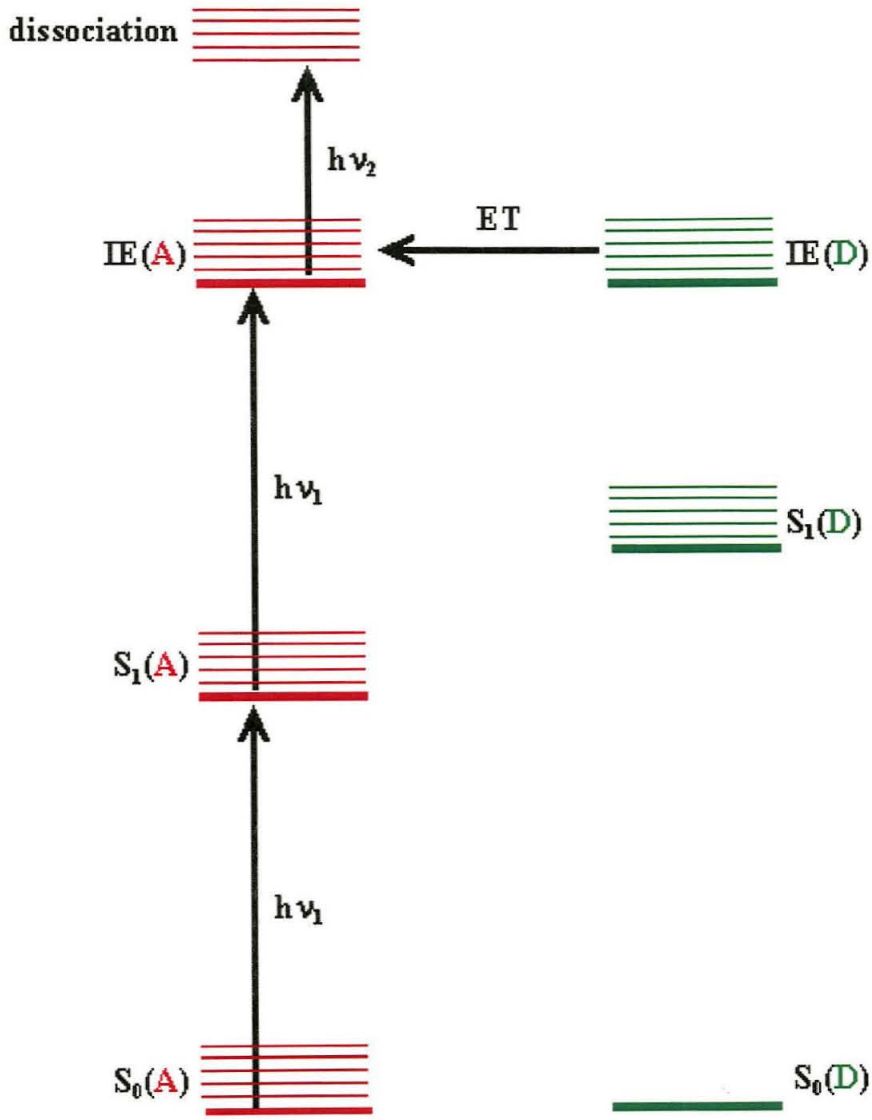
dissociation
hν2
IE(A)
ET
IE(D)
hν1
S1(D)
S1(A)
hν1
S0(A)
S0(D)

along the reaction path. Once again, the rates of the reactions were not recorded.

Reorganization Energies of Isolated Molecules

Our work has been focused on the determination of ET reorganization energies of isolated organic and biological molecules. While solution studies often produced accurate estimates of average inner-sphere reorganization energies, gas-phase experiments have yielded exact (i.e., mode specific) values of λ.[17] The experimental technique employed for these gas-phase ET studies is photoelectron spectroscopy (PES). In valence PES, molecules are irradiated with high-energy He Iα ($1s^2 \leftarrow 1s^1 2p^1$, 21.218 eV) and He II$\alpha$ ($1s^1 \leftarrow 2p^1$, 40.814 eV) photons. The kinetic energies of ejected electrons are recorded by a hemispherical analyzer and related to ionization energies according to Eq. 1.6:[18]

$$h\nu = IE + \frac{1}{2}mv^2 \qquad \text{Eq. 1.6}$$

The principal components of a photoelectron spectrometer are shown in Figure 1.3.

In PES, the relative populations of the vibrational states are described by the Maxwell-Boltzmann distribution law. In adiabatic approximation, the electronic part, $\Psi(r, Q)$, of the ground (i.e., neutral) state wave equation is a solution to the electronic Schrödinger equation (Eq. 1.7):[19]

$$\hat{H}_E \Psi(r,Q) = E(Q)\Psi(r,Q), \qquad \text{Eq.1.7}$$

where H_E is an electronic hamiltonian, and E is an eigenvalue. Both $\Psi(r, Q)$ and $E(Q)$ parametrically depend on the nuclear position, Q, and are continuos functions of the $3N$

Figure 1.3. Top: Schematic representation of a photoelectron spectrometer. Bottom: Principal components of a hemispherical analyzer employed in PES experiments.

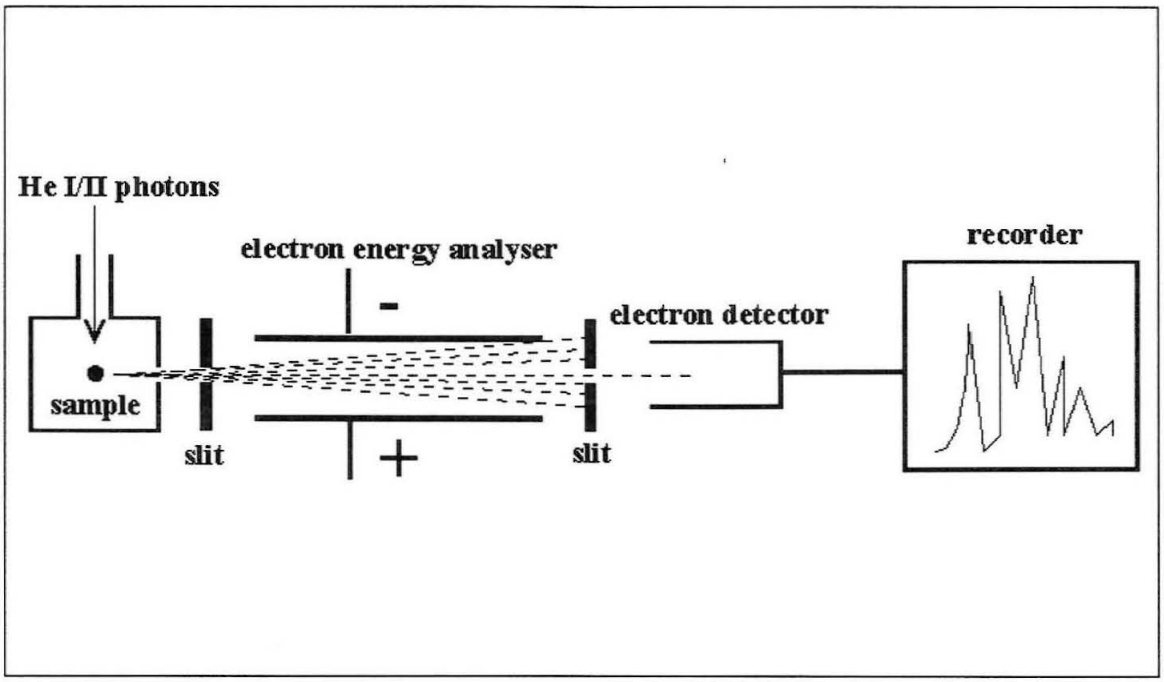
He I/II photons
electron energy analyser
recorder
electron detector
sample
slit
slit

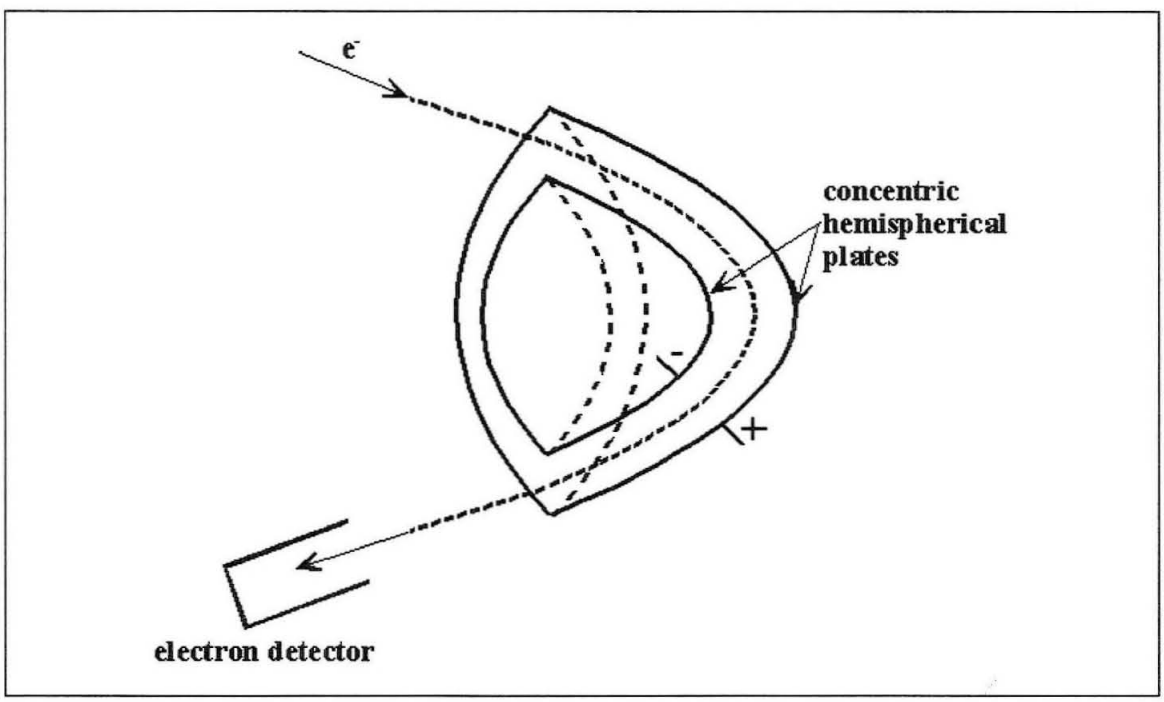
e⁻
concentric
hemispherical
plates
electron detector

nuclear coordinates. The nuclear part of the ground state wave equation is a function of $3N$-6 internal molecular vibrations defined by the symmetry-adapted vibrational coordinates. In the cation state,[20] the electronic functions are the solutions to the electronic hamiltonian similar to the one used for the ground state. This approximation is known as the Franck-Condon principle.[21] The physical basis for the Franck-Condon principle is that the time scale of electronic motion, 10^{-16} s, is much shorter than that of nuclear motion, 10^{-14} s. Since the internuclear distances do not change significantly during ionization, the high-intensity bands in the photoelectron spectrum correspond to the vertical ionization energies (Figure 1.4). Since ionization transitions can take place between different vibrational levels of the ground and cation states, the total ionization intensity is distributed over the vibrational line structure of the photoelectron band.

When the equilibrium nuclear positions of the ground and cation states are nearly the same, the vertical ionization corresponds to the 0-0 vibrational transition (i.e., adiabatic transition) (Figure 1.5). In the laboratory, this is commonly observed in small, highly volatile molecules.[22] More frequently, however, the removal of an electron from a molecule results in a significant change of molecular geometry; thus the equilibrium nuclear position of the cation state is shifted relative to that of the ground state. In addition, large molecules (typically solids) do not sublime at low temperatures (i.e., below 25 °C), which results in thermal population of their excited vibrational states. Vertical ionizations in these cases correspond to other than 0-0 vibrational transitions (Figure 1.5).

The intensities of the individual vibrational bands in the vibrational progression are defined by the square of vibrational overlap integrals (Eq. 1.4). Photoelectron spectra of

Figure 1.4. Schematic depiction of PES at 300 K. Arrows represent vertical ionizations.

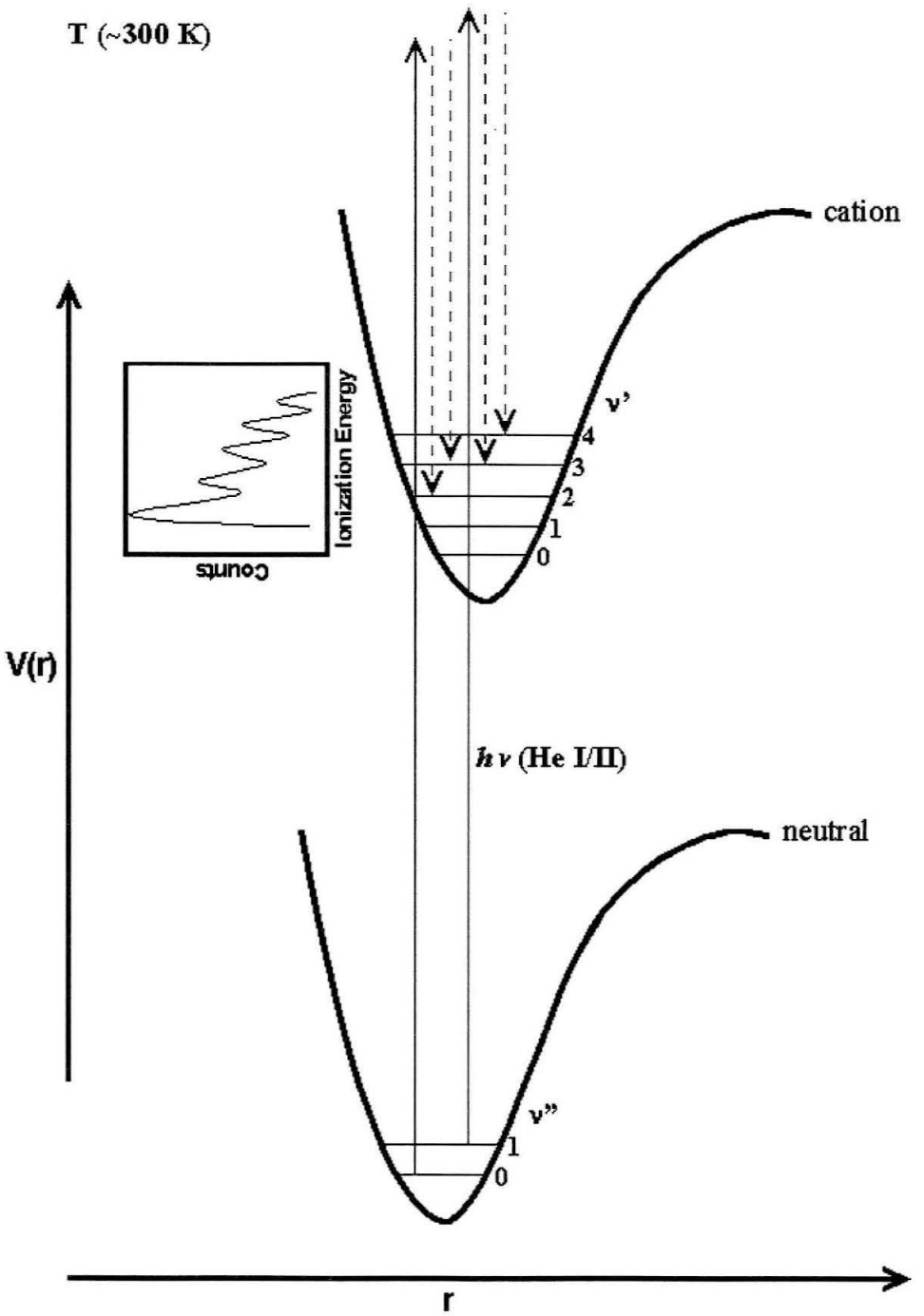
T (~300 K)
cation
neutral
V(r)
r
Ionization Energy
Counts
ν'
ν"
4
3
2
1
0
1
0
hν (He I/II)

Figure 1.5. Top: Franck-Condon principle applied to a case in which $r_n < r_c$ and 3-0 transition is the most probable. Bottom: Typical vibrational progression intensity distributions: (a) adiabatic, 0-0 transition, and (b) vertical, 3-0 transition.

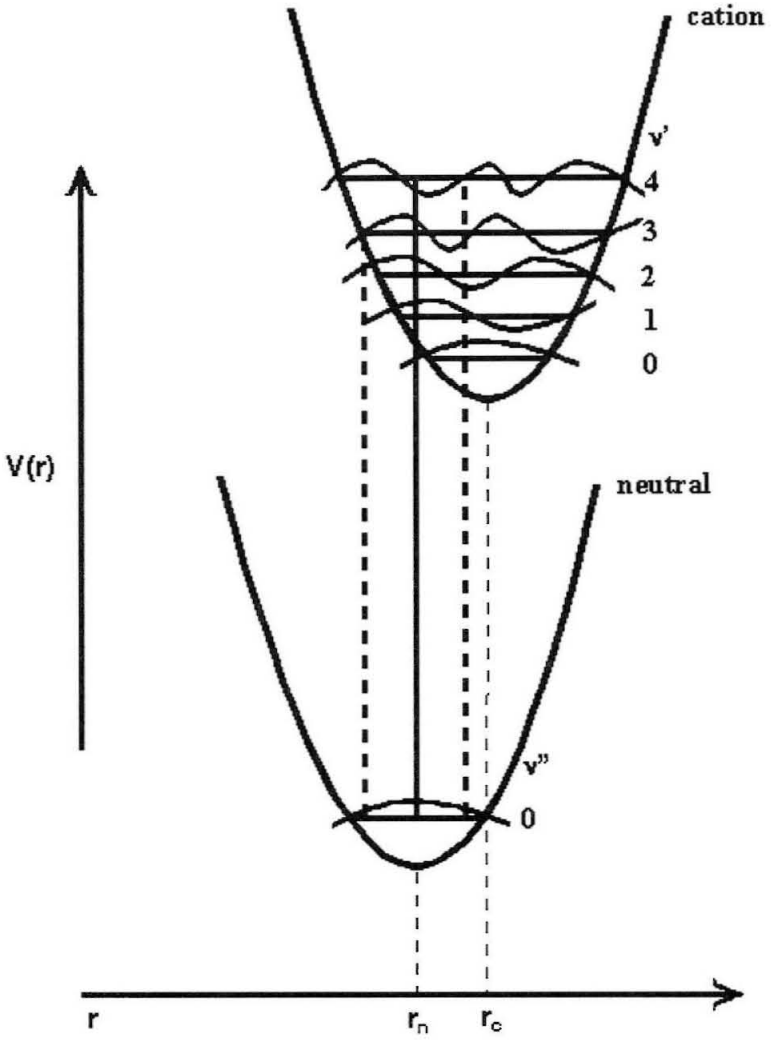
cation
v'
4
3
2
1
0
V(r)
neutral
v"
0
r
r_n
r_c

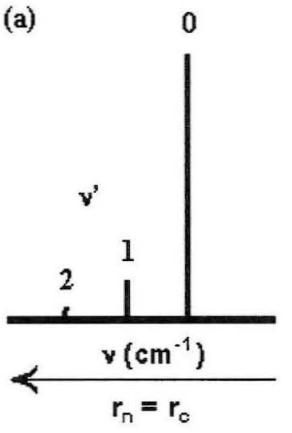
(a)
0
v'
1
2
ν (cm^{-1})
$r_n = r_c$

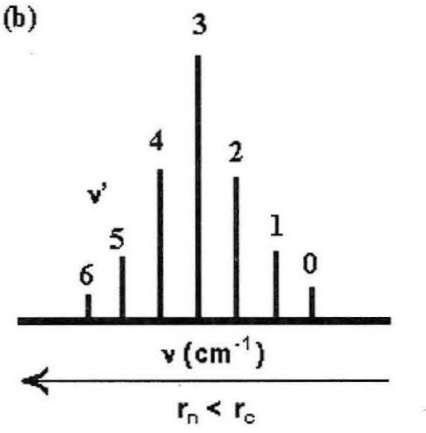
(b)
3
4
2
v'
1
5
0
6
ν (cm^{-1})
$r_n < r_c$

molecules often exhibit vibrational progressions, and the extent of the molecular geometry change can be established from vibrational band-shape analyses. As will be described in detail in Chapters 2 and 3, the vibrational progressions can be fit to a Poisson distribution function, yielding values of S (this procedure is known as a quantum-mechanical analysis of the fine structure).[21] The low-frequency modes and slight changes in the vibrational frequencies between the neutral and cation states contribute to the spectral broadening, which is treated semiclassically.[21] The sum of quantum-mechanical and semiclassical reorganization energies is the gas-phase ET reorganization energy. If the coupling between solvent and intramolecular vibrational modes is weak, the gas-phase λ is virtually the same as the solution λ_i.[17]

References and Notes

(1) Marcus, R. A. *J. Chem. Phys.* **1956**, *24*, 966-978.

(2) (a) Winkler, J. R.; Gray, H. B. *Chem. Rev.* **1992**, *92*, 369-379. (b) Balzani, V., Ed. *Electron Transfer in Chemistry*; Wiley-VCH Verlag: Germany, **2001**.

(3) (a) Hopfield, J. J., Ed. *Oxidases and Related Redox Systems*; Pergamon Press: Oxford, **1982**; pp. 3-19. (b) Hopfield, J. J., Ed. *Electrical Phenomena at the Biological Membrane Level*; Elsevier: New York, **1977**; pp. 471-492.

(4) (a) McConnell, H. M. *J. Chem. Phys.* **1961**, *35*, 508-515. (b) Liang, C.; Newton, M. D. *J. Phys. Chem.* **1992**, *96*, 2855-2866. (c) Liang, C.; Newton, M. D. *J. Phys. Chem.*

1993, *97*, 3199-3211. (d) Broo, A.; Larsson, S. *Chem. Phys.* **1990**, *148*, 103-115. (e) Curtiss, L. A.; Naleway, C. A.; Miller, J. R. *Chem. Phys.* **1993**, *176*, 387-405. (f) Jordan, K. D.; Padden-Row, M. N. *Chem. Rev.* **1992**, *92*, 395-410.

(5) (a) Siders, P.; Marcus, R. A. *J. Am. Chem. Soc.* **1981**, *103*, 741-747. (b) Siders, P.; Marcus, R. A. *J. Am. Chem. Soc.* **1981**, *103*, 748-752.

(6) (a) Vorotyntsev, M. A.; Dogonadze, R. R.; Kuznetsov, A. M. *Phys. Status Solidi* **1972**, *B54*, 125. (b) Vorotyntsev, M. A.; Dogonadze, R. R.; Kuznetsov, A. M. *Phys. Status Solidi* **1972**, *B54*, 425. (c) Dogonadze, R. R.; Kuznetsov, A. M.; Vorotyntsev, M. A. *Phys. J. Electroanal. Chem.* **1977**, *75*, 315.

(7) Brunschwing, B. S.; Sutin, N. *Comments Inorg. Chem.* **1987**, *6*, 209-235.

(8) Winkler, J. R.; Gray, H. B. *Inorg. Chem.* **1985**, *24*, 346-355.

(9) Miller, J. R.; Closs, G. L. *Science* **1988**, *240*, 440-447.

(10) The authors used standard distortion parameters to fit experimental data; and the use of "Franck-Condon factors" expression is incorrect.

(11) Cortés, J.; Heitele, H.; Jortner, J. *J. Phys. Chem.* **1994**, *98*, 2527-2536.

(12) Levy, D. H. *Advances in Chemical Physics*; John Wiley Inc: New York, **1999**; Vol. 106.

(13) Bixon, M.; Jortner, J. *J. Chem. Phys.* **1968**, *48*, 715-726.

(14) Jortner, J. *J. Chem. Phys.* **1976**, *64*, 4860-4867.

(15) Chattoraj, M.; Laursen, S. L.; Paulson, B.; Chung, D. D.; Closs, G. L.; Levy, D. H. *J. Chem. Phys.* **1992**, *96*, 8778-8784.

(16) Weinkauf, R,; Schanen, P.; Metsala, A.; Schlag, E. W.; Bürgle, M.; Kessler, H.

J. Phys. Chem. **1996**, *100*, 18567-18585.

(17) Consult Chapters 2 (Amashukeli, X.; Winkler, J. R.; Gray, H. B.; Gruhn, N. E.; Lichtenberger, D. L. *J. Phys. Chem.* **2002**, in press) and 3 for the experimental results and discussion.

(18) Hollas, J. M. *Modern Spectroscopy*; John Wiley Inc: New York, **1996**; p. 255.

(19) Born M.; Huang, K. *Dynamical Theory of Crystal Lattice*; Oxford University Press: New York, **1954**.

(20) Any of the states that are generated after the removal of an electron from the ground state.

(21) Ballhausen, C. J. *Molecular Electronic Structures of Transition Metal Complexes*; McGraw-Hill: U.K., **1979**; p.125.

(22) See ref. 18, Ch. 8.

Chapter 2

Electron-Transfer Reorganization Energies of Isolated Organic Molecules[†]

[†] Adapted from X. Amashukeli, J. R. Winkler, H. B. Gray, N. E. Gruhn, D. L. Lichtenberger, *J. Phys. Chem. B* (2002), in press.

Acknowledgments:

This work would not have been possible without the Gas-Phase Photoelectron Spectroscopy facilities at the University of Arizona, and the Molecular Simulation Center at Caltech.

Introduction

Electron-transfer reactions are key steps in a vast array of chemical and biological processes.[1] According to semiclassical theory, the rates of these reactions in solution are governed by three fundamental parameters: the reorganization energy, λ (where $\lambda = \lambda_i + \lambda_o$, the inner- and outer-sphere contributions); the electronic coupling matrix element, H_{AB}; and the standard free energy change, ΔG^0.[2] Both theoretical and experimental investigations suggest that the solvent contribution (λ_o) to the reorganization energy is much larger in most cases than the inner-sphere contribution (λ_i). It also has been shown that the ratio λ_o/λ_i decreases with decreasing solvent polarity.[3] The limiting case is a reaction in the absence of bulk solvent, as occurs in the gas phase.[4]

Reorganization energies were extracted from analyses of the photoelectron spectra of six isolated organic molecules: phenanthrene (**1**), 1,10-phenanthroline (**2**), phenazine (**3**), dibenzo[a,c]anthracene (**4**), dibenzo[a,c]phenazine (**5**), and dipyrido[3,2-a;2'3'-c]phenazine (**6**) (Scheme 2.1). These particular molecules were selected because they are often employed as redox active components in donor-bridge-acceptor systems.[5]

Materials and Methods

Molecules

Molecules **1** though **4** were obtained from Aldrich and were used without further

Scheme 2.1. Molecules employed in this study.

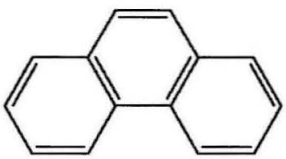

1

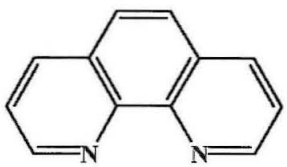

2

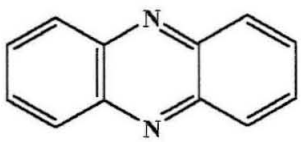

3

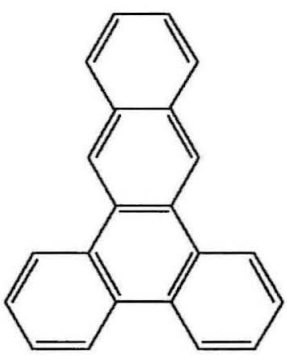

4

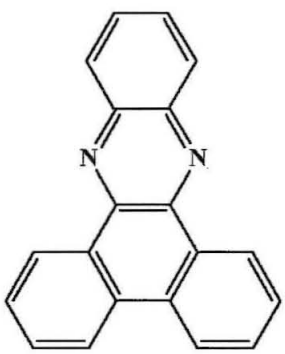

5

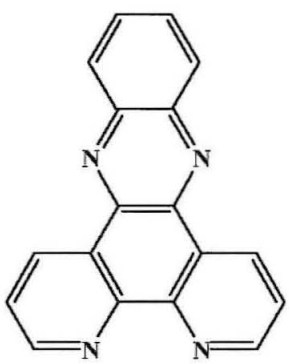

6

purification. **5** was prepared by refluxing 9,10-phenanthrenequinone (3 mmol) and 1,2-diaminobenzene (3 mmol) in dry methanol. A sample of **6** was kindly provided by Sarah Delaney (Caltech).

Photoelectron Spectroscopy

He I photoelectron spectra were recorded using an instrument with a 36 cm diameter, 8 cm gap hemispherical analyzer (McPherson). The ionization source, detection, and control electronics have been described in detail elsewhere.[6,7] The ionization energy scale was calibrated using the $^2E_{1/2}$ ionization of methyl iodide (9.538 eV), with the Ar $^2P_{3/2}$ ionization (15.759 eV) used as an internal energy scale lock during data collection. During data collection, the instrument resolution, measured as full-width-at-half-maximum of the Ar $^2P_{3/2}$ ionization, was 0.019–0.025 eV for **1**–**4**, **6** and 0.033 eV for **5**. Since He I discharge source is not monochromatic,[8] the spectra collected with He Iα ($1s^2 \leftarrow 1s2p$, 21.218 eV) source were corrected for He Iβ line ($1s^2 \leftarrow 1s3p$, 23.085 eV, and 3% of the intensity of the He Iα line). Data collection temperatures at ~10^{-4} torr (monitored using a "K" type thermocouple passed through a vacuum feed and attached directly to the ionization cell): phenanthrene, 47–58 °C; 1,10-phenanthroline, 102–108 °C; phenazine, 63–83 °C; dibenzo[a,c]anthracene, 141–152 °C; dibenzo[a,c]phenazine, 156–172 °C; dipyrido[3,2-a;2'3'-c]phenazine, 183–201 °C.

Computational Details

Electronic structure calculations were carried out using Jaguar 4.1[9] and GAUSSIAN 98[10] programs. The geometries of all the molecules were optimized using the Becke three-

Table 2.1. Ionization Energies of Organic Molecules (eV)

bands	IE (obsd)[a]	IE (calcd, raw)[b]	IE (calcd, compressed)[c]	IE (obsd) (ref. 17)
1				
B_1 (π_1)	7.888	7.751	7.888	7.87
A_2 (π_2)	8.289	8.059	8.123	(8.30)[d]
A_2 (π_3)	9.277	9.556	9.276	9.28
B_1 (π_4)	9.872	10.429	9.940	9.90
2				
B_2 (π_1)	8.342	8.227	8.342	8.35
A_2 (π_2)	8.523	8.643	8.662	(8.82)[d]
σ_N	(9.433)[d]	-		9.39
3				
B_{1g} (π_1)	8.314	8.150	8.314	8.33
B_{2g} (π_2)	8.928	8.703	8.739	(9.06)[d]
A_u (π_3)	9.519	9.765	9.556	9.56
σ_N	(9.158)[d]	-		9.2
4				
A_2 (π_1)	7.376	7.250	7.376	-
B_1 (π_2)	7.880	7.808	7.805	-
A_2 (π_3)	8.254	8.325	8.203	-
A_2 (π_4)	9.114	9.539	9.137	-
B_1 (π_5)	9.367	9.862	9.385	-
B_1 (π_6)	9.899	10.502	9.877	-

Table 2.1 is continued on the next page.

parameter Lee-Yang-Parr functional (B3LYP) and 6-31G(d,p) basis sets. B3LYP consists of the hybrid exchange functional proposed by Becke[11] and the Lee-Yang-Parr correlation functional.[12] Reorganization energies were calculated using B3LYP/6-311G++(2d,2p) level of theory. Ionization energies were estimated from restricted Hartree-Fock (RHF)

Table 2.1. (*continued*)

bands	IE (obsd)[a]	IE (calcd, raw)[b]	IE (calcd, compressed)[c]	IE (obsd) (ref. 17)
5				
A_2 (π_1)	7.983	8.007	7.983	-
B_1 (π_2)	-	8.052	8.018	-
A_2 (π_3)	8.589	8.651	8.478	-
A_2 (π_4)	9.318	9.719	9.300	-
B_1 (π_5)	9.676	10.143	9.626	-
B_1 (π_6)	10.016	10.691	10.048	-
6				
A_2 (π_1)	8.289	8.332	8.289	-
B_1 (π_2)	-	8.335	8.291	-
A_2 (π_3)	9.106	9.289	9.025	-
A_2 (π_4)	9.997	10.567	10.008	-
B_1 (π_5)	10.265	10.888	10.255	-

[a] Vertical ionizations; this work. The error in the ionization energy measurements was determined by fitting 12 individual scans of the photoelectron spectra of **1** with a series of Gaussian functions. Since all the measurements were carried out under similar conditions and the instrument resolution was nearly the same in all cases, the same error, ±0.002, was applied to the rest of the ionization energy values.

[b] Calculated using RHF/6-311G++(2d,2p).

[c] Calculated values are shifted to match the first ionization energy and compressed by factor of 1.3 (ref. 16).

[d] Tentative experimental assignment.

calculations with a 6-311G++(2d,2p) basis set (Table 2.1). Vibrational frequencies were calculated using B3LYP/6-31G(d,p) (Table 2.2) and scaled by 0.987 (for low-frequency modes) and 0.973 (for high-frequency modes).[13]

Results

Photoelectron Spectra

He I photoelectron spectra of **1**–**6** are shown in Figures 2.1-2.2. The data were fit with a series of Gaussian functions (Eq. 2.1, in which A is the peak height, p is the peak position,

$$T = A\, e^{-\alpha\left[\frac{(h\nu - p)}{H}\right]^2} \qquad \text{Eq. 2.1}$$

H is the average full-width at half-maximum, and α is 4ln(2)).[14] Sums of the Gaussian functions gave fits to the experimental data. Ionization energies of **1**–**6** are set out in Table 2.1. The bands were assigned to the ionization of π or σ_N electrons, where σ_N is the nitrogen lone pair state. Koopmans' theorem[15] aided the assignment of π states. To compensate for the relaxation and electronic correlation effects that are neglected by Koopmans' theorem, the calculated energies were shifted to match the first experimental ionization energies and then compressed by the factor of 1.3.[16] σ_N states were assigned on the basis of comparisons between diazo-molecules and their carbon analogs. The σ_N state in the phenazine spectrum was identified by comparison to the previously reported anthracene photoelectron spectrum.[17] Since σ_N bands are broad, featureless, and low-intensity, their assignment is tentative. The σ_N states in **5** and **6** were not assigned due to spectral congestion. The first two ionizations of **5** are nearly degenerate; the bands are poorly resolved (the first band is at 7.983±0.002 eV). Calculations suggest that the first and second ionizations of **6** are separated by 3 meV. These two bands, which were not experimentally resolved, are assigned an average value of 8.238±0.002 eV.

Figure 2.1. He I photoelectron spectra: (a) phenanthrene (**1**), (b) 1,10-phenanthroline (**2**), (c) phenazine (**3**). Experimental data (•••) are fit with Gaussian functions (–) on a baseline (‴), giving total fit (—).

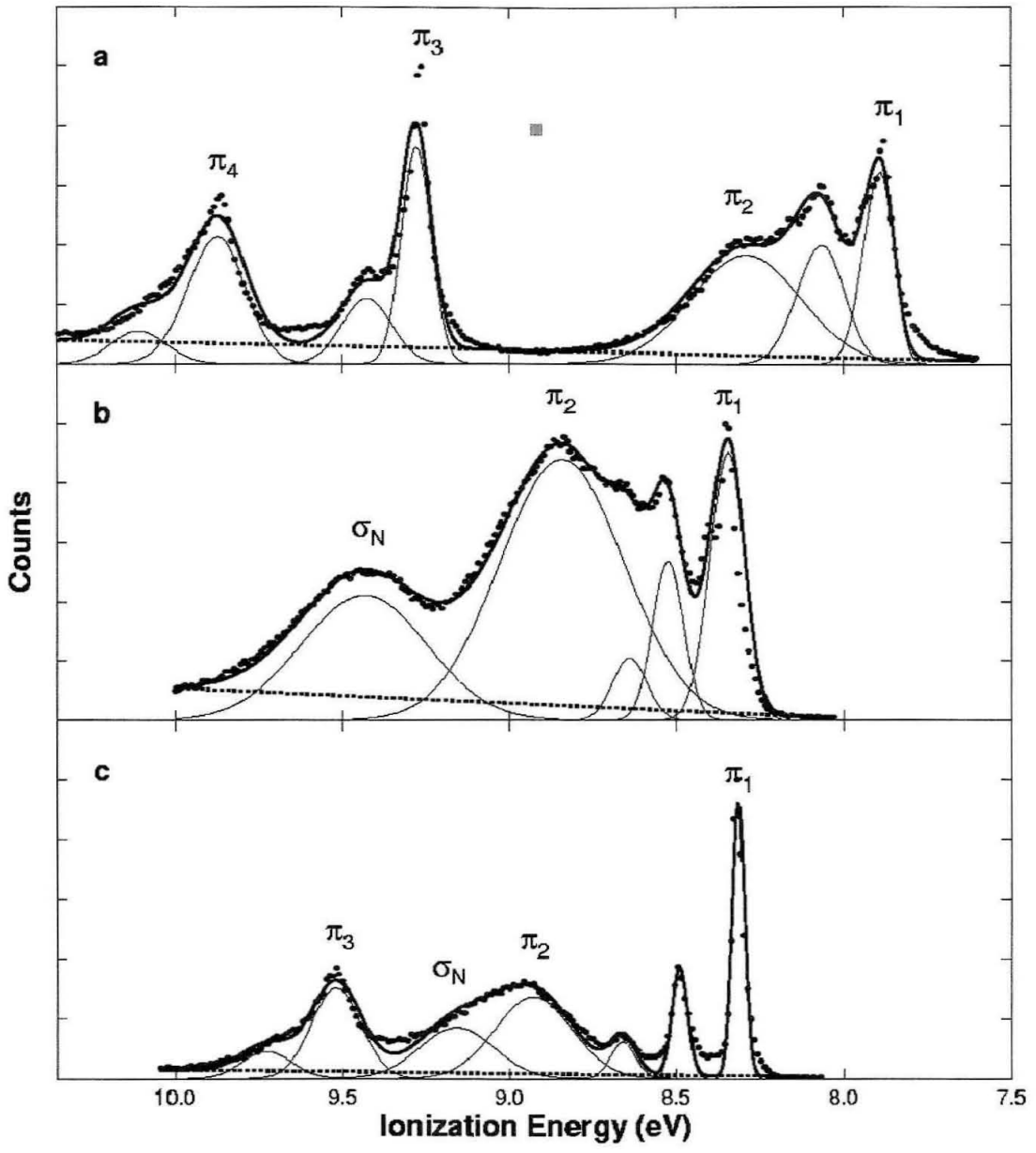
a
b
c
π_1
π_2
π_3
π_4
σ_N
Counts
10.0
9.5
9.0
8.5
8.0
7.5
Ionization Energy (eV)

Figure 2.2. He I photoelectron spectra: (a) dibenzo[a,c]anthracene (**4**), (b) dibenzo[a,c]phenazine (**5**), (c) dipyrido[3,2-a; 2'3'-c]phenazine (**6**). Experimental data (•••) are fit with Gaussian functions (–) on a baseline (‴), giving total fit (—).

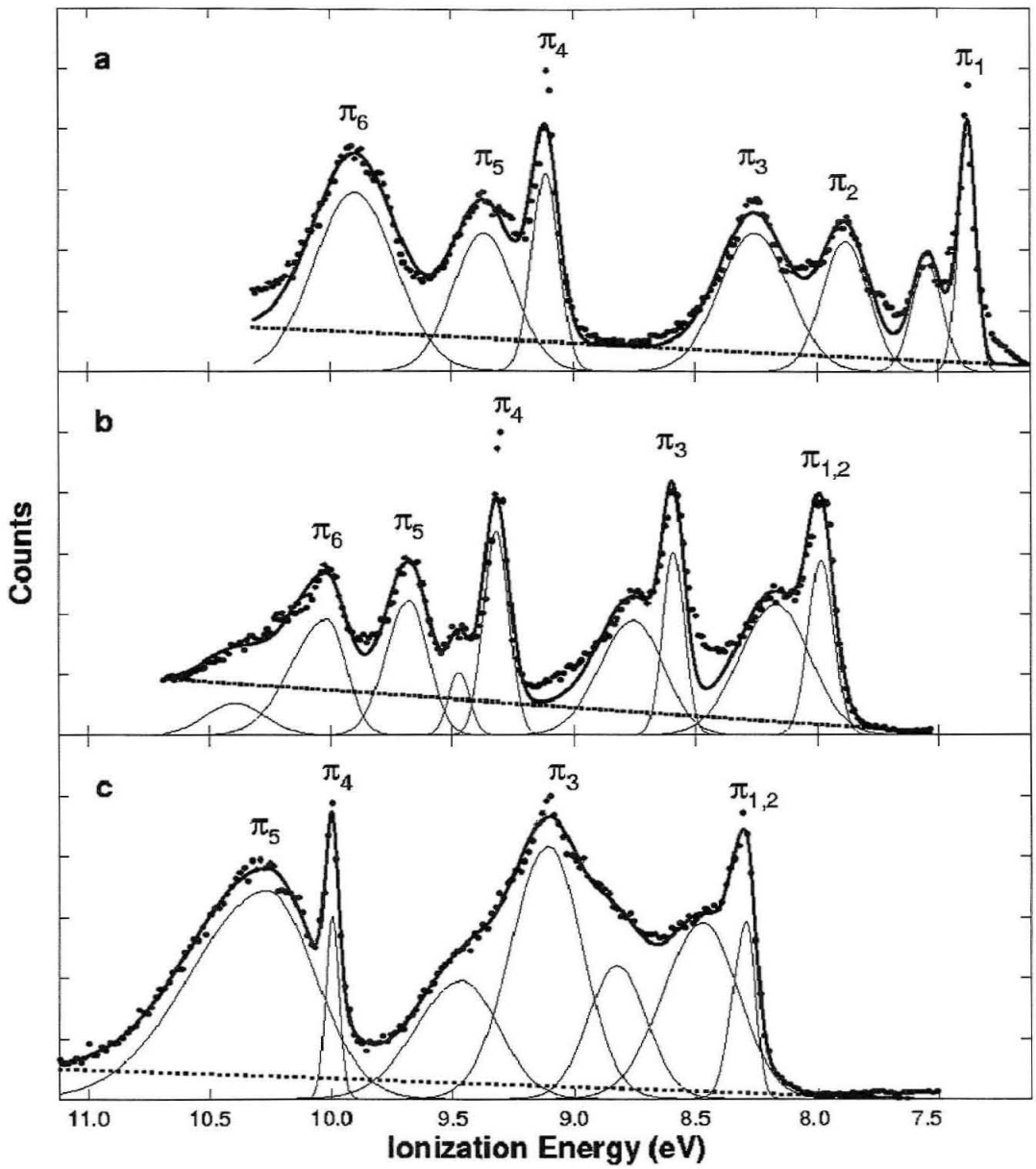
a
b
c
π_1
π_2
π_3
π_4
π_5
π_6
$\pi_{1,2}$
Counts
11.0
10.5
10.0
9.5
9.0
8.5
8.0
7.5
Ionization Energy (eV)

Table 2.2. Selected Vibrational Frequencies (cm^{-1})

molecule	mode	ν (calcd) neutral	ν (calcd) cation	ν (obsd) neutral
1	$23a_1$	242	244	247[a]
	$22a_1$	405	401	408[a]/398[b]
	$21a_1$	549	547	548[a]
	$11a_1$	1356	1365	1352[a]/ 1340[b]
	$10a_1$	1426	1417	1431[a,b]
	$9a_1$	1441	1430	1443[a]/ 1446[b]
2	$21a_1$	237	233	249[c]
	$20a_1$	408	399	408[c]
	$19a_1$	554	547	550[c]
	$10a_1$	1349	1328	1343[c]
	$9a_1$	1387	1389	1404[c]
	$8a_1$	1450	1416	1444[c]

Table 2.2 is continued on the next page.

Quantum-Mechanical Analysis (λ^{QM})

Quantum-mechanical analysis of fine structure in the spectra yielded distortion parameters (S), which are related to λ^{QM} according to Eq. 2.2 (h is Planck's constant and ν_k is the vibrational frequency of mode k).[18] The first ionization bands in the spectra of **1**–**6** exhibit vibrational progressions (Figures 2.3-2.8). The bands in each spectrum were fit with a series of Gaussian functions; widths (H) of the vibrational components in each progression

$$\lambda^{QM} = \sum_k S_k h\nu_k \qquad \text{Eq. 2.2}$$

Table 2.2. (*continued*)

molecule	mode	ν (calcd) neutral	ν (calcd) cation	ν (obsd) neutral
3	$6a_g$	1282	1268	1280[d]
	$5a_g$	1406	1395	1403[d]
	$4a_g$	1481	1486	1479[d]
4	$32a_1$	579	573	-
	$31a_1$	632	624	-
	$30a_1$	701	704	-
	$17a_1$	1337	1356	-
	$16a_1$	1372	1384	1360[e]
	$15a_1$	1405	1404	-

[a] Polarized IR/Raman spectra of single-crystal phenanthrene (ref. 19).

[b] Gas-phase IR spectra of phenanthrene (ref. 20).

[c] Polarized IR/Raman spectra of single-crystal 1,10-phenanthroline (ref. 21).

[d] Polarized Raman spectra of single-crystal phenazine (ref. 22).

[e] IR spectra of thin solid films of dibenzo[a,c]anthracene (ref. 23).

were kept fixed for molecules **1**–**4**. In all cases, hot bands were included as part of the fitting procedure. The first ionization band of **1** exhibits a high-frequency progression (1455±34 cm^{-1}) corresponding to the $10a_1$ mode, and a low-frequency progression (379±34 cm^{-1}) arising from the $22a_1$ mode (Table 2.3). The first ionization band of **2** exhibits two vibrational progressions similar to those observed for **1**: a high-frequency progression with a spacing of 1461±34 cm^{-1}; and a low-frequency progression spaced by 420±34 cm^{-1}. The first ionization band of **3** exhibits a well resolved vibrational progression spaced by 1415±34 cm^{-1} corresponding to the $5a_g$ mode (Table 2.3). The first ionization band of **4** is similar to

Table 2.3. Vibrational Frequencies (cm^{-1}) and Quantum-Mechanical Reorganization Energies (meV)

	mode	ν (obsd)[a]	ν (calcd)[b]	ν (obsd)[c]	S[d]	λ^{QM}
1	$22a_1$	379±34	405	408/ 398	0.692±0.020	33±3
	$10a_1$	1455±34	1426	1431	0.636±0.020	115±4
2	$20a_1$	420±34	408	408	0.753±0.016	39±3
	$8a_1$	1461±34	1450	1444	0.706±0.015	128±4
3	$5a_g$	1415±34	1406	1403	0.387±0.008	68±2
4	$31a_1$	632±34	632	-	0.334±0.014	26±2
	$16a_1$	1357±34	1372	1360	0.393±0.015	66±3

[a] This work.

[b] Calculated using B3LYP/6-31G(d,p).

[c] See Table 2.2.

[d] The values of S were obtained according to the expression: $S=(I_1\pm\Delta I_1)/(I_0\pm\Delta I_0)$, where ΔI_n is the square root of I_n.

those observed in the **1** and **2** spectra: a high-frequency progression (1357±34 cm^{-1}) corresponding to the $16a_1$ mode and a low-frequency progression (632±34 cm^{-1}) attributable to the $31a_1$ mode (Table 2.3).

The intensities of the individual Gaussian bands in each vibrational progression (Figures 2.3-2.6) are assumed to follow a Poisson distribution (Eq. 2.3, where I_n is the

$$I_n = \frac{S^n}{n!} e^{-S} \qquad \text{Eq. 2.3}$$

intensity of the n^{th} vibrational band).[24] Since only the first two vibrational bands are well resolved, the values of S were extracted from the ratio of I_1 to I_0. The results are summarized

Figure 2.3. Low binding energy region in He I photoelectron spectrum of **1**. Experimental data (•••) are fit with Gaussian functions corresponding to vibrational progressions (—) used in λ calculations, and π_2 ionization (- - -) on a baseline(···). Other Gaussian functions (—) describe spectral features of π_1.

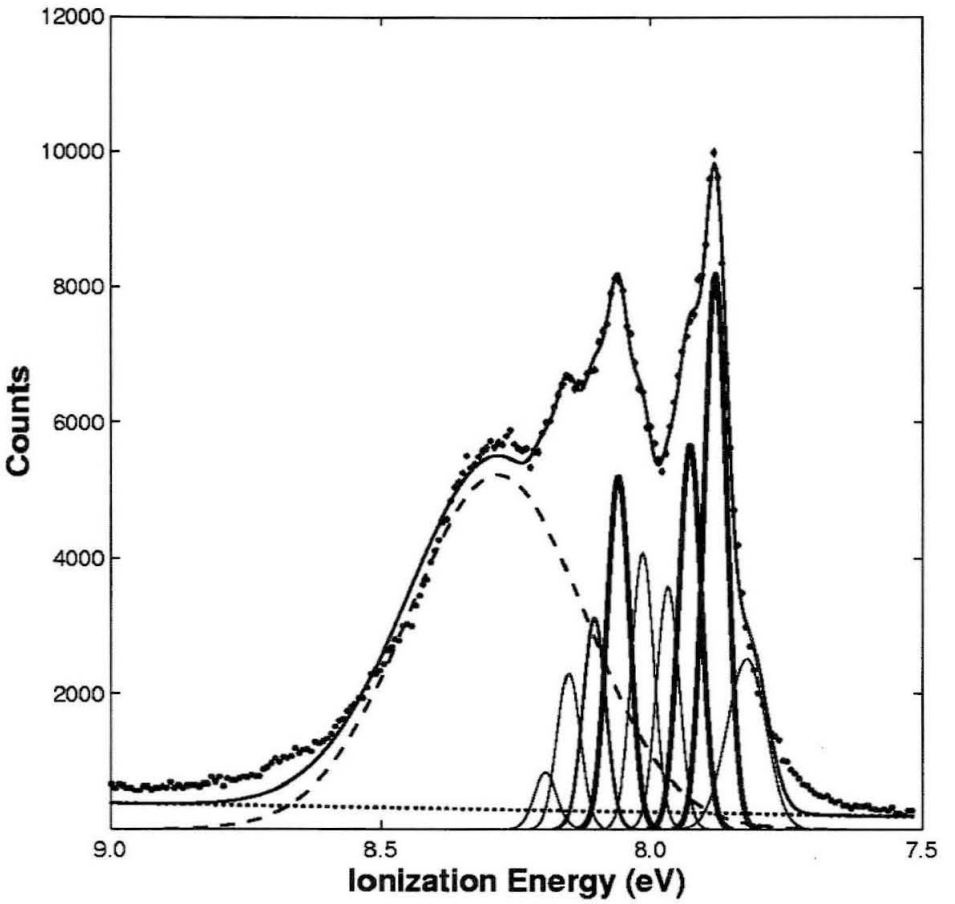
12000
10000
8000
6000
4000
2000
Counts
9.0
8.5
8.0
7.5
Ionization Energy (eV)

Figure 2.4. Low binding energy region in He I photoelectron spectrum of **2**. Experimental data (•••) are fit with Gaussian functions corresponding to vibrational progressions (—) used in λ calculations, and π_2 and σ ionization (- - -) on a baseline(···). Other Gaussian functions (—) describe spectral features of π_1.

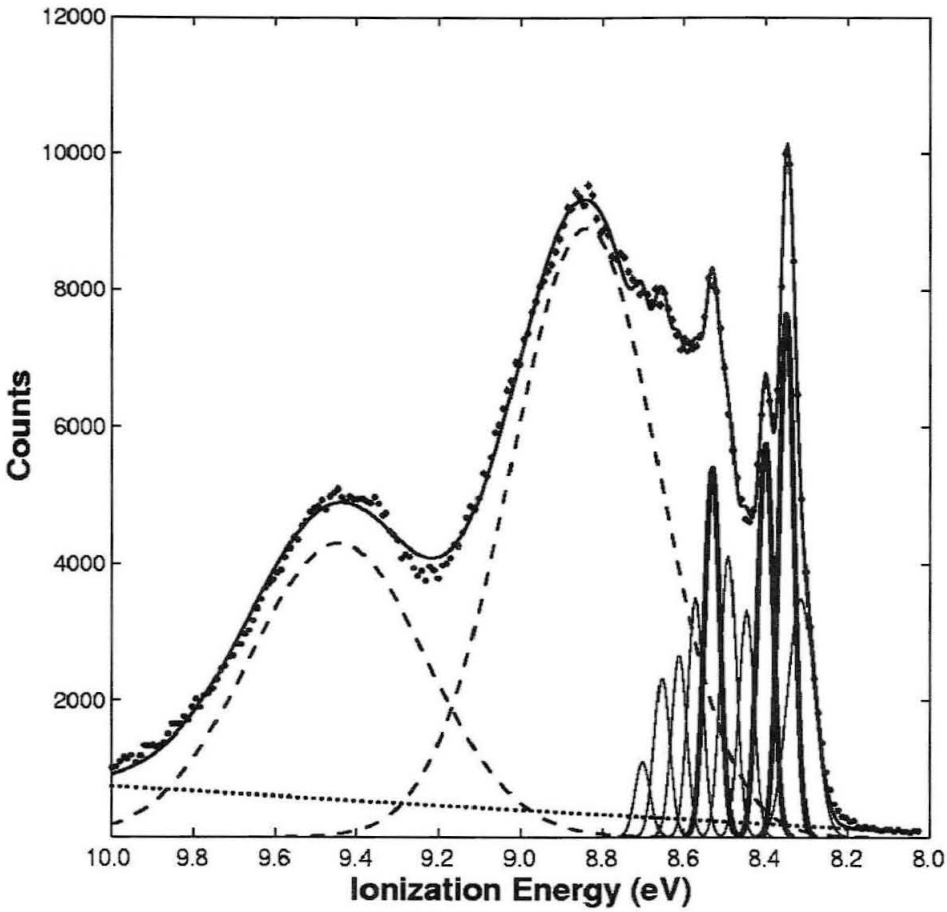
12000
10000
8000
6000
4000
2000
Counts
10.0
9.8
9.6
9.4
9.2
9.0
8.8
8.6
8.4
8.2
8.0
Ionization Energy (eV)

Figure 2.5. Low binding energy region in He I photoelectron spectrum of **3**. Experimental data (•••) are fit with Gaussian functions corresponding to vibrational progressions (—) used in λ calculations on a baseline(···). Other Gaussian functions (—) describe spectral features of π_1.

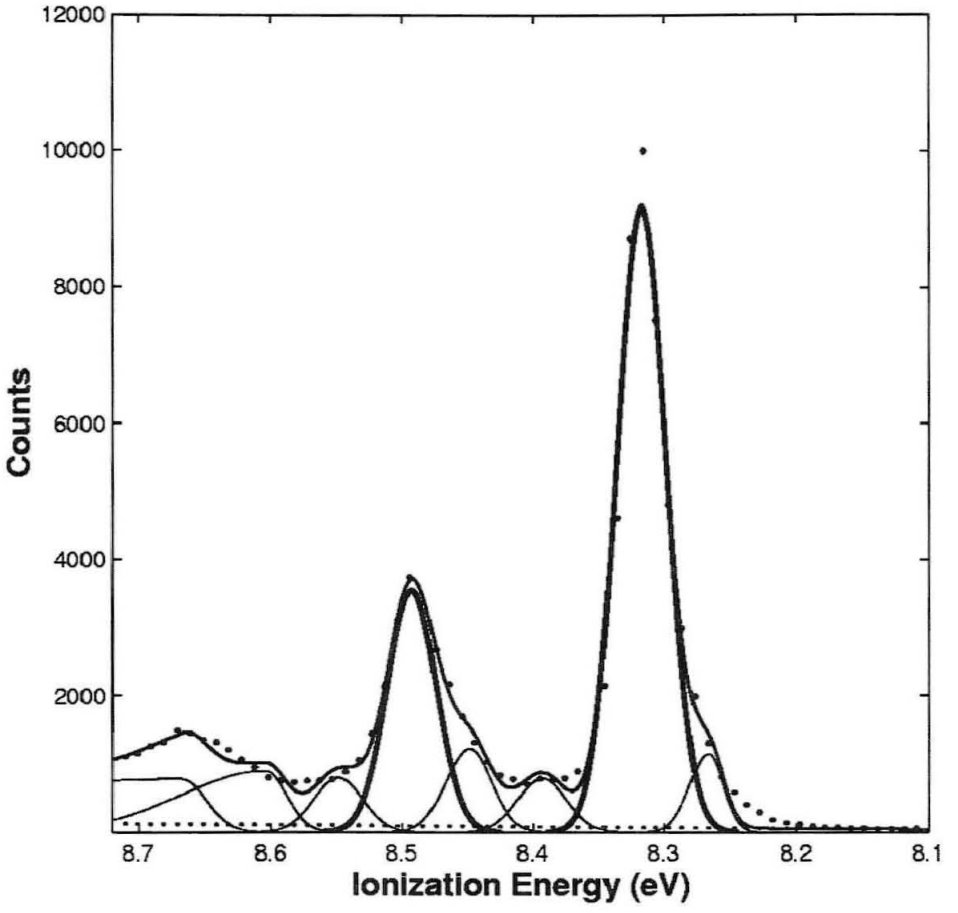
12000
10000
8000
6000
4000
2000
Counts
8.7
8.6
8.5
8.4
8.3
8.2
8.1
Ionization Energy (eV)

Figure 2.6. Low binding energy region in He I photoelectron spectrum of **4**. Experimental data (•••) are fit with Gaussian functions corresponding to vibrational progressions (—) used in λ calculations, and π_2 and π_3 ionization (- - -) on a baseline(···). Other Gaussian functions (—) describe spectral features of π_1.

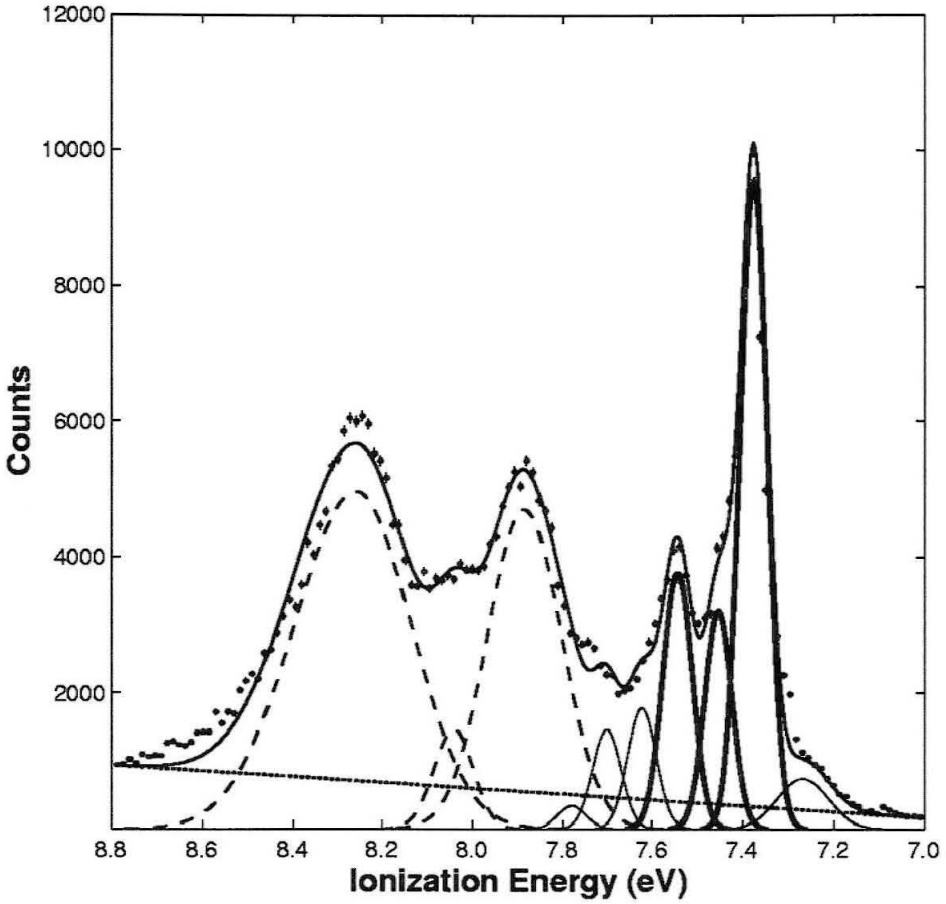
12000
10000
8000
6000
4000
2000
Counts
8.8
8.6
8.4
8.2
8.0
7.8
7.6
7.4
7.2
7.0
Ionization Energy (eV)

Figure 2.7. Low binding energy region in He I photoelectron spectrum of **5**. Experimental data (•••) are fit with Gaussian functions corresponding to π_3 ionization (- - -) on a baseline(···). Only one Gaussian function (—) is used in λ calculations. Other Gaussian functions (—) describe spectral features of π_1 and π_2.

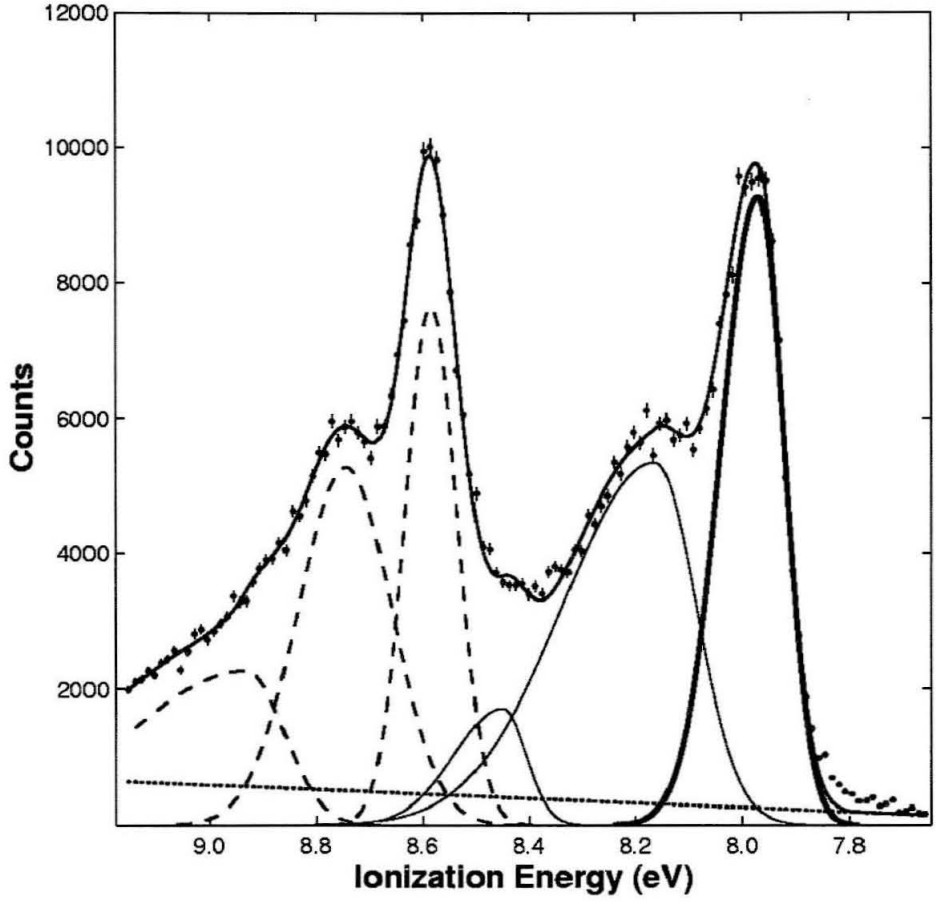
12000
10000
8000
6000
4000
2000
Counts
9.0
8.8
8.6
8.4
8.2
8.0
7.8
Ionization Energy (eV)

Figure 2.8. Low binding energy region in He I photoelectron spectrum of **6**. Experimental data (•••) are fit with Gaussian functions corresponding to π_3 ionization (- - -) on a baseline(···). Only one Gaussian function (—) is used in λ calculations. Other Gaussian functions (—) describe spectral features of π_1 and π_2.

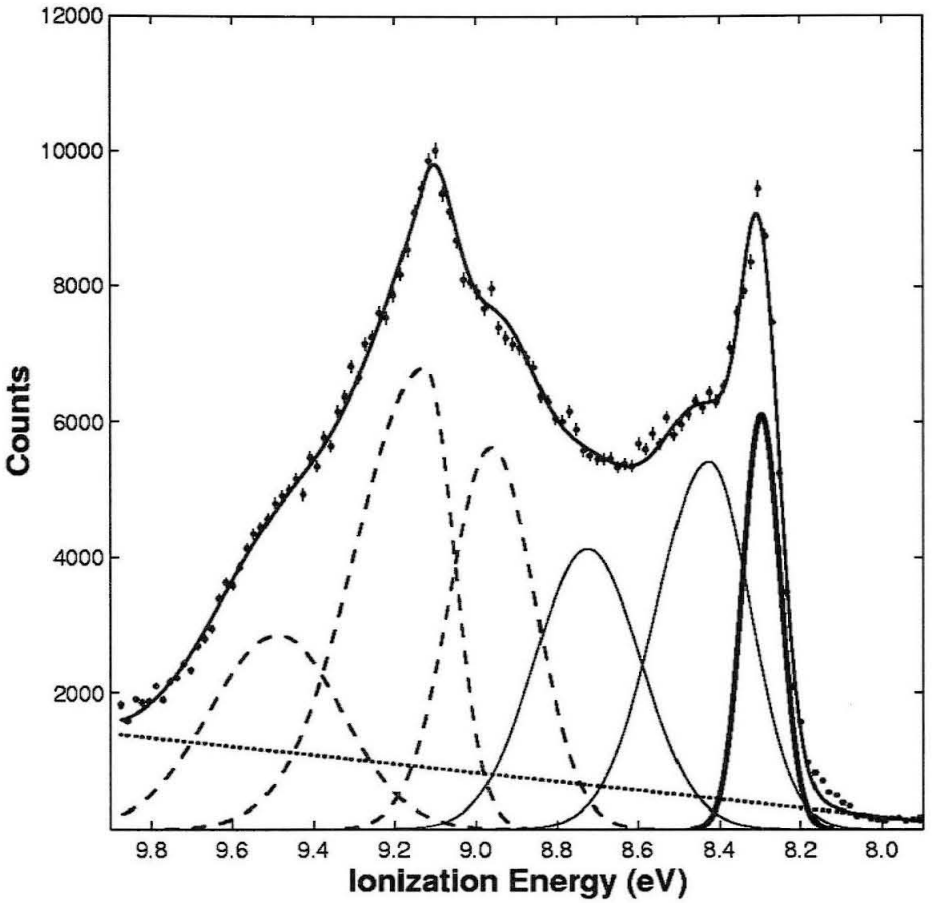
12000
10000
8000
6000
4000
2000
Counts
9.8
9.6
9.4
9.2
9.0
8.8
8.6
8.4
8.2
8.0
Ionization Energy (eV)

in Table 2.3. According to the RHF/6-311G++(2d,2p) calculation (Table 2.1), the first and second ionization energies of **5** are nearly the same; although vibrational structure is present in the spectrum, it is difficult to determine the mode to which it corresponds. Thus, values of *S* were not obtained for this molecule. Similar problems complicated the analysis of the photoelectron spectrum of **6**.

Semiclassical Analysis (λ^{SC})

Distortions along low-frequency modes and small frequency changes between the

$$G = |D|^2 \, e^{-\frac{(h\nu - IE)^2}{4 k_B T \lambda_{SC}}} \qquad \text{Eq. 2.4}$$

neutral and cation states (Table 2.2) can contribute to the breadth of individual vibronic lines in photoelectron spectra. Such band profiles are treated semiclassically (Eq. 2.4, *IE* is the

$$T(\nu) = \int_{\nu}^{\nu} G(x) \, R(x-\nu) \, dx \qquad \text{Eq. 2.5}$$

ionization energy and *D* is related to the transition moment).[24] The Gaussian functions, *T*(ν) (described in Eq. 2.1), that were used to fit the experimental spectra are convolutions of *G* (defined in Eq. 2.4) and another Gaussian function, *R*, defined by the resolution of the instrument Eq. 2.5.[25]

The value of *H*, the average full-width at half-maximum, for function *G* was obtained

$$\lambda^{SC} = \frac{H^2}{16 \ln(2) \, k_B \, T} \qquad \text{Eq. 2.6}$$

by iterative reconvolution of the observed line-shape function and is related to λ^{SC}, according

to Eq. 2.6. The results are summarized in Table 2.4.

Reorganization Energies

Table 2.4. Experimental and Calculated Reorganization Energies (meV)

	λ^{QM}	λ^{SC}	λ	$\lambda^{+\bullet}$	λ^{0}	λ^{total}	$2\lambda^{a}$
1	149±5	21±1	170±5	107	105	212	340±5
2	167±5	13±1	180±5	129	143	272	360±5
3	68±2	22±1	90±2	54	77	131	180±2
4	92±4	66±1	154±4	57	65	122	316±4
5	(≤100)[b]	27±9	(≤127±9)[b]	71	76	147	(≤254±9)[b]
6	(≤100)[b]	16±1	(≤116±1)[b]	61	60	121	(≤232±1)[b]

[a] Twice the observed reorganization energy for the self-exchange reaction.

[b] Tentative assignment.

Calculations employed B3LYP/6-31G(d,p) optimized geometries. B3LYP/6-311G++(2d,2p) single-point energies were calculated for four cases: (1) neutral optimized geometry, charge zero, and singlet multiplicity; (2) neutral geometry, charge plus one, and doublet multiplicity; (3) radical cation geometry, charge zero, and singlet multiplicity; and (4) radical cation geometry, charge plus one, and doublet multiplicity (Figure 2.9). The energy difference between (1) and (3) is λ^{0}, and the energy difference between (4) and (2) is $\lambda^{+\bullet}$. The latter parameter is compared to experimentally derived values of λ in Table 2.4. The total reorganization energy for the $A + A^{\bullet+} \rightleftharpoons A^{\bullet+} + A$ process is the sum of $\lambda^{+\bullet}$ and λ^{0} (Table 2.4).

Figure 2.9. Potential energy surfaces of neutral and cation states that define $\lambda^{+\bullet}$ and λ^{0}.

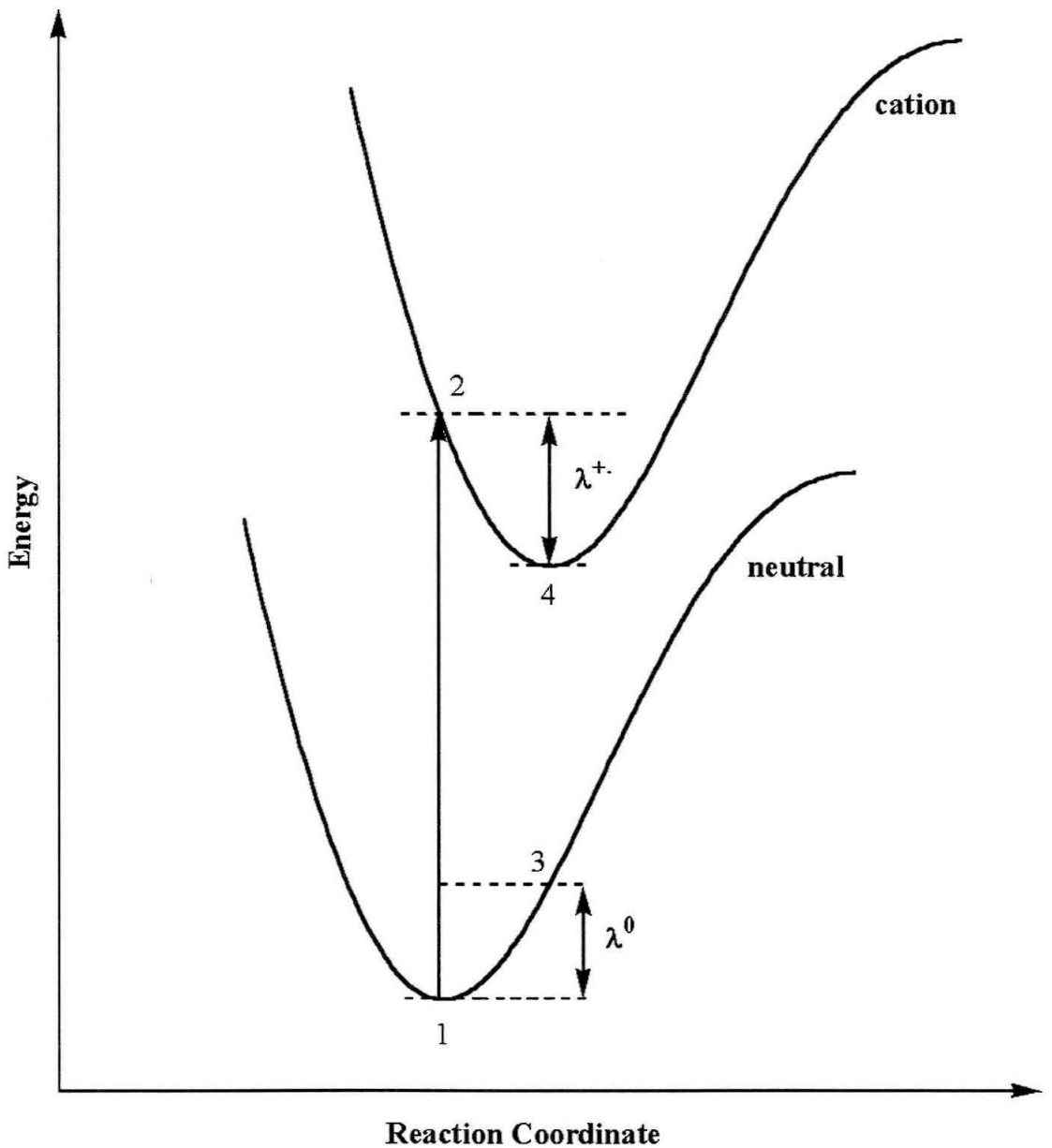
cation
neutral
2
4
3
1
$\lambda^{+\cdot}$
λ^{0}
Energy
Reaction Coordinate

Discussion

Excellent agreement was obtained between experimental and calculated ionization energies for molecules **1** through **6** (Table 2.1). Koopmans' theorem gives raw calculated values for the first ionization energies that are roughly 0.1 eV lower than the experimental results. Shifting ionization energies such that the first experimental and calculated ionization energies are the same and then compressing the results by the factor of 1.3 produces excellent agreement (within 0.068-0.010 eV) with the experimental values.

Quantum-mechanical analyses of the first ionization bands of compounds **1**–**4** gave λ^{QM} values (Tables 2.3-2.4). The values for the vibrational spacings in the photoelectron spectra accord with calculated and experimental frequencies for the neutral molecules (Table 2.2). The frequency of the $22a_1$ mode in the spectrum of **1** is in excellent agreement with gas-phase IR data[20] and B3LYP calculations. The high-frequency vibrational spacing corresponding to the $10a_1$ mode also accords with experimental results and calculations.

Since the only difference between **1** and **2** is the presence of nitrogen atoms in ring positions 1 and 10, it is reasonable to expect that similar vibrational modes will be observed in the spectra of these molecules. Indeed, the $20a_1$ mode in the spectrum of **2** corresponds to the $22a_1$ mode of **1**. Moreover, the observed frequency is in good agreement with experimental and computational results. The high-frequency progression in **2** is spaced by 1461 ± 34 cm^{-1}, which is in excellent agreement with the $8a_1$ experimental and calculated vibrational frequencies (Table 2.2). The vibrational frequency of the $9a_1$ mode of **2**, however, corresponds to the observed $10a_1$ mode in the spectrum of **1**. The experimental

frequency[21] of $9a_1$ in **2** is 1404 cm^{-1} (the calculated value is 1387 cm^{-1}). Given the relative error in the spacing of the high-frequency progression in the spectrum of **2**, the assignment to $9a_1$ is tentative. Unlike the $10a_1$ mode of **1**, however, there is only a 2 cm^{-1} difference between calculated $9a_1$ vibrational frequencies for the neutral and cation states of **2** (Table 2.2). For the $8a_1$ mode of **2**, the difference between neutral and cation states is 34 cm^{-1}. Based on these observations, the observed high-frequency progression was assigned in the spectrum of **2** to $8a_1$, even though it does not correspond to the $10a_1$ mode of **1**.

A well-resolved vibrational progression in the spectrum of **3** corresponds to the $5a_g$ mode. Low-frequency progressions are also observed (Figure 2.5) and are used to fit the experimental data. These vibrational lines, however, are poorly resolved and were not used to estimate the reorganization energy.

The only five-ring molecule in the series that has a well-resolved high-frequency progression is **4**. This progression (spaced by 1357±34 cm^{-1}) is assigned to the $16a_1$ mode, and the low-frequency progression to $31a_1$. λ^{QM} is estimate to be 92±4 meV, which is lower than λ^{QM} for **1** or **2**. λ^{SC} is estimated to be 66±1 meV, which is larger than λ^{SC} for **1**, **2**, or **3**. If λ^{SC} is overestimated, it would explain the significant difference, 101 meV, between experimental and calculated reorganization energies.

Since the first and second ionization bands overlap in the photoelectron spectra of **5** and **6**, values of λ^{QM} were not obtained. Semiclassical bandshape analyses give 27 ±9 meV for **5** and 16 ±1 meV for **6**. λ^{QM} is assumed to be not greater than 100 meV. Therefore, the total reorganization energy is expected for **5** or **6** not to exceed 120–130 meV.

Calculated $\lambda^{+\bullet}$ values are lower than their experimental counterparts (Table 2.4). The

best agreement is for **3**, where the difference between experimental and calculated parameters is only 36 meV. Computational results reproduce experimental trends in λ values (Table 2.4): λ and $\lambda^{+\bullet}$ for the three-ring molecules are larger than those for the five-ring systems, with the exception of **3**. Ring systems containing heteroatoms exhibit larger λ and $\lambda^{+\bullet}$ values than their carbon analogs.

Calculated values of $\lambda^{+\bullet}$ and λ^{0} are similar for **1**–**6** (Table 2.4), indicating that curvatures of the energy surfaces are equivalent for equilibrium geometries of neutral molecules and cations. The curvatures of experimental parabolic surfaces for the neutral and cation species are also assumed to be the same; therefore, total reorganization energies for the self-exchange electron-transfer reaction, $A + A^{\bullet+} \rightleftharpoons A^{\bullet+} + A$, are 2λ (Table 2.4). With the assumption that solvent molecules do not perturb any of the internal modes involved in the self-exchange reaction, 2λ is the same as λ_i. The value of 2λ for **1** is 340 meV, and λ_i for intramolecular electron transfer between phenanthrene and the biphenyl anion radical is 450 meV.[3] Assuming that the reorganization energy of biphenyl is not greater than that of phenanthrene, λ_i for this reaction is only slightly higher than predicted from our results.

To extend the analysis to a single-ring system, the reported He I photoelectron spectrum of benzene is examined.[26] Unlike **1**–**6**, benzene has degenerate HOMOs and the first ionization energy is due to the removal of an electron from the $1e_{1g}$ π orbital.[27] Owing to the Jahn-Teller effect,[28] vibrational structure in the benzene spectrum is complex: the first band exhibits a strong adiabatic transition followed by short and weak progressions,[26] indicative of a small geometry change upon ionization. Treating the spectrum as for **1**–**6**, estimated λ does not exceed 100 meV. Calculations of the reorganization energy of benzene

anion formation indicate that $\lambda^{-\bullet}$ is in the range 289–158 meV;[29] and reported changes in the bond lengths for the negative ion are almost the same as for the positive ion,[29] a finding supporting the assumption that $\lambda^{+\bullet} \approx \lambda^{-\bullet}$. The value of $\lambda^{-\bullet}$ for anthracene is in the range 67–86 meV,[29] which agrees well with our B3LYP calculation of $\lambda^{+\bullet}$, 57 meV, and experimental λ, 90 meV, of **3**. Since $\lambda^{-\bullet}$ for anthracene is nearly the same as $\lambda^{+\bullet}$ and λ of **3**, and $\lambda^{-\bullet}$ for benzene is slightly larger than 100 meV, our estimate of λ for benzene is reasonable. What is more, it is consistent with resonance Raman experiments of Myers and coworkers on the hexamethylbenzene/tetracyanoethylene complex, where the reorganization energy of specific modes localized on hexamethylbenzene is estimated to be 129 meV.[30]

Conclusion

It has been shown that mode-specific quantum-mechanical and semiclassical analyses of ionization band profiles can be used to determine electron-transfer reorganization energies for isolated molecules. Experimentally derived λ values for **1-6** are in the range 90 to 180 meV, and are on average 63 meV higher than the B3LYP results. Reorganization energies of five-ring systems are slightly lower that those for three-ring systems. Analysis of the photoelectron spectrum of benzene yields $\lambda \leq 100$ meV.

References and Notes

(1) Balzani, V., Ed. *Electron Transfer in Chemistry*; Wiley-VCH Verlang GmbH: D-69469 Weinheim, Germany, **2001**; Vols. 1-5.

(2) Marcus, R. A.; Sutin, N. *Biochim. Biophys. Acta* **1985**, *811*, 265-322.

(3) Miller, J. R.; Closs, G. L. *Science* **1988**, *240*, 440-447.

(4) (a) Chattoraj, M.; Laursen, S. L.; Paulson, B.; Chung, D. D.; Closs, G. L.; Levy, D.H. *J. Phys. Chem.* **1992**, *96*, 8778-8784. (b) Jortner, J.; Bixon, M.; Wegewijs, B.; Verhoeven, J. W.; Rettschnick, R. P. H. *Chem. Phys. Lett.* **1993**, *205*, 451-455. (c) Shou, H.; Alfano, J. C.; van Dantzig, N. A.; Levy, D. H.; Yang, N. C. *J. Chem. Phys.* **1991**, *95*, 711-713. (d) Brenner, V.; Millie, P.; Piuzzi, F.; Tramer, A. *J. Chem. Soc., Faraday Trans.* **1997**, *93*, 3277-3287. (e) Tramer, A.; Brenner, V.; Millie, P.; Piuzzi, F. *J. Phys. Chem.* **1998**, *A102*, 2798-2807. (f) Van Dantzig, N. A.; Shou, H.; Alfano, J. C.; Yang, N. C.; Levy. D. H. *J Chem. Phys.* **1994**, *100*, 7068-7078.

(5) Ref.1, Vol. 3, Part 2, p.177.

(6) Lichtenberger, D.L.; Kellogg, G. E.; Kristofzski, J. G.; Page, D.; Turner, S.; Klinger, G. Lorenzen, *J. Rev.Sci. Instrum.* **1986**, *57*, 2366.

(7) Renshaw, S. K. *Ph.D. Dissertation*; University of Arizona: Arizona, **1992**.

(8) Turner, D. W.; Baker, C.; Baker, A. D.; Brundle, C. R. *Molecular Photoelectron Spectroscopy*; Wiley-Interscience: London, **1970**.

(9) Jaguar version 4.0, Schrödinger Inc.: Portland, OR, **1999**.

(10) GAUSSIAN 98, Revision A.9, Frisch, M. J.; Trucks, G. W.; Schlegel, H. B.; Scuseria, G. E.; Robb, M. A.; Cheeseman, J. R.; Zakrzewski, V. G.; Montgomery, Jr.,J. A.;

Stratmann, R. E.; Burant, J. C.; Dapprich, S.; Millam, J. M.; Daniels, A. D.; Kudin, K. N.; Strain, M. C.; Farkas, O.; Tomasi, J.; Barone, V.; Cossi, M.; Cammi, R.; Mennucci, B.; Pomelli, C.; Adamo, C.; Clifford, S.; Ochterski, J.; Petersson, G. A.; Ayala, P. Y.; Cui, Q.; Morokuma, K.; Malick, D. K.; Rabuck, A. D.; Raghavachari, K.; Foresman, J. B.; Cioslowski, J.; Ortiz, J. V.; Baboul, A. G.; Stefanov, B. B.; Liu, G.; Liashenko, A.; Piskorz, P.; Komaromi, I.; Gomperts, R.; Martin, R. L.; Fox, D. J.; Keith, T.; Al-Laham, M. A.; Peng, C. Y.; Nanayakkara, A.; Challacombe, M.; Gill, P. M. W.; Johnson, B.; Chen, W; Wong, M. W.; Andres, J. L.; Gonzalez, C.; Head-Gordon, M.; Replogle, E. S.; and Pople, J. A. Gaussian, Inc.: Pittsburgh PA, **1998**.

(11) Becke, A.D. *J. Chem. Phys.* **1993**, *98*, 5648-5652.

(12) Lee, C.; Yang, W.; Parr, R. G. *Phys. Rev.* **1988**, *B37*, 785-789.

(13) There is a simple procedure for scaling the raw calculated values (Martin, J. M. L.; El-Yazal, J.; Francois, J.-P. *J. Phys. Chem.* **1996**, *100*, 15358-15367.) that accounts for anharmonicities provided that no strong Fermi resonances exist. See Chapter 5 for more detail.

(14) Lichtenberger, D. L.; Copenhaver, A. S. *J. Electron Spectrosc. Relat. Phenom.* **1990**, *50*, 335-352.

(15) Koopmans, T. *Physica* **1933**, *1*,104.

(16) Cornil, J.; Vanderdonckt, S.; Lazzaroni, R.; dos Santos, D. A.; Thys, G.; Geise, H. J.; Yu, L.-M.; Szablewski, M.; Bloor, D.; Lögdlund, M.; Salaneck, W. R.; Gruhn, N. E.; Lichtenberger, D. L.; Lee, P. A.; Armstrong, N. R.; and Brédas, J. L. *Chem. Mater.* **1999**, *11*, 2436-2443.

(17) Hush, N. S.; Cheung, A. S.; Hilton, P. R. *J. Electron Spectrosc. Relat Phenom.* **1975**, *7*, 385-400.

(18) Brunschwig, B. S.; Sutin, N. *Comments Inorg. Chem.* **1987**, *6*, 209-235.

(19) Bree, A.; Solven, F.G.; Vilkos, V.V.B. *J. Mol. Spectrosc.* **1972**, *44*, 298-319.

(20) Cane, E.; Miani, A.; Palmieri, P.; Tarroni, R.; Trombetti, A. *Spectrochim. Acta* **1997**, *A53*, 1839-1851.

(21) Perkampus, H.. -H.; Rother, W. *Spectrochim. Acta* **1974**, *A30*, 597-610.

(22) Durnick, T. J.; Wait, S. C. Jr. *J. Mol. Spectrosc.* **1972**, *42*, 211-226.

(23) Orr, S. F. D.; Thompson, H. W. *J. Chem. Soc.* **1950**, 218-221.

(24) Ballhausen, C. J. *Molecular Electronic Structures of Transition Metal Complexes*; McGraw-Hill, Inc.: UK, **1979**, p. 125.

(25) Press, W. H.; Flannery, B. P.; Teukolsky, S. A.; Vetterling, W. T. *Numerical Recipes, The Art of Scientific Computing, (Fortran Version)*; Cambridge University Press: New York, NY, **1989**, p.383.

(26) Karlsson, L.; Mattson, L.; Jadrny, R.; Bergmark, T.; Siegbahn, K. *Phys. Scr.* **1976**, *14*, 230-241.

(27) Hollas, J. M. *Modern Spectroscopy*; John Wiley & Sons Ltd: Chichester, UK, **1996**, p.270.

(28) Jahn, H. A.; Teller, E. *Proc. R. Soc.* **1937**, *A161*, 220-235.

(29) Klimkāns, A.; Larsson, S. *Chem. Phys.* **1994**, *189*, 25-31.

(30) Markel, F.; Ferris, N. S.; Gould, I. R.; Myers, A. B. *J. Am. Chem. Soc.* **1992**, *114*, 6208-6219.

Chapter 3

Electronic Structures and Electron-Transfer Reorganization Energies of Free Base and Zn(II) Protoporphyrin IX[†]

[†] Adapted from X. Amashukeli, H. B. Gray, N. E. Gruhn, D. L. Lichtenberger, in preparation (2002).

Acknowledgments:

This work would not have been possible without the Gas-Phase Photoelectron Spectroscopy facilities at the University of Arizona, and the Molecular Simulation Center at Caltech.

Introduction

In nature, porphyrin is a ubiquitous chromophore: hemes, the iron(II) and (III) complexes of protoporphyrin IX, are the prosthetic groups of myoglobins, hemoglobins, cytochromes, peroxidases, and catalases.[1] The reactivity of hemes greatly depends on their electronic structures, which can be studied by photoelectron spectroscopy. Heme active sites participate in a variety of biological electron-transfer reactions.[2] According to the semiclassical ET theory, the rates of these reactions depend on the standard free energy change, ΔG^0, the electronic coupling matrix element, H_{AB}, and the reorganization energy, λ (where $\lambda = \lambda_i + \lambda_o$, the inner- and outer-sphere contributions).[3] We have demonstrated that it is possible to obtain reorganization energies of isolated molecules, λ_i, from fine structure analyses of their photoelectron spectra.[4] This motivated us to acquire photoelectron spectra of protoporphyrin IX (PPIX), and Zn(II)protoporphyrin IX (ZnPPIX) (Scheme 3.1), assign their first two ionization bands, and estimate their gas-phase ET reorganization energies. To our knowledge, this is the first such study of biologically relevant porphyrins.

Materials and Methods

Molecules

PPIX and ZnPPIX were obtained from Frontier Scientific and were used without further purification.

Scheme 3.1. Molecules: **1** is PPIX and **2** is ZnPPIX.

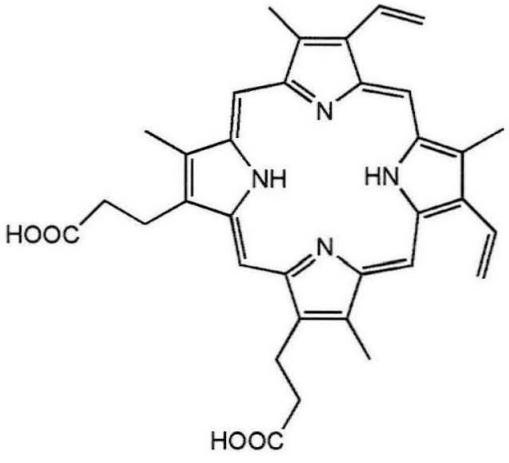

1

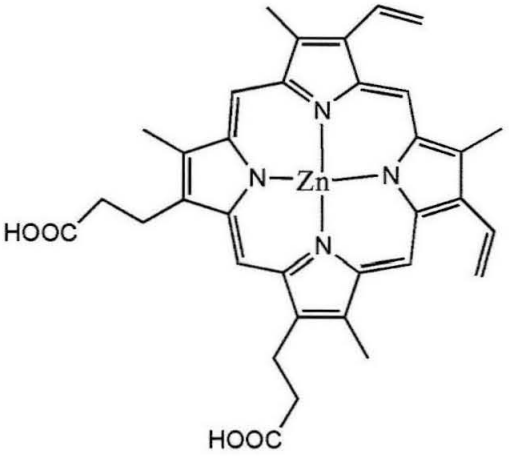

2

Figure 3.1. Full He I photoelectron spectra of (a) PPIX and (b) ZnPPIX. Maximum number of counts for each molecule is 1000.

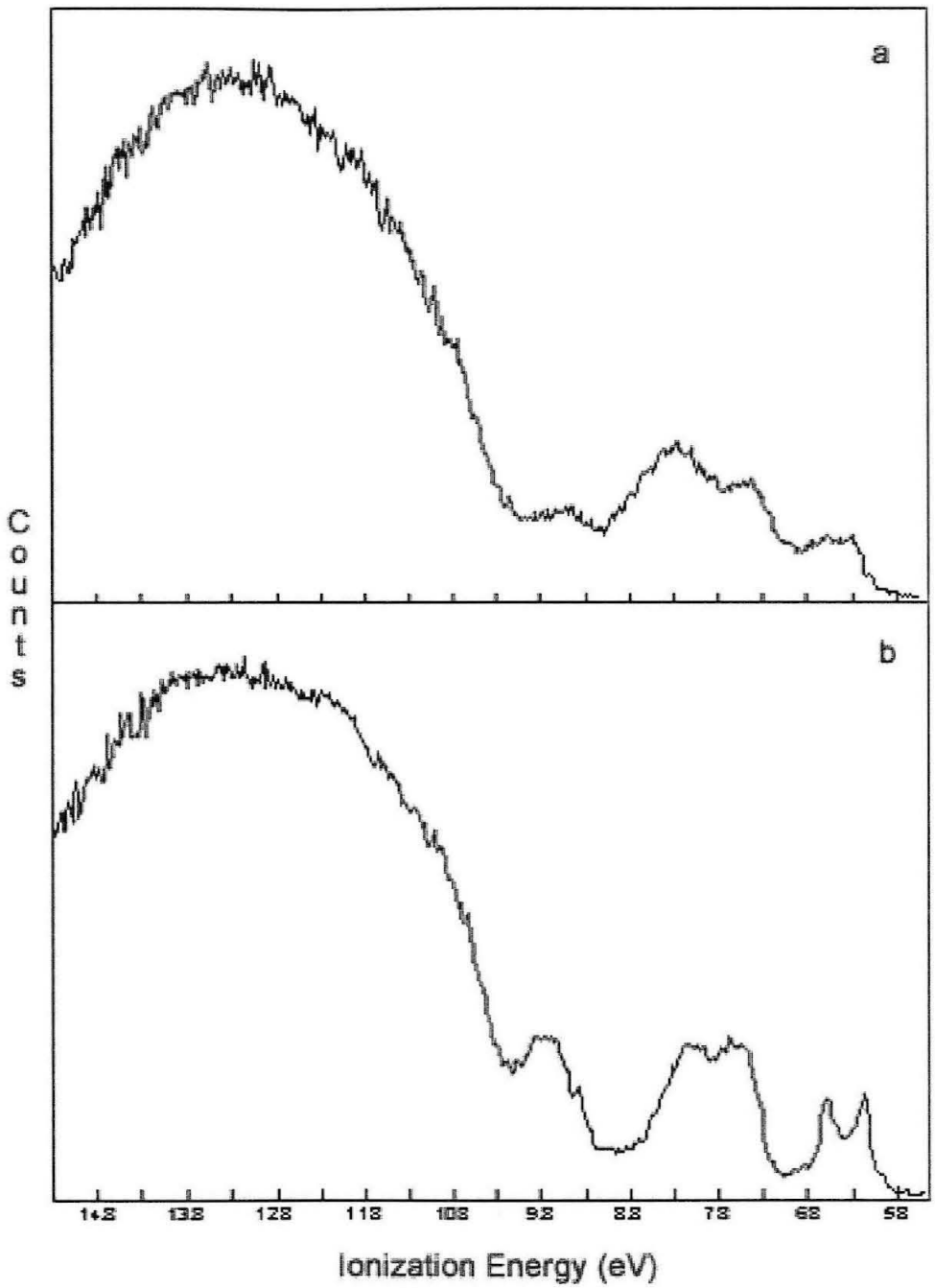
a
b
Counts
14.5
13.5
12.5
11.5
10.5
9.5
8.5
7.5
6.5
5.5
Ionization Energy (eV)

Experimental Details of Photoelectron Spectroscopy

Photoelectron spectra were recorded using an instrument equipped with 36 cm diameter, 8 cm gap hemispherical analyzer (McPherson), which is described in more detail elsewhere.[5] The ionization energy scale was calibrated using the $^2E_{½}$ ionization of methyl iodide (9.538 eV). Argon $^2P_{3/2}$ ionization (15.759 eV) was used as an internal energy scale lock during data collection. The instrument resolution, measured as full-width and half-maximum of the argon $^2P_{3/2}$ ionization, was 0.025–0.038 eV. All data were intensity corrected with an experimentally determined instrument analyzer sensitivity function, which has a linear dependence of the analyzer transmission (intensity) on the kinetic energy of the electrons within the energy range of these experiments. Since the discharge sources (He I and II) are not monochromatic,[6] the spectra collected with the He Iα ($1s^2 \leftarrow 1s2p$, 21.218 eV) source were corrected for the He Iβ line ($1s^2 \leftarrow 1s3p$, 23.085 eV, and 3% of the intensity of the He Iα line), and the He IIα ($1s \leftarrow 2p$, 40.814 eV) spectra were corrected for the He IIβ line ($1s \leftarrow 3p$, 48.372 eV, and 12% of the intensity of the He IIα line). The sublimation temperature of PPIX (at 10^{-4}-10^{-5} Torr) was 265–295 °C, and that of ZnPPIX (at 10^{-4}–10^{-5} Torr) was 245–275 °C. The temperatures were monitored by a "K" type thermocouple passed through a vacuum feedthrough and attached directly to the ionization cell.

Photoelectron Data Analyses

The vertical length of each data mark in the spectra represents the experimental variance of that point.[7] The ionization bands are represented analytically with the best fit of asymmetric Gaussian functions, which are defined by position, amplitude, and half-width for

Table 3.1. Analytical Representation of PPIX PES Data

Ionization band		Half-Width (eV)		Relative Area		
label	**energy (eV)**	**high**	**low**	**He I**	**He II**	**He II/He I**
1	5.89	0.27	0.16			
2	6.14	0.23	0.22	1	1	1
3	6.30	0.24	0.18			
4	6.58	0.42	0.41	1.78	1.92	1.08
5	6.95	0.48	0.45	1.11	0.97	0.87
6	7.45	0.53	0.52	4.20	3.78	0.90
7	7.92	0.47	0.47	3.22	3.43	1.06
8	8.23	0.54	0.44	4.37	4.99	1.14
9	8.66	0.91	0.47	4.76	5.59	1.12
10	9.54	3.37	0.53	9.11	11.50	1.26

the high and low binding energies. The He I spectrum of PPIX was fit first; the number of Gaussian functions employed was based on the features in the spectrum and the number of functions necessary for a statistically good fit. The He II spectrum of PPIX was fit next: the positions and half-widths were kept fixed to those of the He I fit and the peak amplitudes were allowed to vary to account for the changes in the ionization cross sections. The relative integrated peak areas are known within 5–10% confidence limit. Because of the electron scattering, the major source of uncertainty is in the determination of the base line, which is assumed to be nearly linear over a small energy range of these spectra. The area under the overlapping Gaussian peaks is known within the same confidence limit. The fitting procedures used are described in more detail elsewhere.[7] The same method was employed

Table 3.2. Analytical Presentation of ZnPPIX PES Data

Ionization band		Half-Width (eV)		Relative Area		
label	**energy (eV)**	**high**	**low**	**He I**	**He II**	**He II/He I**
1	5.94	0.11	0.11			
2	6.06	0.12	0.12	1	1	1
3	6.18	0.13	0.11			
4	6.29	0.14	0.10			
5	6.40	0.18	0.14	0.30	0.30	1
6	6.60	0.21	0.21	0.89	0.55	0.62
7	6.78	0.57	0.10	0.25	0.25	1

in fitting ZnPPIX data: the He I spectrum was fit first, and the results were used to fit the He II spectrum.

Computational Details

Electronic structure calculations were carried out using GAUSSIAN 98[8] and Jaguar 4.1[9] programs. The porphin optimized geometry was obtained using Becke[10] three-parameter Lee-Yang-Parr[11] functional and 6-31G (d,p) basis set. Functional groups were added to the optimized porphin structure to generate PPIX; the geometry of PPIX was optimized using the same level of theory. The PPIX optimized geometry was used in generating a ZnPPIX structure, which was optimized employing a B3LYP/CEP[12]-31G(for Zn)/6–31G(d,p)(for C, N, O, H) level of theory. Single point energies were calculated using B3LYP/6-311G(d,p) for PPIX and B3LYP/CEP-121G(for Zn)/6-311(d,p)(for C, N, O, H) for ZnPPIX. λ^0 is the energy difference between the neutral singlet states of the molecules

Figure 3.2. Close-up He I (a) and He II (b) photoelectron spectra of PPIX. 2000 counts is collected for He I source (1500 for He II source).

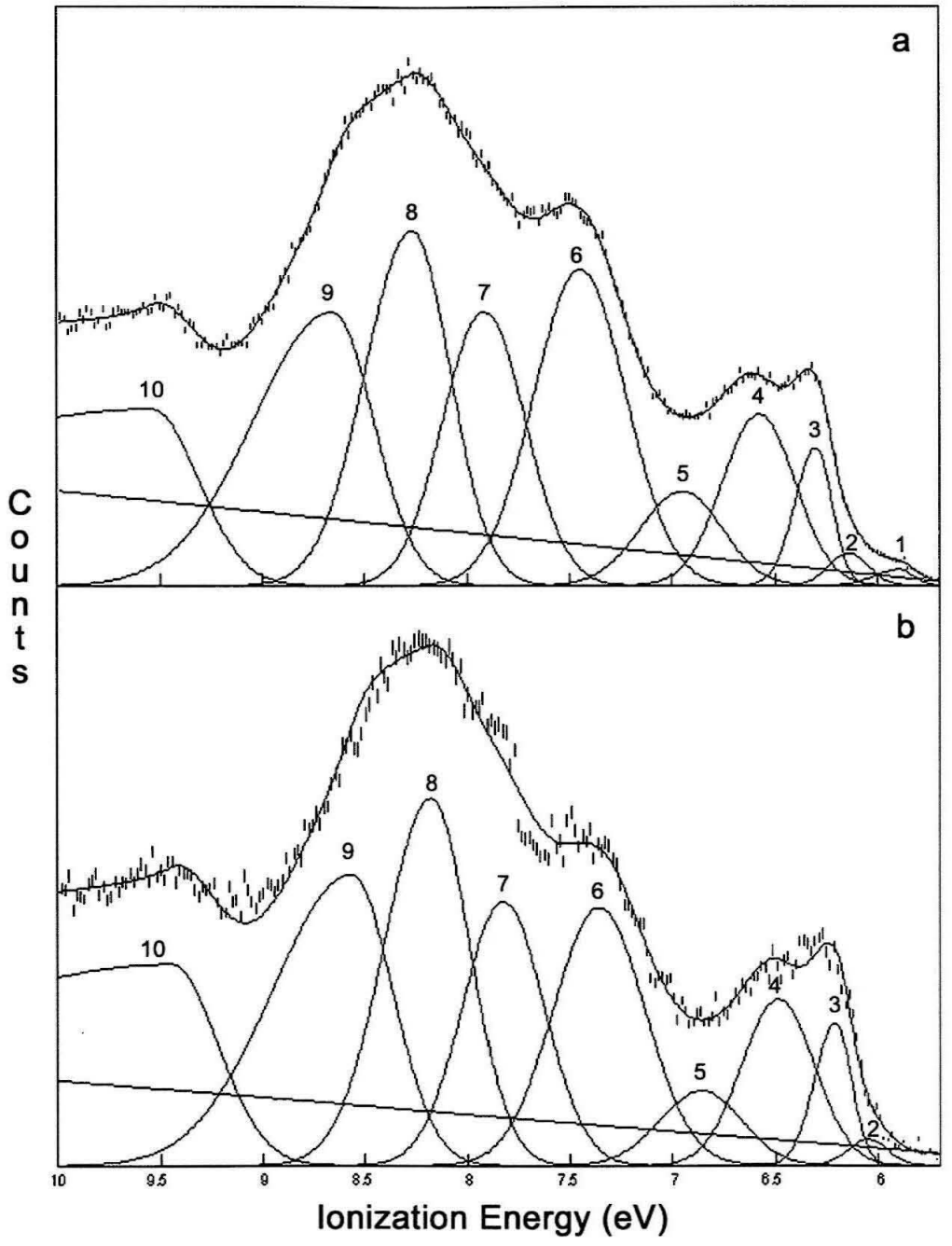
a
b
10
9
8
7
6
5
4
3
2
1
Counts
10
9.5
9
8.5
8
7.5
7
6.5
6
Ionization Energy (eV)

Figure 3.3. Close-up He I (a) and He II (b) photoelectron spectra of ZnPPIX. 2000 counts is collected for He I source (1500 for He II source).

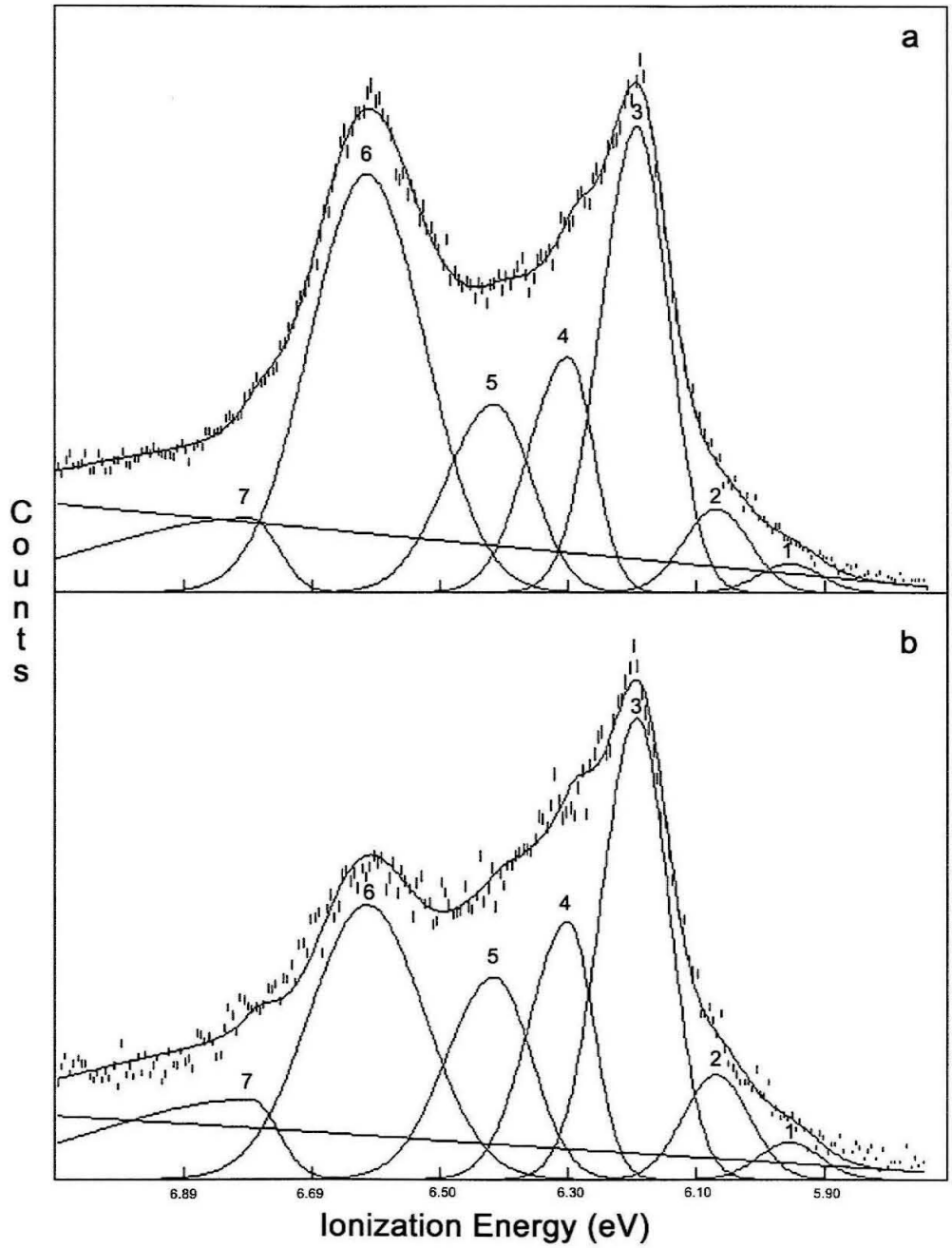
a
b
1
2
3
4
5
6
7
Counts
6.89
6.69
6.50
6.30
6.10
5.90
Ionization Energy (eV)

whose geometries were optimized for neutral and ionized states. Likewise, $\lambda^{+\bullet}$ is calculated as the energy difference between the cation doublet states of the molecules whose geometries were optimized for neutral and cation states. The sum of λ^{0} and $\lambda^{+\bullet}$ is the total reorganization energy, λ^{total}.

Results

Photoelectron Spectroscopy of PPIX and ZnPPIX

The full He I photoelectron spectra (5.1–15.3 eV) of PPIX and ZnPPIX are shown in Figure 3.1. The spectra are divided into three regions (I, II, and III),[13] where region I is between 5.8 and 7.2 eV. The first two porphyrin ionizations are located in region I. Region II is between 7.2 and 9.6 eV. Ionizations associated with the removal of electrons from the porphyrin ring and its substituents are located in region II. High binding energy ionizations found above 9.6 eV (region III) are predominantly associated with the removal of electrons from stable π and σ bonds. The assignment of ionization bands in regions II and III is difficult due to spectral congestion, but less complicated in region I. In high-valent metalloporphyrin complexes, metal *d* bands are usually found between regions I and II.[14]

The overlap of the ionization bands in regions I and II in He I and II spectra of PPIX prevented the recording of close-up spectra of region I. Instead, close-up spectra were obtained in the range 10.0–5.7 eV (Figure 3.2). The data were fit analytically and the results are presented in Table 3.1. The first two ionizations are located between 6 and 7 eV with

Table 3.3. Selected Bond Distances (Å) and Angles (deg) of PPIX and PPIXDME

Bonds[a]	PPIX[b]	PPIXDME[c]	Angles[a]	PPIX[b]	PPIXDME[c]
N-C_α	1.362[d]	1.367(9)[d]	C_α-N-C_α	110.7[d]	110.5(5)[d]
	1.372[e]	1.370(7)[e]		105.5[e]	105.4(5)[e]
C_m-C_α	1.397	1.386(9)	N-C_α-C_m	125.3	124.9(5)
C_β-C_α	1.443[d]	1.441(7)[d]	N-C_α-C_β	107.1[d]	106.9(5)[d]
	1.469[e]	1.452(7)[e]		111.4[e]	110.9(5)[e]
C_β-C_β	1.386[d]	1.360(7)[d]	C_α-C_β-C_β	107.6[d]	107.9(5)[d]
	1.369[e]	1.355(7)[e]		105.8[e]	106.5(5)[e]
C_β-C_{methyl}	1.498	1.498(8)	C_β-C_α-C_m	127.3[d]	127.7(6)[d]
C_β-C_{vinyl}	1.459	1.474(21)		123.6[e]	124.8(7)[e]
$C_{vinyl(\alpha)}$-$C_{vinyl(\beta)}$[f]	1.343	1.260(8)	C_α-C_m-C_α	127.5	128.1(8)
			C_α-C_β-C_{alkyl}	124.6	124.7(8)

[a] The notation C_α, C_β, C_m, C_{methyl}, C_{vinyl}, and C_{alkyl} describes positions of the carbon atoms in the molecule; i.e, α-, β-, or *meso*- positions. C_{alkyl} refers to the $-CH_3$ and $-(CH_2)_2CO_2H$ substituents.

[b] B3LYP calculation; this work.

[c] Ref. 15.

[d] The average for the amino pyrroles.

[e] The average for the imino pyrroles.

[f] C-C double bond.

distinct features labeled **3** and **4**. The Gaussian fit yields vertical ionization energies at 6.30 and 6.58 eV. There are a few more ionizations between 7 and 10 eV; and several Gaussian functions were used to represent these features best. However, it is hard to assign these bands to any particular ionization state due to the spectral congestion. It is most likely that they are generated by the removal of electrons from the low energy π orbitals of the

Figure 3.4. B3LYP/6-31G(d,p) optimized geometry parameters for PPIX.

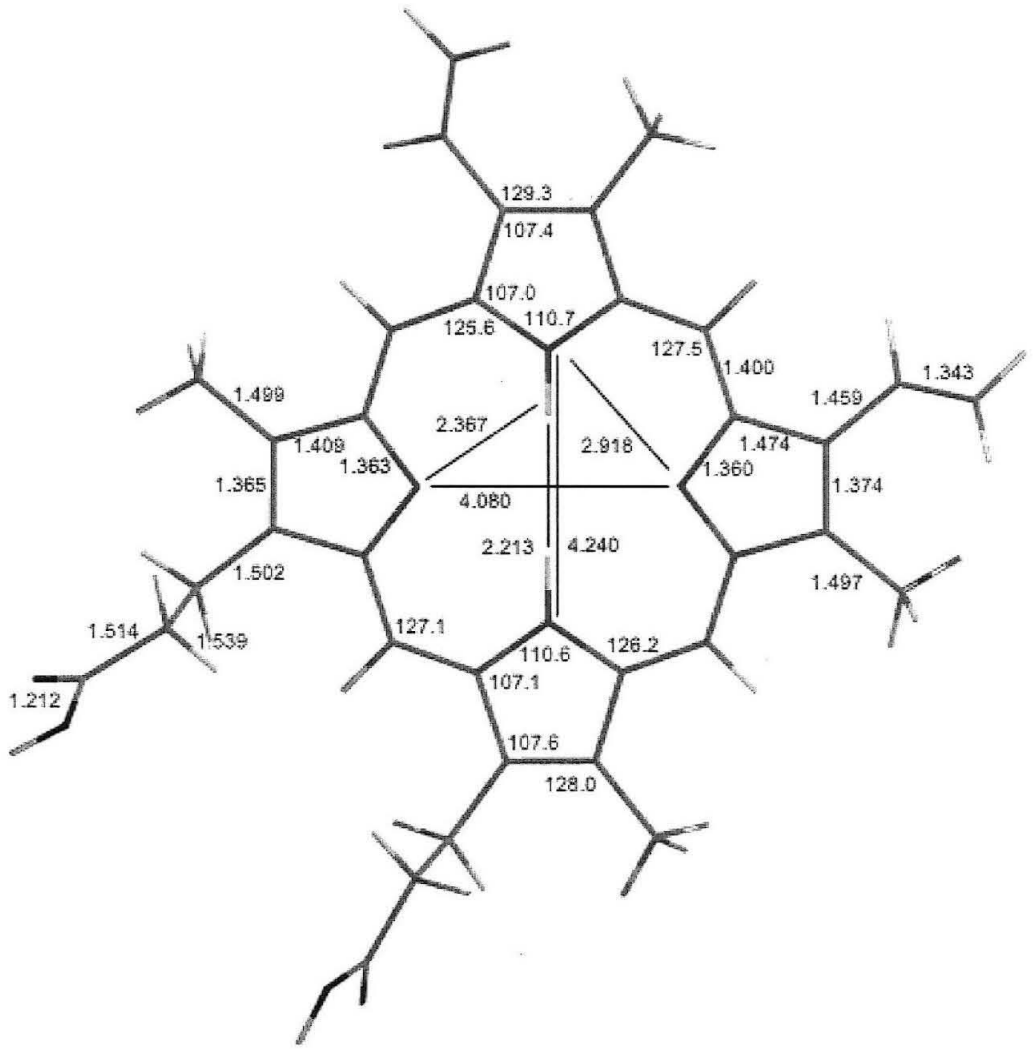
129.3
107.4
107.0
110.7
125.6
127.5
1.400
1.343
1.459
1.499
2.367
2.918
1.409
1.363
1.474
1.360
1.365
1.374
4.080
2.213
4.240
1.502
1.497
1.514
1.539
127.1
110.6
126.2
1.212
107.1
107.6
128.0

Figure 3.5. B3LYP/CEP-31G/6-31G(d,p) optimized geometry parameters for ZnPPIX.

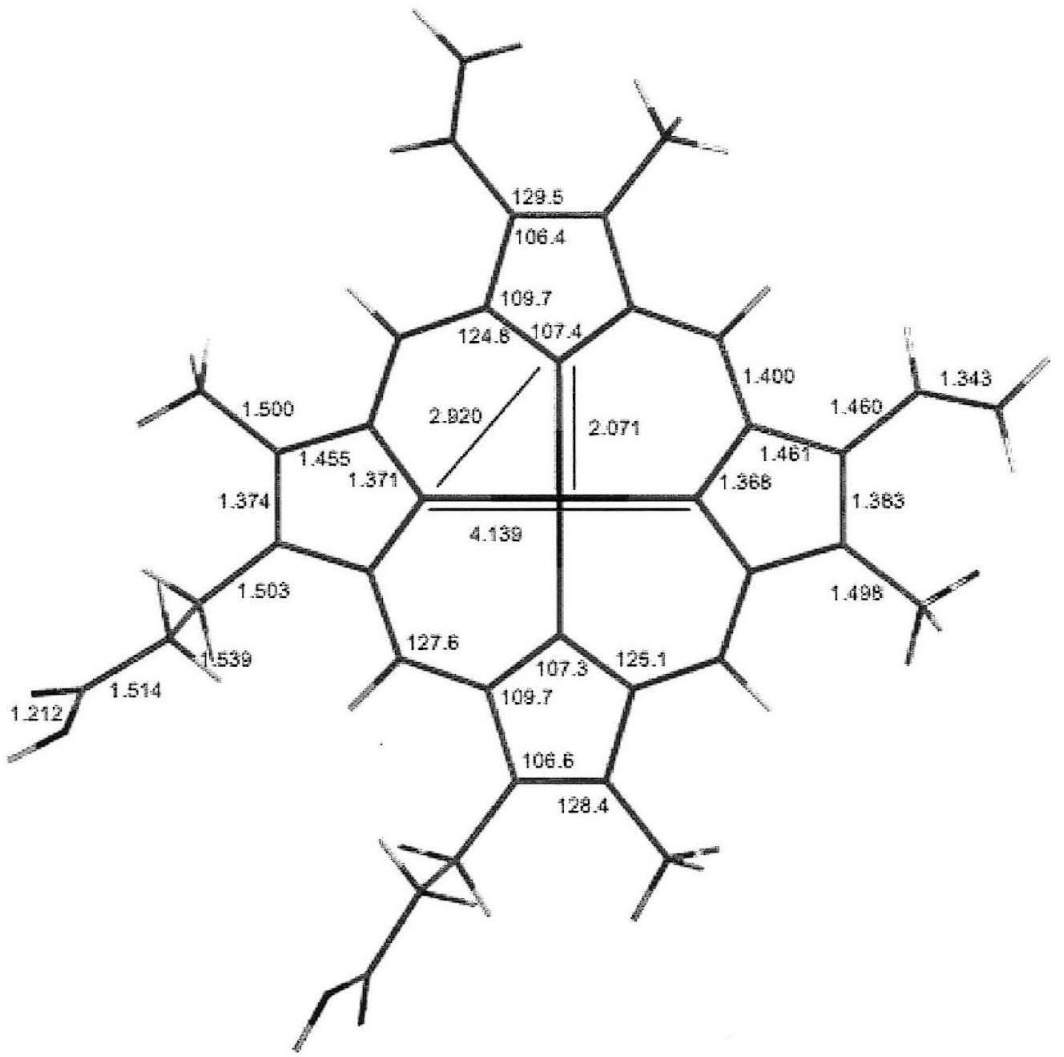
129.5
106.4
109.7
124.8
107.4
1.400
1.343
1.460
1.500
2.920
2.071
1.455
1.461
1.371
1.368
1.374
1.383
4.139
1.503
1.498
1.539
127.6
107.3
125.1
1.514
109.7
1.212
106.6
128.4

porphyrin ring and the vinyl substituents.

The first two ZnPPIX ionization bands in region I are well resolved and have little overlap with region II bands (Figure 3.3). These two distinct spectral features are labeled **3** and **6**, and they represent two vertical ionizations: 6.18 and 6.60 eV, respectively. A small shoulder on the high binding energy side of the first band is due to a partially resolved vibrational progression, and is fit with Gaussian **4**. The results of the analytical fit are presented in Table 3.2.

Computational Results

B3LYP optimized geometry parameters for PPIX and ZnPPIX are in Figures 3.4-3.5. The average PPIX bond distances and angles are compared to those of free base PPIX dimethyl ester (PPIXDME) obtained from the X-ray diffraction experiment (Table 3.3).[15] B3LYP/6-311G(d,p) calculation of PPIX yielded a b_{1u}-type orbital as the first HOMO; and an a_u-type orbital as the second HOMO (Figure 3.6). According to a B3LYP/CEP-121G(Zn)/6-311(d,p)(C, N, O, H) single point energy calculation, the first two HOMOs of ZnPPIX are of a_{1u} and a_{2u} symmetries (Figure 3.7). Even though neither PPIX nor ZnPPIX is a symmetric molecule, in each case the first two HOMOs resemble those of porphin. Therefore, D_{2h} symmetry designations were adopted for PPIX (D_{4h} for ZnPPIX).

Reorganization Energy of ZnPPIX

$$\lambda^{QM} = \sum_k h\nu_k S_k \qquad \text{Eq. 3.1}$$

The reorganization energy for PPIX was not obtained due to spectral congestion. The ZnPPIX experimental λ is the sum of λ^{QM} and λ^{SC} (reorganization energies obtained from quantum-mechanical (QM) and semiclassical (SM) analyses of photoelectron data).[4] Quantum-mechanical analysis of fine structure yields distortion parameters (S), which are related to λ^{QM} according to Eq. 3.1 (h is Planck's constant and ν_k is the vibrational frequency of mode k).[16] The first ionization band in the ZnPPIX He I spectrum exhibits a low-frequency vibrational progression spaced by 867 cm^{-1} (Figure 3.3).

We assume that the intensities of the individual Gaussian bands in the vibrational progression follow a Poisson distribution (Eq. 3.2, where I_n is the intensity of the n^{th}

$$I_n = \frac{S^n}{n!} e^{-S} \qquad \text{Eq. 3.2}$$

vibrational band).[17] Since only the first two vibrational bands are well resolved, the values of S were extracted from the ratio of I_1 to I_0.

$$G = |D|^2 e^{\frac{-(h\nu - IE)}{4k_B T\lambda^{SC}}} \qquad \text{Eq. 3.3}$$

Distortions along low-frequency modes and small frequency changes between the neutral and cation states can contribute to the breadth of individual vibronic lines in photoelectron spectra. Such band profiles are treated semiclassically (Eq. 3.3, IE is the ionization energy and D is related to the transition moment).[17]

$$T(\nu) = Ae^{-\alpha\left[\frac{(h\nu - p)}{H}\right]^2} \qquad \text{Eq. 3.4}$$

The Gaussian functions, $T(\nu)$, that were used to fit the experimental spectra (Eq. 3.4., in which A is the peak height, p is the peak position, H is the average full-width at half-maximum, and α is $4\ln(2))^7$ are convolutions of G (Eq. 3.3) and another Gaussian function, R, defined by the resolution of the instrument (Eq. 3.5).[18]

$$T(\nu) = \int_0^{\nu} G(x)R(x - \nu)dx \qquad \text{Eq. 3.5}$$

The value of H (the full-width at half-maximum) for the function G was obtained by

$$\lambda^{SC} = \frac{H^2}{16\ln(2)k_B T} \qquad \text{Eq. 3.6}$$

iterative reconvolution of the observed line-shape function and is related to λ^{SC}, according to Eq. 3.6. (Note that H for the function G is not the same as in Eq. 3.4.) The experimental and computational results are summarized in Table 3.4, where $\lambda^{+\bullet}$ is compared to the experimentally derived λ.

Discussion

According to Gouterman's four-orbital porphin model, the two highest occupied π orbitals are close in energy and the two lowest unoccupied π^* orbitals are degenerate.[19] Indeed, the photoelectron spectrum of porphin reveals that the first two ionizations are quasi-degenerate.[20] According to the calculation, one HOMO is an a_u orbital, which has significant electron density in the α- and β-positions on the porphyrin ring; and the other HOMO is a

Figure 3.6. The first two highest occupied molecular orbitals of PPIX. Top: The a_u-type orbital. Bottom: The b_{1u}-type orbital.

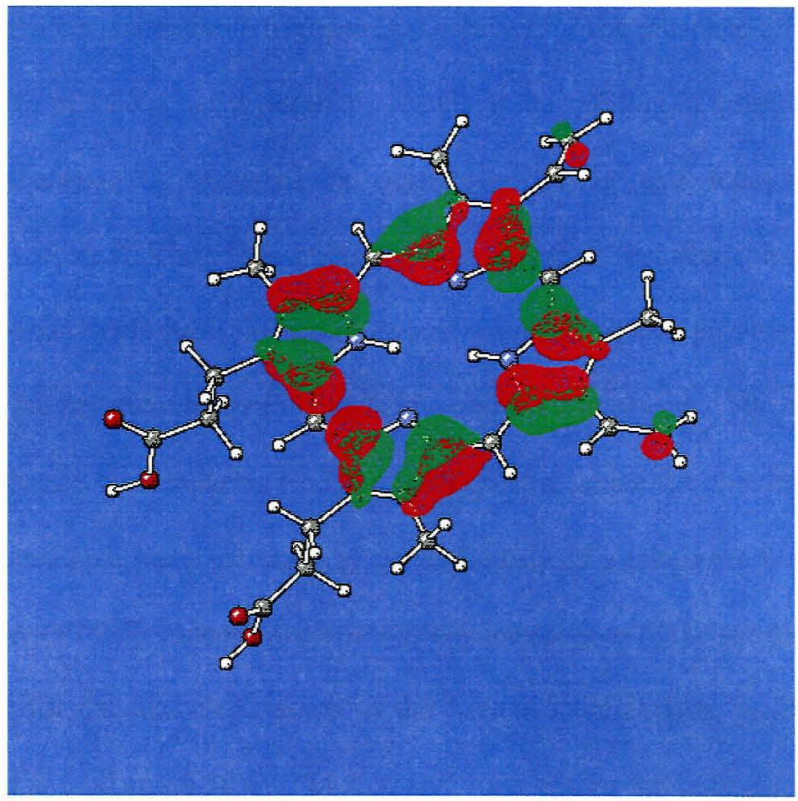

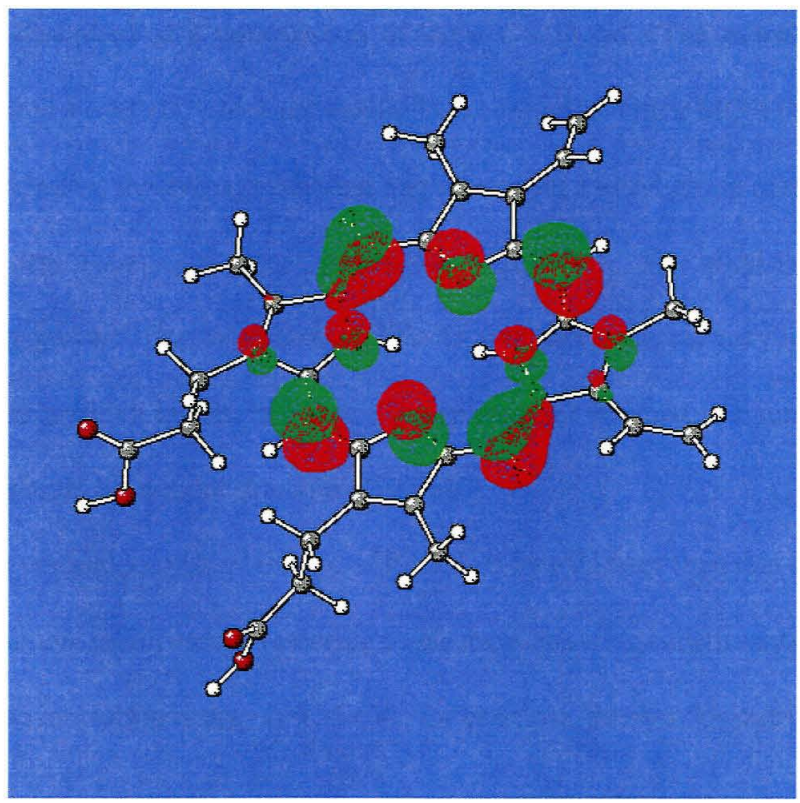

b_{1u} orbital, which has appreciable nitrogen 2p character.[21] The presence of substituents in either β- or *meso*-positions in the porphyrin results in the splitting of quasi-degenerate ^2A_u and $^2B_{1u}$ ionizations, as observed in octaethylporphyrin and tetraphenylporphyrin photoelectron spectra.[22] Therefore, understanding the effect that electron-donating and -withdrawing substituents have on the electronic structure of the porphyrin can aid the assignment of the first two ionization bands in a porphyrin spectrum. The assignment can be further confirmed by comparing He I and He II spectra, where the photoionization cross section of nitrogen 2p orbitals increases by approximately 25% relative to those of carbon.[23]

In the case of PPIX, inductive and mesomeric interactions of the substituents with the porphyrin ring lift the near-degeneracy of the first two ionizations, yielding two well-resolved bands at 6.30 and 6.58 eV. Methyl and vinyl groups are both electron-donating. Methyl substituents interact with the porphyrin ring through a 'classical' inductive effect, which is best described as a polarization of the σ C-C bond. The mesomeric effect is exhibited by vinyl π orbitals, which are available to conjugate with π MO's of the porphyrin (from our calculation, the average dihedral angle between a vinyl group and the porphyrin ring is 29.75 deg, allowing for conjugation between them). The alkyl substituents are electron-donating as well, but the presence of electron-withdrawing carboxylic acids possibly diminishes their positive inductive effect. The splitting of the first two ionizations in the ZnPPIX spectrum is even more dramatic: 0.42 eV.

The first vertical ionization energy of PPIX is 0.59 eV lower than that of porphin (6.9 eV).[20] The same ionization energy lowering by electron-donating substituents is observed in benzene (whose ionization energy is 9.25 eV); for example, the first ionization of toluene is

Figure 3.7. The first two highest occupied molecular orbitals of ZnPPIX. Top: The a_{1u}-type orbital. Bottom: The a_{2u}-type orbital.

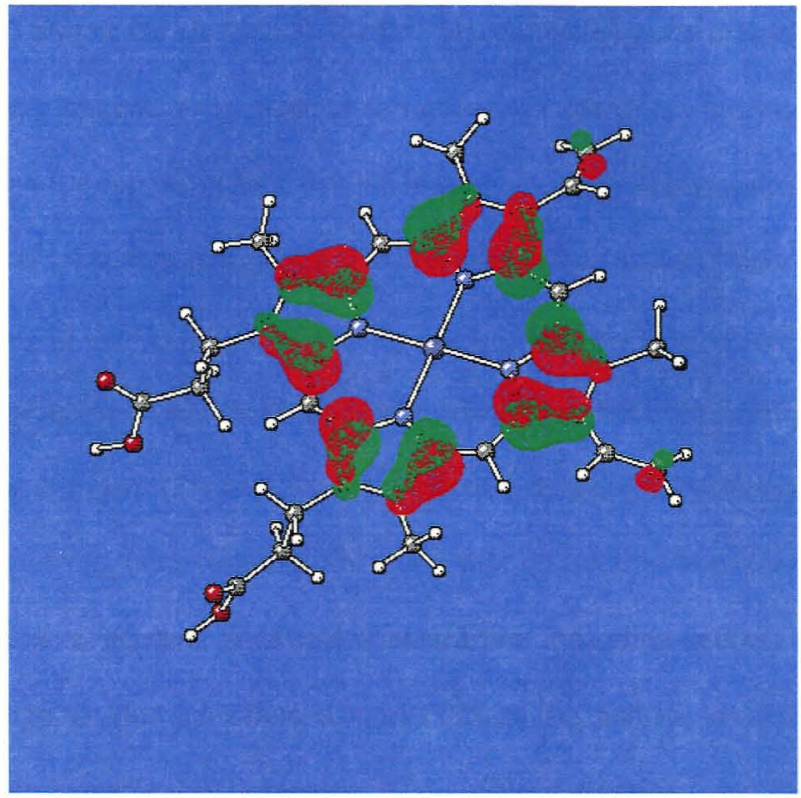

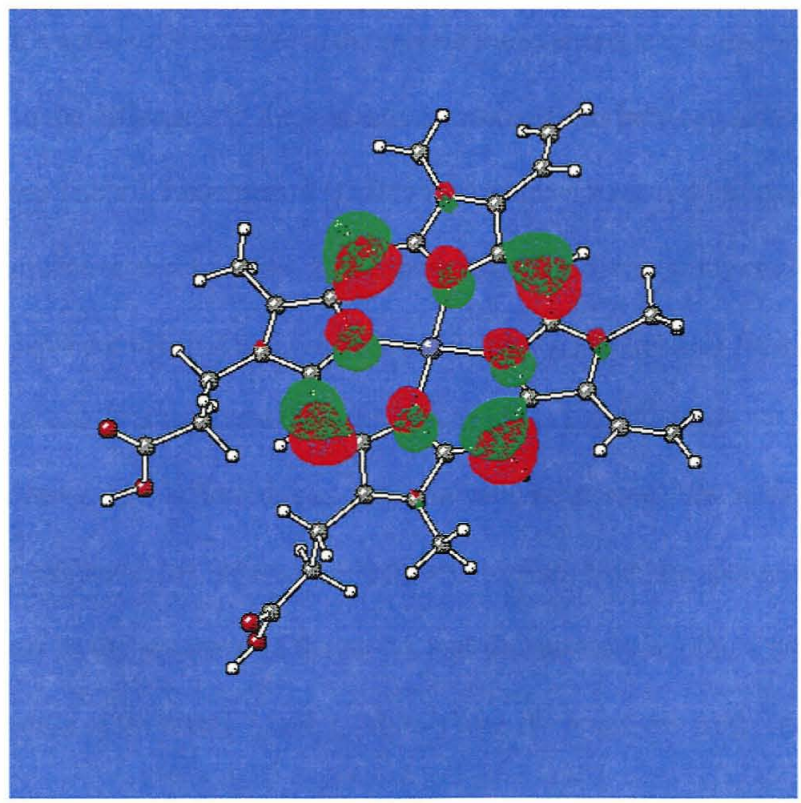

reported at 8.83 eV and the second at 9.36 eV.[24] Since a methyl group makes a benzene ring more 'negative', less energy is required to remove a π electron. Electron-withdrawing substituents have the opposite effect: the first ionization energy of benzonitrile is 9.71 eV.[24] The first vertical ionization energy of ZnPPIX is even lower (6.18 eV) than that of PPIX.

According to the PPIX B3LYP results, the a_u orbital is characterized by significant electron density on the α- and β-carbons, and the b_{1u} has appreciable density on the *meso*-carbons and the nitrogens (Figure 3.6). Since electron-donating substituents in β-positions make a porphyrin ring more negative, the removal of an electron from the destabilized a_u orbital to produce a ^2A_u state yields the observed low ionization energy. Therefore, we tentatively assign the first ionization state of PPIX as ^2A_u, and the second as $^2B_{1u}$. This assignment is in agreement with previous UV-visible absorption[25] and PES[22] studies of substituted free base porphyrins. If the assignment is correct, then the He II spectrum (Figure 3.2) will exhibit a noticeable increase in the second ionization relative area compared to that of the first due to the difference in the ionization cross sections between nitrogen and carbon 2p orbitals. From Table 3.1 the ratio of He II to He I relative areas is 1.08; thus, the expected change in the ionization cross section is not observed. This discrepancy could be due to the small splitting between the first two ionizations (0.28 eV), and the near proximity of region II bands, both of which complicate the comparison of He I and II data.

When a metal ion is introduced into the porphyrin ring, the same two types of interactions are expected: the inductive effect, which arises from the change of the nitrogen atoms' potentials in the presence of the metal, and the mesomeric effect, which originates from the interaction of the metal d_π and p_π orbitals with the porphyrin ring. In addition, there

are also inductive and mesomeric effects from the organic substituents on the porphyrin ring. Gouterman's four-orbital-model-parameter analyses of UV-visible absorption spectra of a series of metals incorporated into substituted porphyrins suggest that the a_{1u} orbital is higher in energy than the a_{2u} orbital for β-substituted metalloporphyrins.[25] This ordering is supported by detailed EPR studies of one-electron oxidized Zn(II) and Mg(II) octaethylporphyrins that show that an electron is removed from the a_{1u} orbital in each case.[26] Thus, both UV-visible and EPR results indicate that metal inductive and mesomeric effects are less significant than those of the organic peripheral substituents, and the ordering of the orbitals in divalent metalloporphyrins is the same as in the free base porphyrins.

In the four-orbital model, an A_{1g} parameter defines the separation of a_{1u} and a_{2u} orbitals. In solution, A_{1g} corrected for A_{1g}'' (the off-diagonal matrix element represented by two-electron exchange integral mixing the excited-state configurations) was found to be 0.15 eV for ZnPPIX.[27] Likewise, other A_{1g} parameters for substituted metalloporphyrins were found to be small.[27] Our ZnPPIX photoelectron results, however, show a greater splitting, 0.42 eV, in the gas phase, suggesting that substituent effects of the metal are equally important as the ones of peripheral alkyl groups. Since metal d_π and p_π orbitals are not energetically available to mix with the a_{2u} porphyrin orbital, the zinc mesomeric effect is negligible. However, the inductive effect of zinc substitution is more significant: in ZnPPIX, six sigma electrons from the nitrogen atoms and the two metal electrons complete the valence shell, i.e., Zn has a formal charge of 2+ and the porphyrin ring of 2-. As a consequence, the first experimental ionization energy is low, 6.18 eV, in comparison to that of PPIX. Also, the negative charge on the porphyrin ring may be delocalized onto the vinyl substituents, which would lower the

a_{1u} orbital energy relative to that of a_{2u}. Since the metal ion interacts directly with the a_{2u} orbital, we conclude that $^2A_{2u}$ is the ground electronic state of ZnPPIX, and $^2A_{1u}$ is the first excited electronic state. The orbital assignment is easily verified by examining the He II spectrum (Figure 3.3): the analysis of He II data shows that the relative area of the first ionization increased by approximately 60% in comparison to that of He I for the same ionization (Table 3.2). This confirms our assignment of the region I photoelectron spectrum

Table 3.4. Reorganization Energies (meV) of PPIX (**1**) and ZnPPIX (**2**)

	$\Delta\nu$ (cm^{-1})[a]	S	λ^{QM}	λ^{SC}	λ^{b}	$\lambda^{+\bullet}$	λ^{0}	λ^{total}
1	-	-	-	-	-	131	117	248
2	867±34[d]	0.507±0.018[e]	124±3	17±1	141±3	56	83	139

[a] $\Delta\nu$ is the vibrational spacing.

[b] $\lambda = \lambda^{QM} + \lambda^{SC}$.

[c] $\lambda^{total} = \lambda^{+\bullet} + \lambda^{0}$.

[d] The error in the vibrational spacing was determined by fitting 10 individual scans of photoelectron spectra of ZnPPIX.

[e] The value of S was obtained according to the expression: $S=(I_1\pm\Delta I_1)/(I_0\pm\Delta I_0)$ where ΔI_n is the square root of I_n.

of ZnPPIX.

The B3LYP optimized geometry of PPIX is in good agreement with experimental bond distances and angles of PPIXDME obtained from the X-ray diffraction experiment (Table 3.3).[15] The only discrepancy is in C-C double bond distances for the vinyl substituents. Both calculation and experiment yield planar porphyrin rings. Introduction of Zn into the

porphyrin ring resulted in slight changes in the porphyrin geometry, which are primarily manifested in an expansion of the ring size (Figures 3.4-3.5). The average calculated Zn-N bond distance, 2.071 Å, is similar to that in Zn(II)porphyrin, 2.058 Å.[21] The bond distances and angles for the peripheral substituents on the porphyrin ring for the most part are the same in PPIX and ZnPPIX. Introduction of the metal into the ring did not change the ring planarity and the average dihedral angle between the vinyl groups and the porphyrin is the same as in PPIX.

Quantum-mechanical and semiclassical analyses of the ZnPPIX spectrum yielded 141±3 meV for the reorganization energy of cation formation in the gas phase. B3LYP calculation yields 56 meV for $\lambda^{+\bullet}$, which is approximately 90 meV lower that the experimental result. Even though B3LYP/CEP-121G(for Zn)/6-311(d,p)(for C, N, O, H) produced excellent optimized geometries, it is not uncommon for the density functional theory energies to be lower that the experimental values. The difference in energy between $\lambda^{+\bullet}$ and λ^{0} is approximately 20 meV, which indicates that the curvatures of the experimental parabolic surfaces for the cation and neutral states are nearly the same. Therefore, the total experimental reorganization energy for the self-exchange reaction of ZnPPIX is 282±3 meV. With the assumption that solvent molecules do not perturb any of the internal modes involved in the self-exchange reaction, this result can be compared to the previously reported inner-sphere reorganization energies in ruthenium-modified proteins, e.g., Ru-Zn-cytochrome *c*.[28] The rate and the free energy change for the intramolecular ET reaction, $Ru(NH_3)_4(py)(His^{33})^{2+} \rightarrow ZnP^{+}$, are 3.5(4) x 10^5 s^{-1} and 0.75(5) eV, respectively, yielding 1.19 eV for the total reorganization energy.[28] The inner-sphere contribution to the total

reorganization energy estimated from structural changes in Ru(II)-ammine and Zn-porphyrin complexes was found to be no greater than 0.2 eV, where the inner-sphere configurational changes in the Zn(II)porphyrin were estimated to be 0.15 eV.[29] This crude estimate is in excellent agreement with the direct measurement of the reorganization energy of ZnPPIX from the photoelectron spectrum. Measurement of the rates and driving forces for the Ru(II) → Fe(III) intramolecular reactions yielded 1.2 eV for the reorganization energy, which is quite similar to the value observed in the Zn case.[28] Therefore, we expect that the value for the reorganization energy of Fe(II)PPIX will be similar to that of ZnPPIX.

The calculated PPIX reorganization energy is 248 meV, which is approximately two fold greater than that of ZnPPIX (Table 3.4). Due to the spectral congestion in region I of the PPIX spectrum, an experimental value of λ is not available for comparison to the calculated result. It is reasonable to assume that the experimental result will not be 100 meV greater than the calculated value.

Conclusion

We have assigned the region I photoelectron spectrum of ZnPPIX: the ground electronic state is $^2A_{2u}$ (the tentative assignment for PPIX is ^2A_u). ZnPPIX experimental results suggest that an inductive substituent effect of the metal ion is important in determining the order of the electronic states in metalloporphyrin photoelectron spectra. A fine structure analysis of the ZnPPIX spectrum yielded 141±3 meV for the reorganization

energy, which is in excellent agreement with λ_i values for ruthenium-modified proteins.

References and Notes

(1) Kadish, K. M.; Smith, K. M.; Guilard, R., Ed. *The Porphyrin Handbook*; Academic Press: London, **2000**; Vol. 4.

(2) Balzani, V., Ed. *Electron Transfer in Chemistry*; Wiley-VCH Verlang GmbH: D-69469 Weinheim, Germany, **2001**; Vols. 1-5.

(3) Marcus, R. A.; Sutin, N. *Biochim. Biophys. Acta* **1985**, *811*, 265-322.

(4) Amashukeli, X.; Winkler, J. R.; Gray, H. B.; Gruhn, N. E.; Lichtenberger, D. L. *J. Phys. Chem. B* **2002**, in press.

(5) Westcott, B. L.; Gruhn, N. E.; Enemark, J. H. *J. Am. Chem. Soc.* **1998**, *120*, 3382-3386.

(6) Turner, D. W.; Baker, C.; Baker, A. D.; Brundle, C. R. *Molecular Photoelectron Spectroscopy*; Wiley-Interscience; London, **1970**.

(7) Lichtenberger, D. L.; Copenhaver, A. S. *Electron Spectrosc. Relat. Phenom.* **1990**, *50*, 335-352.

(8) GAUSSIAN 98, Revision A.9, Frisch, M. J.; Trucks, G. W.; Schlegel, H. B.; Scuseria, G. E.; Robb, M. A.; Cheeseman, J. R.; Zakrzewski, V. G.; Montgomery, Jr.,J. A.; Stratmann, R. E.; Burant, J. C.; Dapprich, S.; Millam, J. M.; Daniels, A. D.; Kudin, K. N.; Strain, M. C.; Farkas, O.; Tomasi, J.; Barone, V.; Cossi, M.; Cammi, R.; Mennucci, B.; Pomelli, C.; Adamo, C.; Clifford, S.; Ochterski, J.; Petersson, G. A.; Ayala, P. Y.; Cui, Q.;

Morokuma, K.; Malick, D. K.; Rabuck, A. D.; Raghavachari, K.; Foresman, J. B.; Cioslowski, J.; Ortiz, J. V.; Baboul, A. G.; Stefanov, B. B.; Liu, G.; Liashenko, A.; Piskorz, P.; Komaromi, I.; Gomperts, R.; Martin, R. L.; Fox, D. J.; Keith, T.; Al-Laham, M. A.; Peng, C. Y.; Nanayakkara, A.; Challacombe, M.; Gill, P. M. W.; Johnson, B.; Chen, W; Wong, M. W.; Andres, J. L.; Gonzalez, C.; Head-Gordon, M.; Replogle, E. S.; and Pople, J. A. Gaussian, Inc.: Pittsburgh PA, **1998**.

(9) Jaguar version 4.1, Schrödinger Inc.: Portland, OR, **2000**.

(10) Becke, A.D. J. Chem. Phys. **1993**, *98*, 5648-5652.

(11) Lee, C.; Yang, W.; Parr, R. G. Phys. Rev. B **1988**, *37*, 785-789.

(12) CEP is a core effective potential.

(13) (a) Khandelwal, S. C.; Robber, J. L. *Chem. Phys. Lett.* **1975**, *34*, 355.; (b) Kitagawa, S.; Morishima, I.; Yonezawa, T.; Sato, N. *Inorg. Chem.* **1979**, *18*, 1345-1349.

(14) Westcott, B. L.; Gruhn, N. E.; Michelsen, L. J.; Lichtenberger, D. L. *J. Am. Chem. Soc.* **2000**, *122*, 8083-8084.

(15) Caughey, W. S.; Ibers, J. A. *J. Am. Chem. Soc.* **1977**, *99*, 6639-45.

(16) Brunschwig, B. S.; Sutin, N. *Comments Inorg. Chem.* **1987**, *6*, 209-235.

(17) Ballhausen, C. J. *Molecular Electronic Structures of Transition Metal Complexes*; McGraw-Hill, Inc.: UK, **1979**; p. 125.

(18) Press, W. H.; Flannery, B. P.; Teukolsky, S. A.; Vetterling, W. T. *Numerical Recipes, The Art of Scientific Computing, (Fortran Version)*; Cambridge University Press: New York, NY, **1989**; p.383.

(19) Gouterman, M.; Dolphin, D., Ed. *The Porphyrins*; Academic Press; New York,

1978; Vol. 3.

(20) Dupuis, P.; Roberge, R.; Sandorfy, C. *Chem. Phys. Lett.* **1980**, *75*, 434-437.

(21) Ghosh, A; Kadish, K. M.; Smith, K. M.; Guilard, R., Ed. *The Porphyrin Handbook*; Academic Press: London, **2000**; Vol. 7, pp 1-38.

(22) Gruhn, N. E.; Lichtenberger, D. L.; Ogura, H.; Walker, F. A. *Inorg. Chem.* **1999**, *38*, 4023-4027.

(23) Yeh, J. J.; Lindau, I. *At. Data Nucl. Data Tables* **1985**, *32*, 1. (According to Gelius model, the atomic orbital cross sections are additive in molecular orbitals (Gelius, U. *J. Electron Spectrosc. Relat. Phenom.* **1975**, *5*, 985.).

(24) Kimura. K. *Handbook of He I Photoelectron Spectra of Fundamental Organic Molecules*; Japan Scientific Societies Press: Tokyo, **1981**.

(25) Spellane, P. J.; Gouterman, M.; Antipas, A.; Kim, S.; Liu, Y. C. *Inorg. Chem.* **1980**, *19*, 386-391.

(26) Fajer, J.; Borg, D. C.; Forman, A.; Felton, R. H.; Vegh, L.; Dolphin, D. *Ann. N. Y. Acad. Sci.* **1975**, *244*, 349-364.

(27) Shelnutt, J. A.; Ortiz, V. *J. Phys. Chem.* **1985**, *89*, 4733-4739.

(28) Winkler, J. R.; Gray, H. B. *Chem. Rev.* **1992**, *92*, 369-379.

(29) Meade, T. J.; Gray, H. B.; Winkler, J. R. *J. Am. Chem. Soc.* **1989**, *111*, 4353-4356.

Chapter 4

Inner-Sphere Reorganization Energies of Metalloporphyrins: Computational Study

Introduction

Cytochromes are a class of heme electron-transfer proteins; the active site of a cytochrome consists of an iron ion (e.g, Fe^{II}, Fe^{III}) bound to the porphyrin, and two axial ligands that complete the octahedral coordination sphere.[1] Biological classification of cytochromes (e.g., cytochromes *a*, *b*, *c*, *f*) is based on the type of substituents on the porphyrin ring, the axial ligands, and the number and arrangements of the heme groups in a protein.[2] Histidine (His) and methionine (Met) are the most common axial ligands, but proteins with tyrosine (Tyr) are known as well.[3] In addition, there are five-coordinate heme proteins, but their functions are catalysis and transport rather than electron transfer.[3]

According to semiclassical ET theory, reaction rates depend on reorganization energy, λ (where $\lambda = \lambda_i + \lambda_o$, the sum of inner- and outer-sphere contributions).[4] For cytochromes, λ_i is associated with the structural changes in the first coordination sphere of the metal, and λ_o constitutes structural changes in the surrounding polypeptide and the solvent. The inner-sphere contribution to ET rates is considered small in comparison to the outer-sphere component;[5] however, values of λ_i indicate whether a particular protein can efficiently facilitate the transfer of electrons. These considerations motivated us to calculate and compare reorganization energies for a series of six-coordinate iron and cobalt porphyrin model complexes.

Methods

Electronic structure calculations were carried out using Jaguar 4.1 program.[6] The geometries were optimized using the Becke three-parameter Lee-Yang-Parr functional. B3LYP consists of the hybrid exchange functional proposed by Becke[7] and the Lee-Yang-Parr correlation functional.[8] The basis sets used in these calculations were core-effective potential (CEP), CEP-31G, for the metal ions, and 6-31G(d,p) (a split-valence basis set with d-type Gaussian polarization wavefunctions on C, N, O, and S atoms, and a set of p-type Gaussian polarization functions on H atoms). The same level of theory was used to calculate reorganization energies.

Model complexes consist of metal octamethylporphyrin with two axial ligands: SH_2, imidazole, and C6H5O$^-$ as models for Met, His, and Tyr. In the case of iron, all complexes were assumed to be in a low-spin state (i.e., a singlet for Fe^{II}, and a doublet for Fe^{III}). In the case of cobalt, Co^{II} complexes were doublets, and Co^{III} complexes were singlets. The reorganization energy for the reduced complexes, λ^{red}, was calculated as the difference between energy of the M^{II} state in its optimal geometry and the energy of the M^{II} complex calculated at the M^{III} optimized geometry. Similarly, the reorganization energy for the oxidized complex, λ^{ox}, was calculated as the energy of the M^{III} complex in its optimal geometry minus the energy of the M^{III} state in the geometry optimized for the reduced complex. The total, self-exchange reorganization energy, λ, is the sum of λ^{red} and λ^{ox}.

Reorganization energies were also calculated for free base porphin and methyl-, ethyl-, and tetraphenyl-substituted porphyrins using B3LYP/6-31G(d,p) level of theory. Values of

Table 4.1. Calculated[a] and Experimental Fe-Ligand Bond Lengths (Å)

axial ligand (L)		oxidation state	Fe-L (calculated/experimental)			reference
1	2		N_{por}	L 1	L 2	
His	His	III	-/1.97-2.00	-/2.00	-/2.08	9
Im[b]	Im	II	2.03/2.00	2.07/2.01	2.07/2.01	10
		III	2.02/1.99-2.00	2.07/1.96	2.07/1.99	11
Met	Met	III	-/2.01-2.02	-/2.64	-/2.69	12
SR_2[c]	SR_2	II	2.02/2.00	2.44/2.34	2.44/2.34	13
		III	2.01/1.98	2.43/2.33	2.43/2.35	13

[a] this work.

[b] Im stands for imidazole.

[c] R is H in this work.

λ^0 and $\lambda^{+\bullet}$ were calculated as described in detail in Chapters 2 and 3. The sum of λ^0 and $\lambda^{+\bullet}$ is the total reorganization energy, λ^{total}, for a self-exchange reaction.

Results and Discussion

Geometries of Porphyrins in Cytochromes

The optimized geometry of free base protoporphyrin IX is described in Chapter 3. In this work, we found no significant changes in porphyrin ring geometry associated with different peripheral substituents. Selected bond lengths and angles for the neutral six-coordinate metalloporphyrins are presented in Figures 4.1-4.4. Reduced and oxidized

Table 4.2. Reorganization Energies (meV) of Free Base Porphyrins

molecule	λ^0	$\lambda^{+\bullet}$	λ^{total}
porphin[a]	21	29	50
octamethylporphyrin[a]	27	34	61
(1,3-ethyl)methylporphyrin[a]	107	163	270
tetraphenylporphyrin[a]	58	67	125
protoporphyrin IX[b]	117	131	248

[a] Calculated with B3LYP/6-31G(d,p).

[b] Calculated with B3LYP/6-311G(d,p).

geometries of iron model complexes are compared to experimental values in Table 4.1. There is favorable agreement between calculated and experimental structural parameters of model complexes; on average, our calculated bond lengths are 0.03 Å greater than the experimental values. Remarkably, there is little difference between actual cytochrome heme geometries and those of the model complexes.

Reorganization Energies of Porphyrins

Calculated free base porphyrin reorganization energies are summarized in Table 4.2. When a π electron is removed from a porphyrin, the charge is delocalized over the porphyrin ring. Therefore, introduction of methyl groups in β-positions will yield an insignificant change between neutral and cation geometries. This is reflected in a small difference, 11 meV, in reorganization energies between porphin and octamethylporphyrin. Surprisingly, introduction of ethyl groups in 1- and 3-β positions of methylated porphyrin causes a dramatic five-fold increase in λ^{total} in comparison to that of porphin. Likewise,

Figure 4.1. B3LYP optimized geometry of Fe(imidazole)$_2$octamethylporphyrin (closed-shell, singlet).

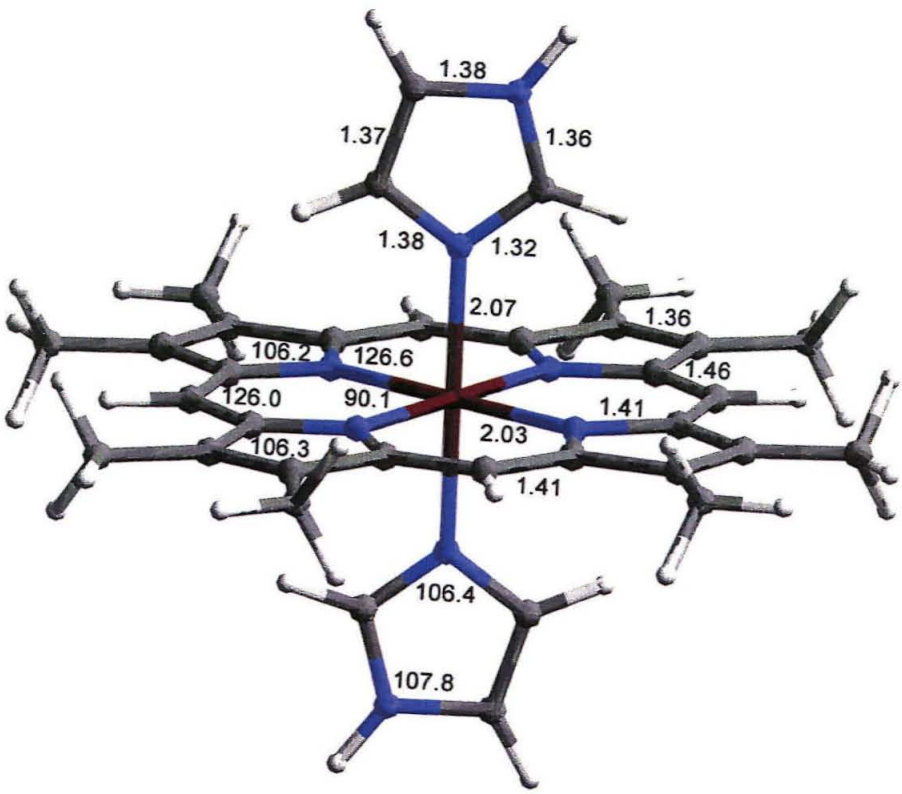
1.38
1.37
1.36
1.38
1.32
2.07
1.36
106.2
126.6
1.46
126.0
90.1
1.41
2.03
106.3
1.41
106.4
107.8

Figure 4.2. B3LYP optimized geometry of $Fe(SH_2)_2$octamethylporphyrin (closed-shell, singlet).

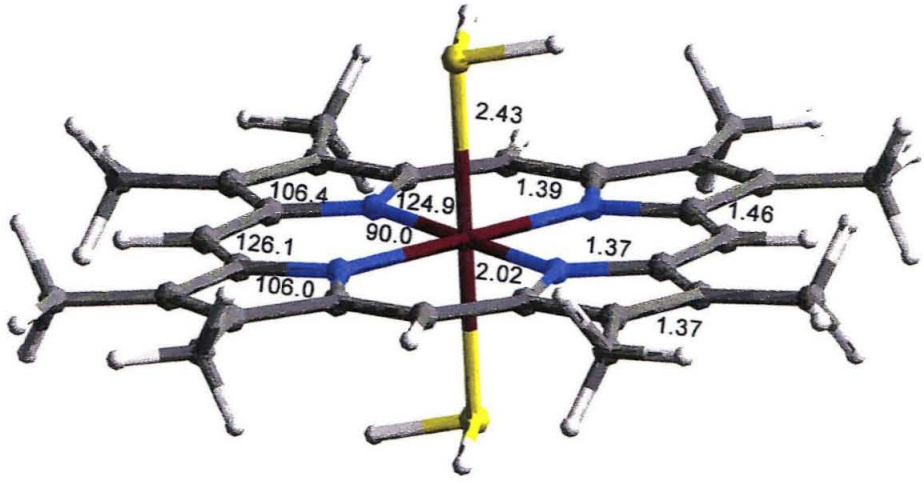
2.43
106.4
124.9
1.39
1.46
90.0
126.1
1.37
2.02
106.0
1.37

Figure 4.3.a. B3LYP optimized geometry of $Fe(C_6H_5O)$(imidazole)octamethylporphyrin (oxidation state of iron is III; closed-shell, doublet).

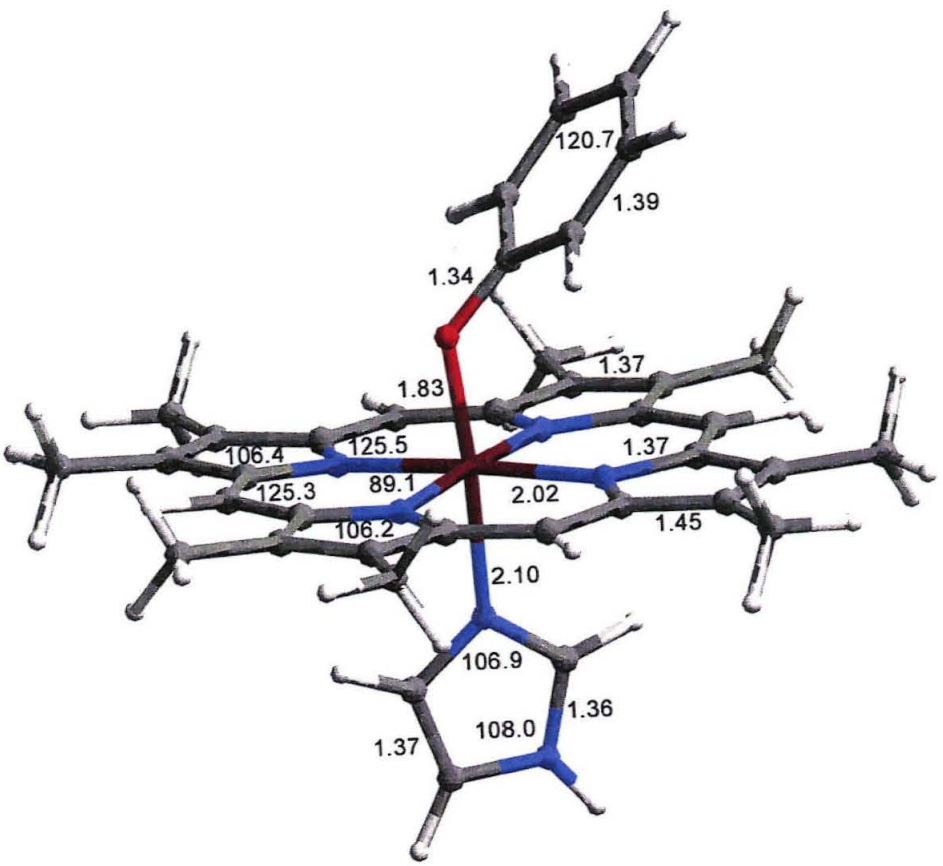
120.7
1.39
1.34
1.37
1.83
106.4
125.5
1.37
125.3
89.1
2.02
106.2
1.45
2.10
106.9
1.36
108.0
1.37

Figure 4.3.b. B3LYP optimized geometry of $Fe(C_6H_5O)$(imidazole)octamethylporphyrin (oxidation state of iron is III; closed-shell, doublet), showing dihedral angle of 179.4 deg.

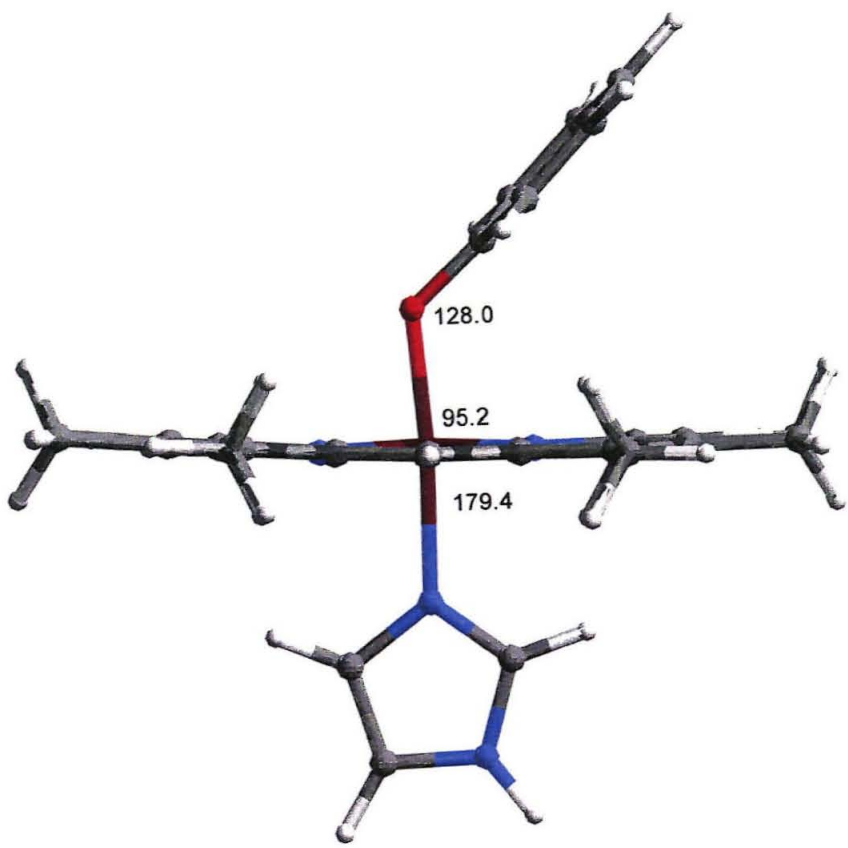
128.0
95.2
179.4

Figure 4.4. B3LYP optimized geometry of Co(imidazole)$_2$octamethylporphyrin (closed-shell, doublet).

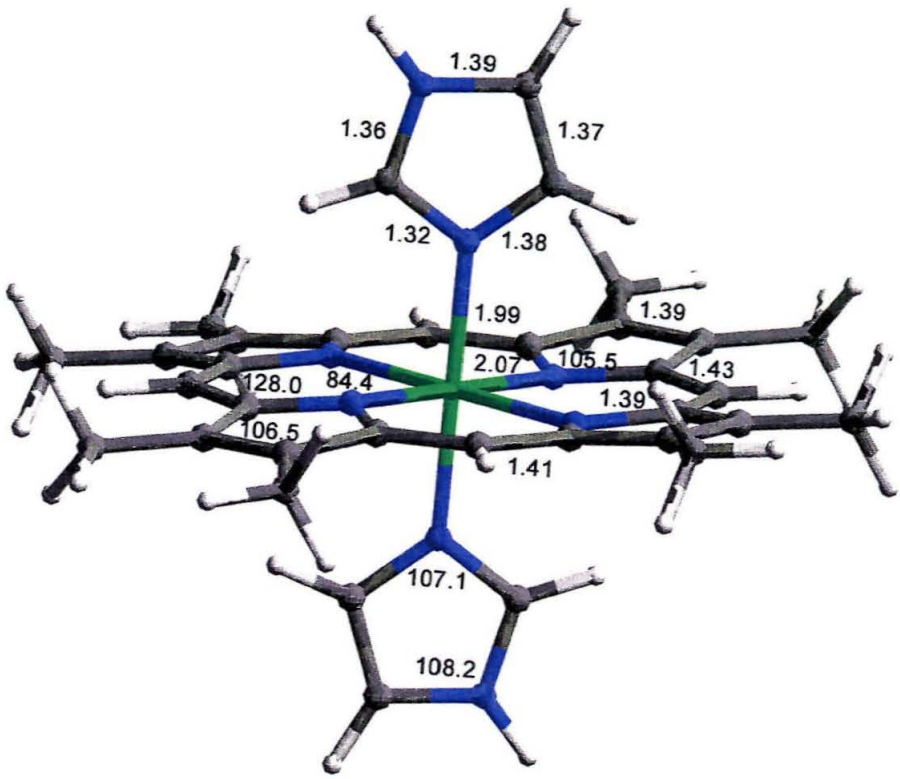
1.39
1.36
1.37
1.32
1.38
1.99
1.39
2.07
105.5
1.43
128.0
84.4
1.39
106.5
1.41
107.1
108.2

the reorganization energy of protoporphyrin IX calculated with B3LYP/6-311G(d,p) level of theory is 248 meV. Introduction of four phenyl groups in *meso*-positions yields value of λ^{total} which is in between those of porphin and protoporphyrin IX. In all cases, λ^{0} and $\lambda^{+\bullet}$ are different by at least 9 meV, which indicates that curvatures of the energy surfaces are nearly equivalent for equilibrium geometries of neutral molecules and their cations.

Reorganization Energies of Iron and Cobalt Porphyrins

Calculated reorganization energies of metalloporphyrins are listed in Table 4.3. The common His-His axial ligands combination is found in many *a*-, *b*-, and *c*-type cytochromes.[3] The calculated reorganization energy of the iron-*bis*(imidazole) complex is 110meV (Figure 4.5), which is consistent with small geometry changes between the reduced and oxidized forms of the cytochrome found crystallographically (Table 4.1). λ^{red} and λ^{ox} are different, which indicates that the curvatures of energy surfaces are not equivalent for equilibrium geometries of reduced and oxidized forms of this molecule. The reorganization energy of the cobalt-*bis*(imidazole) complex, 449 meV, is significantly larger. Unlike its iron analog, the porphyrin ring in the cobalt model system is not planer, the positions of peripheral methyl groups in the reduced complex change when cobalt is oxidized (Figure 4.6). Moreover, a substantial increase in Co-$N_{imidazole}$ bond length is calculated from the oxidized to the reduced forms, contributing to the large reorganizations energy. Therefore, reorganization energies in low-valent metal-*bis*(imidazole) porphyrins are primarily metal-centered (i.e., λ is associated primarily with changes in metal-N bond lengths). This observation contrasts with the case of high-valent iron porphyrins, as found in peroxidase compounds I and II, where

Figure 4.5. Overlay of B3LYP optimized geometries of reduced (green) and oxidized (red) forms of Fe(imidazole)$_2$octamethylporphyrin, showing minor changes in bond lengths and angles.

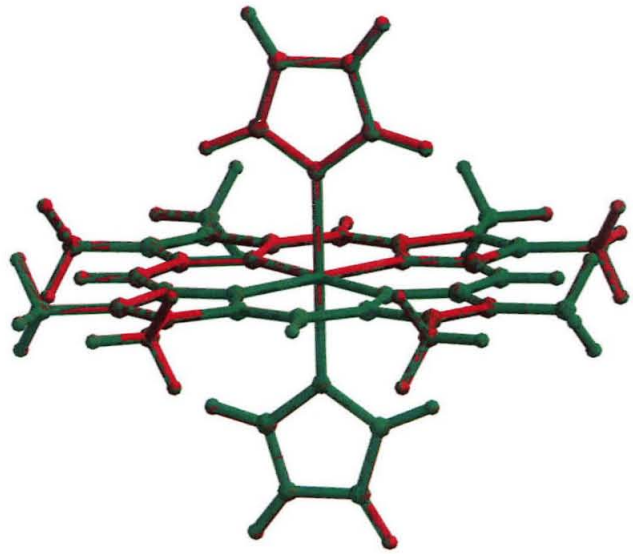

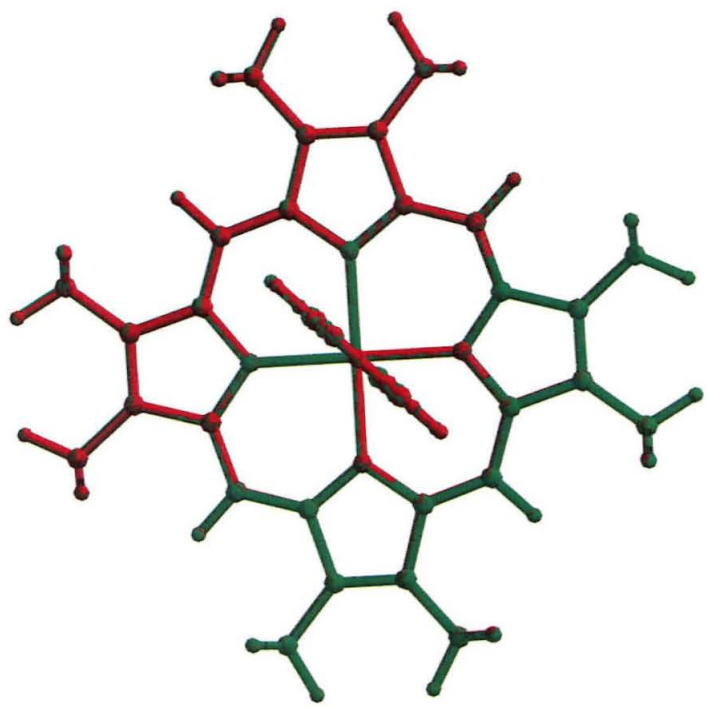

Figure 4.6. Overlay of B3LYP optimized geometries of reduced (green) and oxidized (red) forms of Co(imidazole)$_2$octamethylporphyrin, showing changes in bond lengths and angles, and the positions of methyl groups.

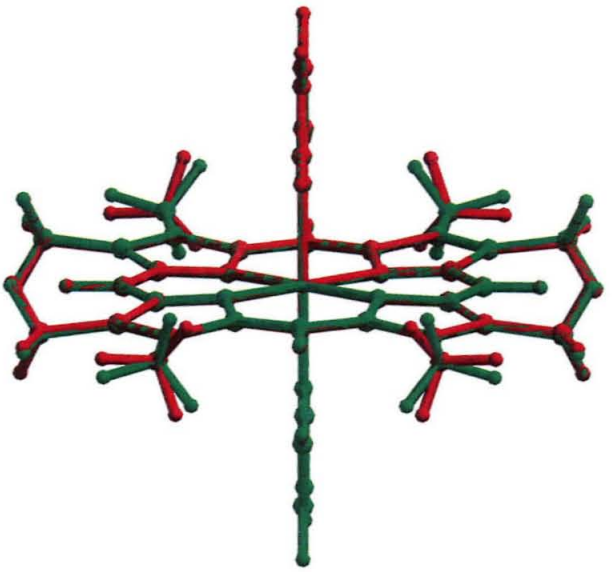

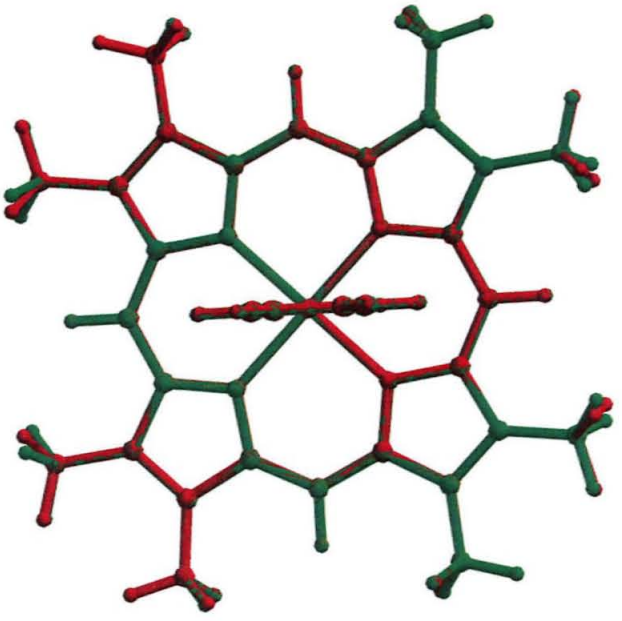

Figure 4.7. Four highest occupied molecular orbitals (where HOMO is the first orbital, HOMO-1 is the second orbital, *etc.*) of Fe(imidazole)$_2$octamethylporphyrin.

HOMO-2, Bu

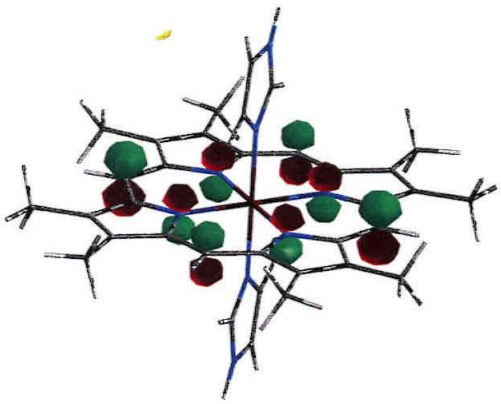

HOMO-3, Ag

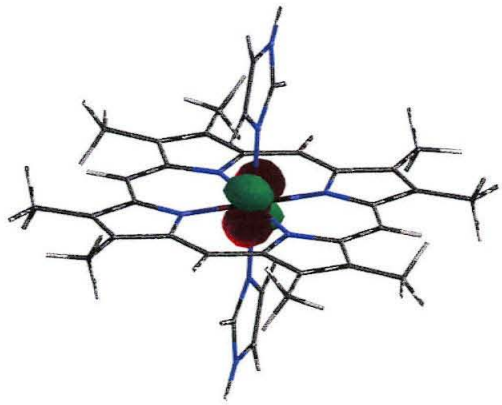

HOMO, Bg

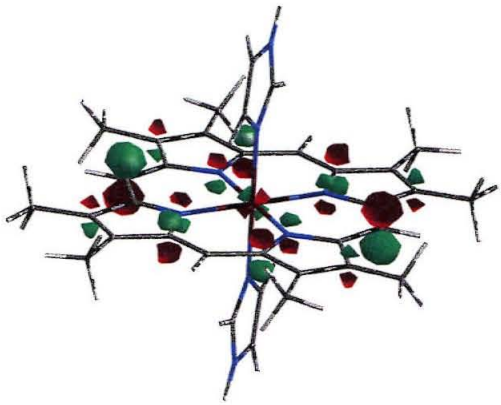

HOMO-1, Bg

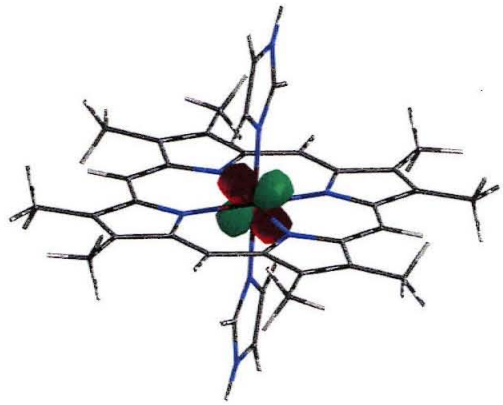

Figure 4.8. Fe(II)octamethylporphyrin molecular orbitals, where HOMO is the first highest occupied molecular orbital, HOMO-1 is the second highest occupied molecular orbital, *etc.*

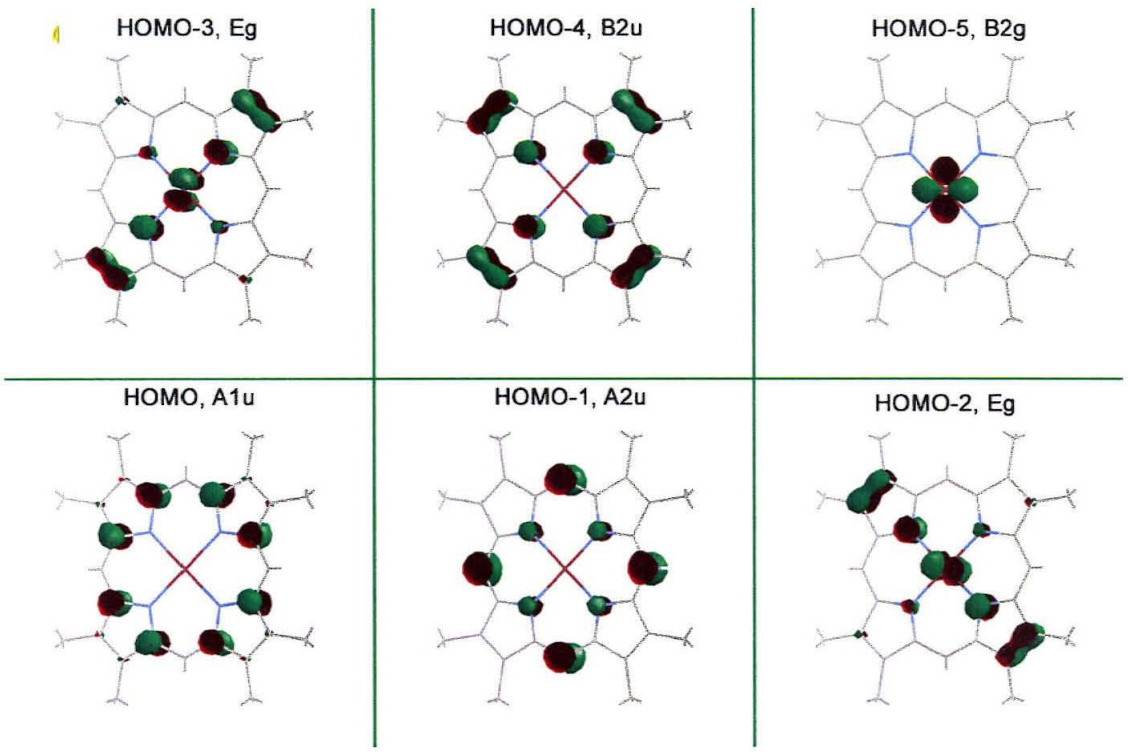
HOMO-3, Eg
HOMO-4, B2u
HOMO-5, B2g
HOMO, A1u
HOMO-1, A2u
HOMO-2, Eg

Table 4.3. Reorganization Energies (meV) of Metalloporphyrins

metal	ligands	λ^{red}	λ^{ox}	λ^{a}	λ^{b}
Fe	Im/Im	34	76	110	85
Fe	SH_2/SH_2	135	98	233	50
Fe	PhO^-/Im	-	-	$\leq 600^c$	487
Co	Im/Im	36	413	449	-

[a] $\lambda = \lambda^{red} + \lambda^{ox}$.

[b] Ref. 15.

[c] approximate value.

the reorganization is porphyrin-centered.[14] This observation is further confirmed by examination of nodal features of highest occupied molecular orbitals of the iron-*bis*(imidazole) complex (Figure 4.7). Unlike the a_{1u} HOMO of Fe(II)octamethylporphyrin (Figure 4.8), the first orbital, b_g, shows considerable metal character. Finally, our calculated reorganization energy is larger than λ obtained by Sigfridsson *et al.*[15] This may be due to the fact that in this work, octamethylporphyrin was used instead of porphin. As seen in Table 4.2, presence of peripheral functional groups affects the values of reorganization energy.

The other prototypical combination of axial ligands, Met-Met, is found in cytochromes b_1 and b_{557}.[12,16] Similar to the case of iron-*bis*(imidazole) complex, both Fe-S and Fe-N_{por} bond lengths change very little in the oxidized and reduced forms of iron-*bis*(SH_2) complex; thus, a similarly small reorganization energy is expected. The calculated λ value, however, is approximately two times greater than the one obtained for iron-*bis*(imidazole) complex. Moreover, λ^{red} is 135 meV, the largest value calculated so far for these iron model complexes with neutral ligands; the reasons behind this unexpected result are unclear. Nevertheless, the

Figure 4.9. Overlay of B3LYP optimized geometries of reduced (green) and oxidized (red) forms of $Fe(C_6H_5O)$(imidazole)octamethylporphyrin, showing major changes in bond lengths and angles.

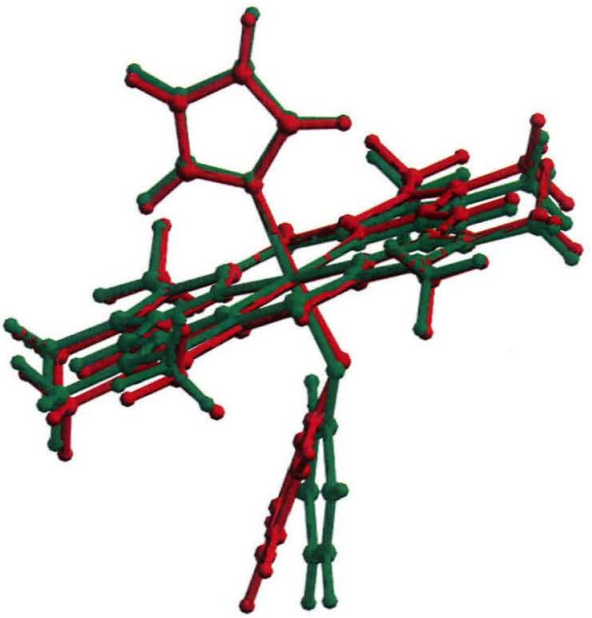

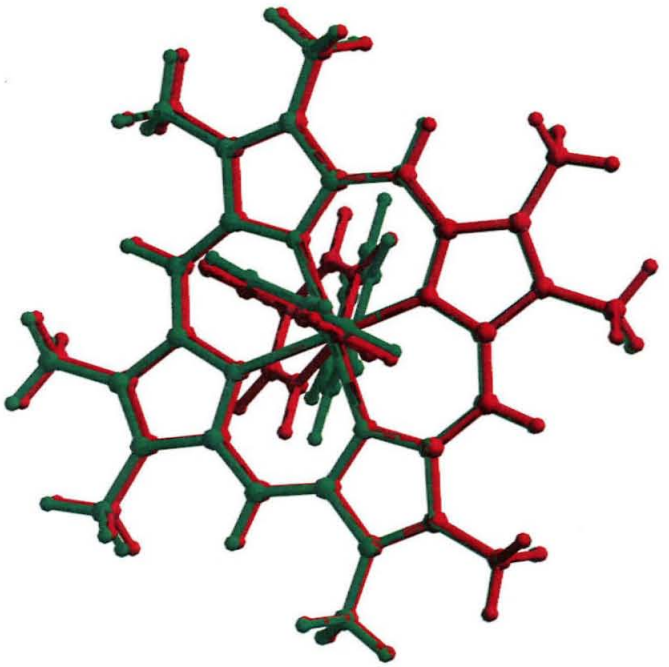

other calculated value of λ, 50 meV,[15] for iron-*bis*($S(CH3)_2$) porphyrin seems to be smaller than anticipated.

Finally, the last combination of axial ligands considered in this work is Tyr-His, which is found in the d_1 domain of cytochrome cd_1 nitrite reductase.[17] Phenoxy ion, $C_6H_5O^-$,was successfully used to model tyrosine. Due to the large size of the molecule, geometry optimization was carried out using a lower level of theory (i.e., polarized functions were not used), and reorganization energies were not calculated. The changes in geometry between reduced and oxidized forms of this complex are significant (Figure 4.9); therefore, the value of the reorganization energy is expected to be large. Indeed, Sigfridsson *et al.* performed calculation on a similar, but smaller system, obtaining value of $\lambda = 487$ meV.[15] Based on comparisons of calculations performed on the molecules with different porphyrin peripheral substituents, we speculate that the value of λ for our model iron-*bis*(phenoxy) complex will not exceed 600 meV. This large reorganization energy is primarily due to substantial changes in Fe-O bond length (0.20 Å). In nature, such large reorganization energy will hinder ET processes.[18] Indeed, the primary function of this six-coordinate heme is catalysis and not ET: the phenolate group dissociates from the heme upon substrate binding.[18]

Conclusion

In this work, we have calculated reorganization energies of metal porphyrins with different axial ligands. Neutral ligands, such as imidazole and SH_2, both yielded low

reorganization energies, which favor fast ET at low driving force. In fact, these combinations of ligands are the most common among electron-transfer proteins. On the other hand, a charged ligand, $C_6H_5O^-$, is expected to produce a larger reorganization energy. This may be part of the reason, why ligands, such as Tyr, are primarily found in catalytic sites. Finally, we have demonstrated that reorganization energies in low-valent metalloporphyrins are metal-centered, which is different from the case of high-valent iron hemes.

References

(1) Bendal, D. S. *Protein Electron Transfer;* BIOS Scientific: Oxford, **1996**.

(2) Palmer, G.; Reedijk, J. *Eur. J. Biochem.* **1991**, *200*, 599-611.

(3) Fraústo da Silvia, J. J. R.; Williams, R. P. J. *The Biological Chemistry of the Elements;* Clarendon Press: Oxford, **1994**.

(4) Marcus, R. A.; Sutin, N. *Biochim. Biophys. Acta* **1985**, *811*, 265-322.

(5) Miller, J. R.; Closs, G. L. *Science* **1988**, *240*, 440-447.

(6) Jaguar version 4.1, Schrödinger Inc.: Portland, OR, **1999**.

(7) Becke, A.D. *J. Chem. Phys.* **1993**, *98*, 5648-5652.

(8) Lee, C.; Yang, W.; Parr, R. G. *Phys. Rev.* **1988**, *B37*, 785-789.

(9) Mathews, F. S.; Czerwinski, E. W. *The Enzymes of Biological Membranes*; Plenum Press: New York, **1985**; Vol. 4.

(10) Scheidt, W. R. *Acc. Chem. Res.* **1977**, *10*, 339-345.

(11) Collins, D, M.; Countryman, R.; Hoard, J. L. *J. Am. Chem. Soc.* **1972**, *94*, 2066-2072.

(12) Frolow, F.; Kalb, A. J.; Yariv, J. *Nat. Struct. Biol.* **1994**, *1*, 453-460.

(13) Mashiko, T.; Marchon, J. -C.; Musser, D. T.; Reed, C. A.; Kastner, M. E.; Scheidt, W. R. *J. Am. Chem. Soc.* **1979**, *101*, 3653-3655.

(14) (a) Schulz, C. E.; Rutter, R.; Sage, P. G.; Debrunner, P. G.; Hager, L. P. *Biochem.* **1984**, *23*, 4743-4754. (b) Roberts, J. E.; Hoffman, B. M.; Rutter, R.; Hager, L. P. *J. Bio. Chem.* **1981**, *256*, 2118-2121. (c) Rutter, R.; Hager, L. P. *J. Bio. Chem.* **1982**, *257*, 7958-7961.

(15) Sigfridsson, E.; Olsson, M. H. M.; Ryde, U. *J. Phys. Chem.* **2001**, *105*, 5546-5552.

(16) (a) Cheeseman, M. R.; Thomson, A. J.; Greenwood, C.; Moore, G. R.; Kadir, F. *Nature* **1990**, *346*, 771-773. (b) George, G. N.; Richards, T.; Bare, R. E.; Gea, Y.; Prince, R. C.; Stiefel, E. I.; Watt, G. D. *J. Am. Chem. Soc.* **1993**, *115*, 7716-7718.

(17) Baker, S. C.; Saunders, N. F. W.; Willis, A. C.; Ferguson, S. J.; Hajdu, J.; Fülöp, V. *J. Mol. Biol.* **1997**, *269*, 440-455.

(18) Williams, P. A.; Fülöp, V.; Garman, E. F.; Saunders, N. F. W.; Ferguson, S. J.; Hajdu, J. *Nature* **1997**, *389*, 406-412.

Chapter 5

Density Functional Theory Calculation of Vibrational Frequencies of Organic Molecules

Acknowledgments:

Many thanks to Yunhee Yang for the helpful discussions.

Introduction

Density functional theory[1-4] (DFT) has been successful at calculating and assigning IR and Raman vibrational frequencies of complex molecules, such as polycyclic aromatic hydrocarbons (PAH) (e.g., phenanthrene and anthracene).[5-7] In addition, the assignment of vibrational progressions observed in optical[7] and photoelectron[8,9] spectra of these molecules has been recently aided by DFT calculations.[5] The focus of our research has been on measurement of gas-phase reorganization energies (λ), which requires accurate normal mode assignments of photoelectron spectra.[10] Unfortunately, little experimental and theoretical vibrational spectroscopy data for dibenzo[a,c]anthracene and dibenzo[a,c]phenazine are available. Given the success of DFT in obtaining vibrational frequencies of phenanthrene and anthracene,[5] this method has been employed to calculate and assign vibrational frequencies of molecules of interest to our research: phenazine, dibenzo[a,c]anthracene, and dibenzo[a,c]phenazine (see Chapter2, Scheme 2.1).

Methods

Geometry optimization and harmonic frequency calculations have been carried out using the Jaguar 3.5 program.[11] The B3LYP exchange-correlation functional has been used in all of the calculations. B3LYP consists of the hybrid exchange functional proposed by Becke[12] and the Lee-Yang-Parr[13] correlation functional. The former is a linear combination

of exact Hartree-Fock, Slater local-exchange functional and Becke's non-local gradient correction.[14] The correlation functional contains Vosko-Wilk-Nusair (VWN) local functional[15] and Lee-Yang-Parr local and nonlocal functionals.[13] The 6-31G (d,p) basis has been used throughout. It is a split-valence basis set with a set of d-type Gaussian polarization wavefunctions on nonhydrogen atoms and a set of p-type Gaussian polarization functions on the hydrogen atoms.

Results and Discussion

Scaling Factors

In order to calculate vibrational frequencies that favorably agree with experimental data, it is necessary to devise a simple procedure for scaling raw calculated values. Assuming that there is no strong Fermi resonance, this procedure allows to account for the anharmonicities and the imperfections of the method using few scaling factors.[5] Martin *et al.* (MEF) used the ratios of computed to experimental frequencies of naphthalene as the desired scaling factors and reported that they clustered into three groups: (1) an average ratio of 0.960 for the C-H stretches; (2) an estimated ratio of 0.983 for the in-plane bends; (3) and an average ratio of 0.970 for the remaining vibrations.[5] Upon basis set improvement (from cc-pVDZ to cc-pVTZ), the C-H stretching mode scaling factor became 0.965, and the distinction between the scaling factors for the in-plane and the remaining modes was no longer required (scaling factor of 0.975). These scaling factors (both from cc-pVDZ and cc-

pVTZ calculations) were then applied to the raw computed frequencies of benzene, anthracene, and phenanthrene, yielding remarkably good agreement with experimental data.[5]

In this work, phenanthrene and anthracene are used to determine scaling factors applied to the raw calculated harmonic frequencies of phenazine, dibenzo[a,c]anthracene, and dibenzo[a,c]phenazine. A considerable amount of experimental and theoretical data on phenanthrene and anthracene vibrational spectra have been published. In the case of phenanthrene, Bree, Solven, and Vilkos (BSV) have reported single-crystal polarized infrared and Raman vibrational spectra.[16] Canè *et al.* obtained a gas-phase infrared spectrum,[17] and Warren and coworkers recorded the dispersed fluorescence spectrum in a supersonic expansion.[18] Cyvin *et al.* used five-parameter force-field approximation to assign the vibrational spectrum of phenanthrene;[19] Rougeau *et al.* employed scaled quantum mechanical (SQM) force-field based on modified neglect of diatomic overlap (MNDO) method to determine harmonic frequencies.[20] Finally, MEF performed B3LYP/cc-pVDZ calculations.[5]

In the case of anthracene, IR and Raman spectra of crystalline films and polyethylene-matrix-bound molecules are available from the works of Bakke *et al.*[21] and Neerland *et al.*[22] Szczepanski and coworkers reported vibrational spectrum of anthracene molecules isolated in an argon matrix and calculated the HF/3-21G ground-state frequencies.[23] Anthracene vibrational frequencies were computed by Rougeau *et al.* employing SQM method based on MNDO force-constant matrices and scaling factors,[20] while MEF performed B3LYP/cc-pVDZ calculations.[5] The comparison between HF/3-21G and B3LYP/cc-pVDZ calculation results is discussed in detail elsewhere.[5]

In this work, phenanthrene and anthracene vibrational frequencies were calculated

using B3LYP/6-31G(d,p) method. Computed frequencies were compared to the experimental values reported by BSV in the case of phenanthrene,[16] and both Bakke *et al.* and Neerland *et al.* in the case of anthracene.[21, 22] The average ratios between the experimental and calculated frequencies were separated into four categories: (1) low-frequency in-plane modes that involve C-C bond stretching and bending produced a 0.987 scaling factor; (2) in-plane modes that are combinations of C-C and C-H vibrational and bending modes gave an average ratio of 0.973; (3) high-frequency C-H stretching modes yielded an average ratio of 0.956; (4) out-of-plane vibrational modes for which a 0.984 scaling factor was obtained. The scaling factors reported by MEF differ by less than 1% from those calculated here, demonstrating that the B3LYP/6-31G(d,p) and B3LYP/cc-pVDZ methods similar. High-frequency C-H stretching modes exhibit significant anharmonic effects in comparison to other vibrational modes; consequently, the magnitude of scaling factor for these modes is lower.

Phenanthrene

B3LYP/6-31G(d,p) raw and scaled harmonic frequencies of phenanthrene are reported in Table 5.1 along with experimental frequencies,[16-18] B3LYP/cc-pVDZ,[5] and SQM/MNDO[20] results. In the A_1 symmetry block, the scaled frequencies computed with different basis sets agree within 0–13 cm^{-1}, and no mismatches between experimental and B3LYP/6-31G(d,p) harmonic frequencies are apparent. In contrast, the simple five-parameter force-field calculation of Cyvin *et al.* largely fails to reproduce the experimentally observed bands.[19] The SQM/MNDO results appear to yield better agreement with the experiment,[20] but are

inferior to the DFT frequencies.

In the B_2 symmetry block, no significant differences are found between scaled harmonic frequencies calculated with the 6-31G(d,p) and cc-pVDZ basis sets. B3LYP/6-31G(d,p) frequency, 499 cm^{-1}, for $21b_2$ mode agrees favorably with the experimental results from refs. 17 and 18. B3LYP/6-31G(d,p) $18b_2$ and $17b_2$ harmonic frequencies are 16 cm^{-1} higher than those reported by MEF, but only 5cm^{-1} and 6 cm^{-1} higher than the experimental values.[16,17]

MEF suggested that the 1148 cm^{-1} band reported in ref. 24 was assigned incorrectly. B3LYP/6-31G(d,p) frequency, 1160 cm^{-1}, is only 13 cm^{-1} below the experimental value reported by BSV.[16] Moreover, recently reported gas-phase infrared band at 1163 cm^{-1} assigned to $14b_2$[17] is in a perfect agreement with our calculated frequency and only 10 cm^{-1} lower that of BSV.[16] Thus, we confirm BSV assignment for this mode.[16] Finally, as observed in the A_1 symmetry block, the five-parameter force-field[19] and the SQM/MNDO[20] methods are inferior to B3LYP/6-31G(d,p) level of theory.

In the A_2 symmetry block, there are no significant differences between B3LYP/6-31G(d,p) harmonic frequencies and the values reported by MEF. SQM/MNDO frequencies are 9–39 cm^{-1} different from the scaled results and largely fail to reproduce experimental values. The frequencies calculated by Cyvin *et al.*[19] agree well with the B3LYP/6-31G(d,p) scaled results with the exception of $9a_2$ and $8a_2$. In our calculation, the scaled harmonic frequency for $9a_2$ is 399 cm^{-1}, confirming assignment of BSV.[16] The B3LYP/6-31G(d,p) frequency, 536 cm^{-1}, for the $8a_2$ is 51 cm^{-1} higher than the one reported by Cyvin *et al.*[19]

Table 5.1: Phenanthrene Frequencies (cm^{-1}) and Calculated IR Intensities (in Parentheses)

	B3LYP/6-31G(d,p)[a]			experiment			calculated		comments
v	**raw**	**SF[b]**	**scaled**	**Ref. 16**	**Ref. 17**	**Ref. 18**	**B3LYP/cc-pVDZ[c]**	**SQM /MNDO[d]**	
						A_1			
23	245 (0.18)	1	242	247		246	244	247	
22	410 (0.32)	1	405	408	398	408	401	402	
21	556 (0.32)	1	549	548		544	546	543	
20	724 (0.05)	1	714	711		714	706	744	
19	844 (0.07)	1	833	832		833	827	812	
18	1066 (0.80)	2	1038	1038		1043	1033	1072	
17	1119 (0.86)	2	1089	1094	1094	1065	1085	1106	
16	1181 (0.22)	2	1150	1144			1145	1123	
15	1191 (0.01)	2	1159	1163?[e]		1165	1150	1183	
14	1240 (1)	2	1206	1203	1200	1199	1192	1205	
13	1271 (8.43)	2	1237	1247	1244	1257	1230	1279	
12	1334 (0.72)	2	1298	1304	1299		1294	1290	
11	1394 (1.24)	2	1356	1352	1340	1355	1355	1338	
10	1465 (1.23)	2	1426	1431	1431	1423	1419	1429	
9	1481 (0.84)	2	1441	1443	1446	1450	1436	1463	
8	1574(1.20)	2	1532	1526	1530	1526	1520	1536	
7	1660 (3.47)	2	1616	1602	1608	1580	1602	1605	
6	1678 (0.45)	2	1633	1626		1613	1621	1629	
5	3178 (7.43)	3	3040	3002?[e]			3040	3073	
4	3187 (11.85)	3	3049	3037	3032		3052	3076	
3	3195 (38.53)	3	3056	3057			3057	3080	
2	3203 (0.98)	3	3063	3072	3082		3067	3084	
1	3220 (30.29)	3	3080	3082?[e]	3102		3085	3092	

Table 5.1 is continued on the next page.

Table 5.1. (*continued*)

	B3LYP/6-31G(d,p)[a]			experiment			calculated		comments
v	raw	SF[b]	scaled	Ref. 16	Ref. 17	Ref. 18	B3LYP/cc-pVDZ[c]	SQM /MNDO[d]	
						B_2			
22	447 (2.17)	1	441	441	431	471	438	437	
21	506 (0.64)	1	499	536	502	500	495	498	536 is incorrect
20	630 (5.31)	1	622	619	618	620	618	600	
19	726 (2.60)	1	717	712	709	731	708	695	
18	892 (1.64)	1	881	876	876	875	865	862	
17	1020 (0.72)	2	1007	1001	1002		991	1020	
16	1067 (3.70)	2	1038	1040	1040	1019	1036	1095	
15	1169 (0.97)	2	1138	1144	1142		1131	1158	
14	1192 (0.39)	2	1160	1173?[e]	1163		1149	1165	1173 cm-1, 1148[f] are possible
13	1249 (0.90)	2	1216	1227	1236		1208	1219	
12	1308 (0.01)	2	1273	1282	1270		1263	1266	
11	1396 (0.25)	2	1359	1340?[e]	1358		1355	1284	
10	1450 (0.04)	2	1411			1436	1404	1381	
9	1499 (14.65)	2	1459	1458	1458		1451	1436	
8	1548 (6.96)	2	1506	1502	1504		1502	1505	
7	1624 (0.04)	2	1580	1572			1580	1571	
6	1672 (0.51)	2	1628	1616			1616	1613	
5	3174 (0.95)	3	3036	3019	3015		3037	3068	
4	3178 (3.26)	3	3040				3041	3073	
3	3187 (0.37)	3	3048	3047	3061		3051	3075	
2	3202 (43.72)	3	3063	3064	3068		3065	3083	
1	3211 (22.96)	3	3071	3094			3075	3091	

Table 5.1 is continued on the next page.

Table 5.1. *(continued)*

	B3LYP/6-31G(d,p)[a]			experiment			calculated		comments
v	raw	SF[b]	scaled	Ref. 16	Ref. 17	Ref. 18	B3LYP/cc-pVDZ[c]	SQM /MNDO[d]	
						A_2			
11	112	4	110				97	78	
10	251	4	248				239	238	
9	405	4	399	395?[e]			392	384	395 is correct
8	545	4	537				537	562	
7	595	4	586	594			585	599	
6	778	4	766	761			754	785	
5	807	4	794	763			799	821	
4	886	4	872	791			885	911	
3	968	4	953	946			933	943	
2	991	4	976	969			960	954	972 is possible
1	1002	4	987	1159?[e]			973	1011	1159 is incorrect
						B_1			
10	116 (0.57)	4	115	124			99	94	
9	237 (2.23)	4	233	234	225		226	229	
8	442 (3.61)	4	435	426	424		428	453	
7	507 (2.70)	4	499	495	494		500	520	
6	725 (2.23)	4	714	715			716	731	
5	766 (54.38)	4	754	732	732		733	764	
4	842 (41.25)	4	829	817	810		814	835	
3	893 (7.76)	4	879	871	863		867	904	
2	977 (3.22)	4	962	950	948		941	935	
1	1003 (0)	4	988	1149			974	973	1149 is incorrect

[a] this work; [b] Scaling factors: 1 = 0.987, 2 = 0.973, 3 = 0.956, 4 = 0.984; [c] Ref. 5; [d] Ref. 20; [e] ?: questionable assignment; [f] Ref. 24.

There are no experimental data available for this mode. BSV assigns the 969 cm^{-1} band to $2a_2$.[16] The low-intensity Raman band observed at 972 cm^{-1},[16] however, is in a better agreement with our $2a_2$ calculated frequency. BSV tentatively assigned the1159 cm^{-1} band to $1a_2$,[16] disagreeing with both B3LYP/6-31G(d,p) (987 cm^{-1}) and B3LYP/cc-pVDZ[5] (973 cm^{-1}) results. Witt and Mecke report a $1a_2$ band at 944 cm^{-1},[25] while Schettino *et al.* assign the 928 cm^{-1} band to $1a_2$,[24] again yielding large discrepancy between experimental and calculated frequencies. There are no reports of other experimental Raman bands that would support DFT calculations. MEF suggested that the $1a_2$ experimental frequency corresponds to a low-intensity transition, and it is most likely not observed. The Raman intensities for the A_2 symmetry block have to be calculated in order to make a firm assignment for this mode.

In the B_1 symmetry block, scaled B3LYP/6-31G(d,p) frequencies confirm the experimental assignment of BSV and Canè *et al.*[16, 17] B3LYP/6-31G(d,p) $10b_1$ scaled frequency is 26 cm^{-1} higher than the one reported by MEF.[5] The experimental frequency,[16] however, is only 9cm^{-1} higher than the scaled B3LYP/6-31G(d,p) value. Our $5b_1$ calculated result is 21 cm^{-1} higher than MEF's frequency,[5] which is in a perfect agreement with experimental value. This is the first example, where the B3LYP/6-31G(d,p) scaled frequency does not accurately reproduce experimental value. BSV assigned the 1149 cm^{-1} band to $1b_1$,[16] disagreeing with both MEF and our computed frequencies. We calculate zero infrared intensity for this mode; thus, it is probably not experimentally observed.

In summary, the simple scaling procedure has successfully reproduced experimental frequencies (Table 5.1). The largest deviations were found in the case of high-frequency C-H

modes, such as $1b_2$, where the computed frequency is 23 cm^{-1} lower than the experimental value.[16] This shows that anharmonic effects are significant and can only be partially accounted for by the simple scaling procedure. $5b_1$ is the only example of a low-frequency mode, for which our scaled frequency is 20 cm^{-1} different from the experiment.

Anthracene

B3LYP/6-31G(d,p) results and experimental frequencies[21-23] for anthracene are reported in Table 5.2 along with the SQM/MNDO calculations.[20] In the A_g symmetry block, the experimental results[21,22] accord well with B3LYP/6-31G(d,p) harmonic frequencies. There are no significant differences between the scaled frequencies calculated with different basis sets with an exception of $5a_g$: MEF result is 18 cm^{-1} lower than the scaled B3LYP/6-31G(d,p) frequency. The experimental value,[21,22] however, is only 9 cm^{-1} lower than our result and 9 cm^{-1} higher than MEF calculation. Despite anharmonic effects, B3LYP/6-31G(d,p) scaled frequencies for the $3a_g$, $2a_g$, and $1a_g$ modes are in good agreement with the experimental values.[21,22]

In the B_{3g} symmetry block, no significant differences between the B3LYP/6-31G(d,p) and B3LYP/cc-pVDZ scaled frequencies are observed. MEF reported that Bakke *et al.* and Neerland *et al.* incorrectly assigned the 1433 cm^{-1} band to $5b_{3g}$.[21, 22] We also find that the 1376 cm^{-1} band[26] agrees with our calculated value for $5b_{3g}$ best.

Both Bakke *et al.* and Neerland *et al.* assign the 397 cm^{-1} band to $12a_g$ and $11b_{3g}$.[21, 22] Bolotnikova reported a fluorescence band at 390 cm^{-1}, assigning it to$12a_g$.[27] The B3LYP/6-31G(d,p) scaled frequency for $12a_g$ is 399 cm^{-1} and that for $11b_{3g}$ is 387cm^{-1}. If we were to

base our assignment solely on the magnitude of the calculated harmonic frequency, then the fluorescence band at 390 cm^{-1} would be assigned to $11b_{3g}$ and not to $12a_g$. This is contrary to the MEF assignment, associating the 390 cm^{-1} band with $12a_g$ and the 397 cm^{-1} experimental frequency[21,22] with $11b_{3g}$. The difference between experimental[21,22,27] and calculated (ref. 5 and this work) results, however, is small and it is difficult to make a firm assignment without calculating Raman intensities for these bands. Our and MEF scaled frequencies for $2b_{3g}$ are in a poor agreement with the experimental value.[21,22] We attribute this to the significant anharmonic distortions of this mode.

In the B_{1u} symmetry block, the assignments given by Bakke *et al.* and Neerland *et al.* accord well with scaled B3LYP/6-31G(d,p) frequencies.[21, 22] Scaled harmonic frequencies calculated with different basis sets do not differ significantly with an exception of $5b_{1u}$. However, the experimental values assigned to $5b_{1u}$ are only 8 cm^{-1} lower than our calculated harmonic frequencies and 7 cm^{-1} higher that of MEF.[21-23] Experimental $4b_{1u}$ bands[21-23] are in the better agreement with MEF calculation than with our scaled harmonic frequency.[5] The 1627 cm^{-1} band,[23] however, is only 12 cm^{-1} lower than B3LYP/6-31G(d,p) result. The high-frequency C-H stretching modes reported in ref. 23 agree well with the DFT harmonic frequencies.

The B_{2u} symmetry block calculated frequencies largely agree with those reported by MEF. Unlike the case with A_g, B_{3g}, and B_{1u} symmetry blocks, our calculation does not fully confirm Bakke *et al.* and Neerland *et al.* assignments of the vibrational spectrum.[21,22] We believe, however, that the assignment of the 809 cm^{-1} band to $10b_{2u}$ is correct.[21,22]

The B3LYP/6-31G(d,p) frequency for $8b_{2u}$ is 1142 cm^{-1},which is 24 cm^{-1} higher than

Table 5.2. Anthracene Frequencies (cm^{-1}) and Calculated IR Intensities (in Parentheses)

	B3LYP/6-31G(d,p) [a]			experiment		calculated		comments
v	**raw**	**SF[b]**	**scaled**	**Refs. 21 and 22**	**Ref. 23**	**B3LYP/cc-pVDZ [c]**	**SQM/ MNDO[d]**	
						A_g		
12	404	1	399	397		391	388	390,[e] 397 are possible
11	638	1	629	625		627	617	
10	763	1	753	754		742	809	
9	1036	2	1009	1007		1003	1079	
8	1191	2	1159	1164		1157	1186	
7	1301	2	1266	1264		1272	1321	
6	1447	2	1408	1412		1402	1433	
5	1530	2	1489	1480		1471	1492	
4	1607	2	1564	1556		1556	1562	
3	3174	3	3036	3027		3037	3069	
2	3182	3	3044	3048		3045	3074	
1	3205	3	3065	3072		3069	3090	
						B_{3g}		
11	392	1	387	397		388	401	390,[e] 397 are possible
10	539	1	532	521		524	522	
9	928	1	916	903		908	856	
8	1132	2	1101	1102		1106	1124	
7	1216	2	1184	1187		1180	1214	
6	1300	2	1265	1273		1260	1303	
5	1421	2	1383	1433		1380	1345	1433 is incorrect; 1376[f] is correct
4	1636	2	1593	1574		1582	1599	
3	1684	2	1639	1632		1629	1639	
2	3177	3	3038	3017		3039	3072	
1	3193	3	3054	3054		3058	3083	

Table 5.2 is continued on the next page.

Table 5.2. (*continued*)

	B3LYP/6-31G(d,p) [a]			experiment		calculated		comments
v	**raw**	**SF[b]**	**scaled**	**Refs. 21 and 22**	**Ref. 23**	**B3LYP/cc-pVDZ [c]**	**SQM/ MNDO[d]**	
						B_{1u}		
11	238 (0.88)	1	235	234		231	241	
10	664 (0.96)	1	655	653	652	648	631	
9	917 (1.15)	1	905	906	908	897	847	
8	1177 (4.43)	2	1145	1147	1149, 1151	1145	1152	
7	1295 (4.93)	2	1260	1272	1272	1259	1264	
6	1345 (2.86)	2	1309	1317	1346	1297	1302	
5	1496 (0.67)	2	1456	1448	1450	1441	1463	
4	1684 (5.46)	2	1639	1620	1627	1629		
3	3172 (22.97)	3	3034	3007	3022, 3017	3036		
2	3175 (5.43)	3	3037	3053	3032	3040		
1	3194 (74.55)	3	3055	3084	3062, 3055	3058		

Table 5.2 is continued on the next page.

Table 5.2. *(continued)*

	B3LYP/6-31G(d,p) [a]			experiment		calculated		comments
v	raw	SF[b]	scaled	Refs. 21 and 22	Ref. 23	B3LYP/cc-pVDZ [c]	SQM/ MNDO[d]	
					B_{2u}			
11	620 (8.64)	1	612	601	603	604	580	
10	821 (0.03)	1	811	809		800	884	809 is correct
9	1036 (4.93)	2	1008	998	1001	999	1036	
8	1174 (0.23)	2	1142	1124		1120	1078	
7	1196 (3.24)	2	1164	1167	1167, 1169	1162	1180	
6	1400 (3.09)	2	1363	1397	1318	1362	1237	1397 is incorrect
5	1431 (0.81)	2	1393	1495	1400	1403	1413	1495 is incorrect; 1397 is correct
4	1494 (2.42)	2	1454	1534	1460	1433	1448	1534 is incorrect
3	1594 (5.45)	2	1551	1690	1542, 1540	1539	1553	1690 is incorrect: 1534 is correct
2	3181 (1.30)	3	3044	3021		3044	3074	3048[g] is better
1	3204 (71.70)	3	3064	3048	3068, 3067	3069	3090	3079[g] is better

Table 5.2 is continued on the next page.

Table 5.2. (*continued*)

	B3LYP/6-31G(d,p) [a]			experiment		calculated		comments
v	raw	SF[b]	scaled	Refs. 21 and 22	Ref. 23	B3LYP/cc-pVDZ [c]	SQM/ MNDO[d]	
						B_{1g}		
4	242	4	239	244		232	238	
3	489	4	482	479		476	517	
2	787	4	775	760		755	790	
1	982	4	967	956		947	935	
						B_{2g}		
6	274	4	270	287		265	249	
5	585	4	575	580		576	552	
4	778	4	766	773		772	781	
3	862	4	848	896		832		questionable assignment
2	920	4	905	916		904	952	
1	1003	4	988	977		975	1009	
						A_u		
5	133	4	131			119	108	
4	505	4	497			497	510	
3	754	4	742	743		751	783	
2	879	4	866	858		825	905	858 is correct
1	1002	4	987	988		974	977	

Table 5.2 is continued on the next page.

Table 5.2. (*continued*)

	B3LYP/6-31G(d,p) [a]			experiment		calculated		comments
v	raw	SF[b]	scaled	Refs. 21 and 22	Ref. 23	B3LYP/cc-pVDZ [c]	SQM/MNDO[d]	
						B_{3u}		
6	106 (0.94)	4	105	106		90	95	
5	386 (0.03)	4	380	380		378	356	
4	482 (14.00)	4	474	474	470, 468	470	518	
3	763 (69.34)	4	751	737	729, 726	727	759	
2	912 (51.87)	4	898	883	878.5	881	896	
1	987 (6.95)	4	971	956	955, 958	952	950	

[a] this work; [b] Scaling factors: 1 = 0.987, 2 = 0.973, 3 = 0.956, 4 = 0.984; [c] Ref. 5; [d] Ref. 20; [e] Ref.27; [f] Ref. 26; [g] Ref. 28.

the one reported by MEF. The experimental value[21,22] assigned to this mode is 1124 cm^{-1}, which agrees favorably with MEF B3LYP/cc-pVDZ frequency.[5] Both calculated frequencies for $6b_{2u}$ are in serious disagreement with Bakke *et al.* and Neerland *et al.* assignments.[21, 22] We agree with MEF that 1397 cm^{-1} band is incorrectly assigned to $6b_{2u}$.[5,21,22]

Our calculation result for $5b_{2u}$ agrees well with Szczepanski *et al.* frequency;[23] but there is a serious discrepancy with Bakke *et al.* and Neerland *et al.* assignments.[21, 22] We confirm MEF suggestion that the 1397 cm^{-1} band[21,22] is $5b_{2u}$. The calculated frequency for $4b_{2u}$ with the 6-31G(d,p) basis is 21 cm^{-1} higher than the cc-pVDZ result.[5] Despite this difference, neither calculation confirms Bakke *et al.* and Neerland *et al.* assignment of the 1534cm^{-1} band to $4b_{2u}$.[21, 22] Szczepanski *et al.* report the $4b_{2u}$ band,[23] which accords well with B3LYP/6-31G(d,p) frequency. Our calculated harmonic frequency for $3b_{2u}$ is 12 cm^{-1} higher than the MEF result.[5] Neither calculation, however, confirms the experimental assignment of the 1690 cm^{-1} band[21,22] to $3b_{2u}$. We agree with MEF suggestion that the 1534cm^{-1} band belongs to $3b_{2u}$. The experimental values for the high-frequency C-H stretching modes reported by Bakke *et al.* and Neerland *et al.* are the most 23 cm^{-1} lower than our calculation results.[21,22] Neto *et al.* reported the 3079 cm^{-1} and 3048 cm^{-1} bands[28] that agree well with our calculated frequencies for $1b_{2u}$ and $2b_{2u}$. Also, 3068 cm^{-1} and 3067 cm^{-1} bands from ref. 23 accord well with the our calculated frequency, 3064 cm^{-1}, for $1b_{2u}$.

In the B_{1g} symmetry block, our calculated frequencies for $1b_{1g}$ and $2b_{1g}$ are 20 cm^{-1} higher than the MEF results.[5] The experimental frequencies,[21,22] however, are the most 15 cm^{-1} lower than the B3LYP/6-31G(d,p) values.

Unlike B_{1g}, in the B_{2g} symmetry block, frequencies calculated using two different basis

sets are in good agreement. Our calculation results confirm Bakke *et al.* and Neerland *et al.* assignment with an exception of $3b_{2g}$.[21,22] Räsänen *et al.* reported the 896 cm^{-1} band,[26] which Neerland *et al.* assigned to $3b_{2g}$ based on the results of the five-parameter force-field calculation (see ref. 22 for detail). Bakke *et al.*, however, do not observe this Raman band in their spectrum,[21] suggesting that the feature at 896 cm^{-1} is a low-intensity vibration. Therefore, we propose that the band predicted by our calculation is not observed due to its low intensity. In order to test this proposal, we have to calculate this Raman intensity. MEF suggested that the 824 cm^{-1} band observed by Szczepanski *et al.* should be assigned to $3b_{2g}$.[23] B_{2g} modes, however, are infrared inactive and therefore MEF assignment is questionable.

Our calculated frequencies for the A_u block are in good agreement with MEF results with an exception of $2a_u$. MEF frequency for this mode is 41 cm^{-1} lower than the B3LYP/6-31G(d,p) result. Bakke *et al.* and Neerland *et al.* assign the 858 cm^{-1} band to $2a_u$,[21,22] which is only 8 cm^{-1} lower than our calculated frequency; thus in contrast to MEF suggestion,[5] we support Bakke *et al.* and Neerland *et al.* assignment.[21, 22]

In the B_{3u} symmetry block, our calculated frequencies for $6b_{3u}$, $5b_{3u}$ and $4b_{3u}$ are in good agreement with the experimental results. Our calculation result for $3b_{3u}$ is 24 cm^{-1} higher than the MEF's frequency. The experimental value, 737 cm^{-1},[21,22] however, is only 14 cm^{-1} lower than the B3LYP/6-31G(d,p) frequency. Unlike MEF scaled frequencies, our $2b_{3u}$ and $1b_{3u}$ calculation results are 15 cm^{-1} higher than the experimentally observed bands.[21,22]

In summary, our B3LYP/6-31G(d,p) scaled frequencies have largely reproduced the experimental values (Table 5.2). Only few discrepancies between frequencies calculated

with 6-31G(d,p) and cc-pVDZ basis sets are apparent.

Phenazine

Durnick and Wait (DW) reported phenazine IR (using KBr pellet and Nujol mull samples) and Raman spectra.[29] Neto *et al.* recorded a single-crystal IR spectrum,[30] and Radziszewski *et al.* measured mid- and far-IR spectra of phenazine in polyethylene film.[31] Mitchell *et al.* reported the matrix-isolated triplet-state (T_1) IR spectrum of phenazine.[32] In these publications, the assignment of phenazine spectra was primarily based on the polarized Raman and IR results, experimental intensities, isotope shifts in vibrational spectra of deuterated phenazine, direct comparison with anthracene spectra, and simple force-field calculations (see ref. 29 for details). To our knowledge, there are no reports of DFT vibrational frequency calculations of phenazine.

The scaling factors derived from the vibrational spectra of anthracene and phenanthrene were applied to the raw B3LYP/6-31G(d,p) frequencies. In order to investigate the consequences of using the same scaling factors (based solely on the C-C, and C-H vibrational modes) to the harmonic vibrational frequencies of aromatic heterocycles, we calculated the harmonic frequencies of ^{15}N isotope-substituted phenazine. Phenazine B3LYP/6-31G(d,p) and experimental values are listed in Table 5.3. The frequencies from the force-field calculations are also listed in Table 5.3 along with the B3LYP/6-31G(d,p) scaled harmonic frequencies for ^{15}N isotope substituted phenazine.

In the A_g symmetry block, the scaled harmonic frequencies are in good agreement with DW assignment.[29] Only the $11a_g$, $10a_g$, and $9a_g$ modes of phenazine showed appreciable

isotope shifts in our calculation. The experimental values[29] for these modes are, however, in the perfect agreement with B3LYP/6-31G(d.p) frequencies scaled by the factor 0.987, demonstrating that nitrogen substitution into the carbon positions in the molecule has no effect on the calculated frequencies for these modes. In the case of $8a_g$, the B3LYP/6-31G(d,p) scaled result is 15 cm^{-1} lower than the experimental frequency.[29] We agree with DW assignment, however, because the 1013 cm^{-1} band is a high-intensity polarized Raman band.[29] Also, the experimental $9a_g$ frequency of anthracene[21,22] and $8a_g$ phenazine frequency are in remarkable agreement. B3LYP/3-61G(d,p) $1a_g$ and $2a_g$ frequencies are only 13 cm^{-1} and 6 cm^{-1} respectively higher than the experimental values,[29] which is exceptional, considering that these are high-frequency C-H stretching modes.

In the B_{3g} symmetry block, the experimental frequencies[29] accord well with our calculated results, except for $9b_{3g}$, $8b_{3g}$, $5b_{3g}$. DW assigned the 525 cm^{-1} band to $9b_{3g}$ based on the force-field calculation result[29] and the corresponding anthracene $10b_{3g}$ vibrational frequency, 521 cm^{-1}.[21,22] We calculated a 41 cm^{-1} isotope shift for the $9b_{3g}$ scaled harmonic frequency. The significant nitrogen-for-carbon substitution effect on $9b_{3g}$ precludes the use of the 0.987 scaling factor. The observed ratio between the experimental,[29] 525 cm^{-1}, and the calculated, 566 cm^{-1}, values is 0.92.

The $8b_{3g}$ calculated frequency also shows an isotope shift, in this case by 6 cm^{-1} from 926 cm^{-1}; this, however, does not justify the fact that the calculated frequency is 55 cm^{-1} higher than the experimental value. In anthracene vibrational spectrum, a similar band is found at 903 cm^{-1},[21, 22] which is 34 cm^{-1} higher than the corresponding experimental phenazine frequency,[29] while anthracene's calculated $9b_{3g}$ frequency is only 10 cm^{-1} lower

than phenazine's calculation result. This indicates that there should be only a similarly small difference between the experimental results for these molecules. Based on these observations, DW assignment is questionable.[29] A calculation of Raman intensities is needed for sound assignment of this mode.

DW assignment of the 1348 cm^{-1} band to $5b_{3g}$[29] is in poor agreement with the scaled B3LYP/6-31G(d,p) frequency. The calculated isotope shift of 4 cm^{-1} from 1383 cm^{-1} is insignificant. DW report a band at 1374 cm^{-1},[29] which is a better fit to our calculated frequency; moreover, the $5b_{3g}$ experimental frequency of anthracene,[21,22] 1376 cm^{-1}, matches our calculation for phenazine. Based on these observations, we conclude that the 1374 cm^{-1} band should be assigned $5b_{3g}$.

B3LYP/6-31G(d,p) frequencies in B_{1u} and B_{2u} symmetry blocks largely confirm the DW assignment.[29] The 1636 cm^{-1} band reported by Neto *et al.*[30] is in a better agreement with our $3b_{1u}$ calculated frequency. The B3LYP/6-31G(d,p) frequency for $2b_{1u}$ is 34 cm^{-1} higher than the experimental value from ref. 29, due to large anharmonic effects in this mode. The experimental frequency, 3069 cm^{-1},[30] is in a better agreement with the $1b_{1u}$ calculated result than other experimental values.[29,31]

DW assigned the 1209 cm^{-1} band to $6b_{2u}$ which is 25 cm^{-1} lower than our calculated frequency. For this mode, we calculate a 13 cm^{-1} isotope shift below 1234 cm^{-1}. Therefore, one possible explanation for the observed difference between the scaled frequency and the experimental value[29] is the significant nitrogen character in $6b_{2u}$. Alternatively, there is a low-intensity band observed at 1234 cm^{-1},[29] which is in a perfect agreement with our calculation. Since the isotope shift is relatively small, we tentatively assign 1234 cm^{-1} band

to $6b_{2u}$.

Calculated B_{1g} and B_{2g} frequencies are in good agreement with the experimental values.[29] DW assignment of 963 cm^{-1} band to $1b_{1g}$ is based on the force-field calculations.[29] In anthracene vibrational spectra, the 956 cm^{-1} band is assigned to $1b_{1g}$,[21,22] which also confirms DW experimental assignment for phenazine. Anthracene experimental frequency for $1b_{1g}$ band is 11 cm^{-1} lower than the B3LYP/6-31G(d,p) result (see Table 5.2); and in the case of phenazine the difference between experimental and calculation frequencies is 17 cm^{-1}. Despite these discrepancies, the DFT calculation is superior at reproducing experimental vibrational frequencies to the force-field calculation of DW.[29]

No significant ^{15}N isotope shifts are calculated for A_u and B_{3u} modes of phenazine. DW's assignment of 288 cm^{-1} band to $5a_u$ is based on the force-field calculation.[29] Clearly this assignment does not agree with the B3LYP/6-31G(d,p) scaled frequency of 128 cm^{-1}. The experimental band at 128 cm^{-1} is assigned by DW to $5b_{3u}$,[29] while our calculation suggests that this band clearly belongs to $5a_u$. We also note, that the intensity reported by DW for this frequency is half that of the 288 cm^{-1} band.[29] Furthermore, the 288 cm^{-1} band is not observed by Neto *et al.*,[30] Radziszewski *et al.*,[31] and Mitchell *et al.*[32] $5b_{3u}$ B3LYP/6-31G(d,p) scaled frequency is 105 cm^{-1}, which agrees favorably with the 113 cm^{-1} band reported by Radziszewski *et al.*[31]

DW assigned the 744 cm^{-1} band to $3a_u$.[29] Although, the corresponding anthracene frequency for this mode is 743 cm^{-1},[21,22] we suggest that the DW assignment is incorrect, because the bands belonging to A_u modes do not exhibit high intensity. Unlike anthracene low-intensity 734 cm^{-1} band,[21,22] phenazine 744cm^{-1} band has high experimental

Table 5.3. Phenazine Frequencies (cm^{-1}) and Calculated IR Intensities (in Parentheses)

	B3LYP/6-31G(d,p)[a]				experiment			calculated	anthracene	comments
ν	**raw**	**SF[b]**	**scaled**	**^{15}N[c]**	**Ref. 29**	**Ref. 30**	**Ref. 31**	**Ref. 29**	**calcd/exp[d]**	
							A_g			
11	422	1	416	407	416			343	399/397	
10	623	1	614	605	612			620	629/625	
9	749	1	739	730	735			746	753/754	
8	1026	2	998	998	1013			1011	1009/1007	
7	1180	2	1148	1148	1157			1158	1159/1164	
6	1318	2	1282	1280	1280			1280	1266/1264	
5	1446	2	1406	1404	1403			1386	1408/1412	
4	1522	2	1481	1480	1479			1474	1489/1480	
3	1603	2	1560	1558	1556			1546	1564/1556	
2	3198	3	3057	3057	3051			3052	3044/3048	
1	3220	3	3078	3078	3065			3059	3065/3072	
							B_{3g}			
10	451	1	445	445	449			420	387/390	
9	573	1	566	525	525			533	532/521	525 is correct
8	938	1	926	920	871			882	916/903	questionable experimental assignment
7	1146	2	1115	1115	1127			1106	1101/1102	
6	1232	2	1199	1199	1210			1236	1184/1187	
5	1421	2	1383	1379	1348			1338	1383/1376	1374 is correct
4	1578	2	1535	1516	1529			1509	1593/1574	
3	1660	2	1615	1615	1620			1648	1639/1632	
2	3187	3	3047	3047	3059			3054	3038/3017	
1	3215	3	3074	3074	3074			3061	3054/3054	

Table 5.3 is continued on the next page.

Table 5.3. *(continued)*

	B3LYP/6-31G(d,p)[a]				experiment			calculated	anthracene	comments
ν	raw	SF[b]	scaled	^{15}N[c]	Ref. 29	Ref. 30	Ref. 31	Ref. 29	calcd/exp[d]	
							B_{1u}			
10	243 (3.76)	1	239	238	246	245		212	235/234	
9	670 (6.5)	1	661	657	657	657	658	637	655/653	
8	918 (2.6)	1	906	898	903	905	904	909	905/906	
7	1162 (11.42)	2	1131	1130	1147	1147	1148	1121	1145/1147	
6	1296 (0.14)	2	1261	1256	1275	1281	1285	1266	1260/1272	
5	1341 (0.29)	2	1305	1300	1302		1307	1319	1309/1317	
4	1518 (3.43)	2	1477	1477	1471	1478	1471	1481	1456/1448	
3	1688 (1.5)	2	1643	1643	1625	1628		1618	1639/1620	1636 is better
2	3186 (2.99)	3	3046	3046	3012	3015	3015	3055	3034/3007	
1	3215 (30.92)	3	3073	3073	3040	3069	3043	3063	3055/3084	

Table 5.3 is continued on the next page.

Table 5.3. (*continued*)

	B3LYP/6-31G(d,p)[a]				experiment			calculated	anthracene	comments
v	raw	SF[b]	scaled	^{15}N[c]	Ref. 29	Ref. 30	Ref. 31	Ref. 29	calcd/exp[d]	
							B_{2u}			
10	611 (15.73)	1	603	602	594	596	595	625	612/601	
9	842 (17.71)	1	831	824	819	821	820	828	811/809	
8	1024 (7.37)	2	996	996	1003	997	1004	1009	1008/998	
7	1163 (6.16)	2	1132	1128	1140		1140	1137	1142/1124	
6	1268 (0.37)	2	1234	1221	1209	1210	1210	1207		1234 is better
5	1396 (18.69)	2	1358	1357	1361	1364	1362	1394	1363/1397	
4	1479 (13.17)	2	1439	1438	1431	1431	1431	1427	1454/1460	
3	1571 (29.86)	2	1528	1525	1513	1514	1516	1520	1551/1534	
2	3198 (25.7)	3	3058	3058	3059	3063	3061	3053	3044/3021	
1	3218 (37.55)	3	3076	3076	3086	3088	3090	3060	3064/3048	
							B_{1g}			
4	248	4	244	244	249			304	239/244	
3	504	4	496	496	494			387	482/479	
2	800	4	788	788				767	775/760	
1	996	4	980	980	963			995	967/956	

Table 5.3 in continued on the next page.

Table 5.3. (*continued*)

	B3LYP/6-31G(d,p)[a]				experiment			calculated	anthracene	comments
ν	**raw**	**SF[b]**	**scaled**	**^{15}N[c]**	**Ref. 29**	**Ref. 30**	**Ref. 31**	**Ref. 29**	**calcd/exp[d]**	
							B_{2g}			
5	285	4	281	276	289			349	270/287	
4	597	4	587	585	585			467	575/580	
3	823	4	810	808				779	766/773	
2	903	4	888	887				956	848/?	
1	1062	4	1001	1001	992			989	988/977	
							A_u			
5	130	4	128	128	288			207	131/ --	288 is incorrect; 128 is correct
4	510	4	502	502	475			376	497/ --	
3	773	4	761	761	744			663	742/743	744 is incorrect; probably not observed
2	896	4	881	881	857			921	866/858	862 is better
1	1016	4	999	999	957			987	987/988	957 is incorrect; 995 is correct
							B_{3u}			
5	107 (2.8)	4	105	104	128	113		154	105/106	128 is incorrect
4	405 (5)	4	398	394	393	392		347	380/380	
3	506 (0.53)	4	498	492		482		507	474/474	
2	789 (129.9)	4	776	776	749	750		776	751/737	754 is better
1	995 (2.79)	4	979	979	1109			1019	971/956	1109 is incorrect; 957 is correct

[a] this work; [b] Scaling factors: 1 = 0.987, 2 = 0.973, 3 = 0.956, 4 = 0.984; [c] scaled harmonic frequencies of ^{15}N phenazine; [d] see Table 5.2.

intensity.[29, 30] The 744 cm^{-1} band is one of the high-intensity peaks that originate from one high-intensity band at 750 cm^{-1} in phenazine solution spectrum.[30] Hence an experimental band related to our calculated frequency, 761 cm^{-1}, is likely unobservable. Both DW and Neto *et al.* assign high-intensity 749 cm^{-1} and 750 cm^{-1} bands to $2b_{3u}$.[29, 30] We find, that the high-intensity 754 cm^{-1} band[30] is in a better agreement with our calculated frequency for $2b_{3u}$.

DW assignment of the 857 cm^{-1} band to $2a_u$[29] does not agree with our calculated frequency. DW also reported a band at 862 cm^{-1},[29] which we tentatively assign to this mode. The assignment of the 957 cm^{-1} band to $1a_u$[29] is clearly incorrect, due to the high experimental band intensity. Alternatively, the low-intensity band reported by DW at 995 cm^{-1} is a better match with our calculated result.[29] DW assignment of the 1109 cm^{-1} band to $1b_{3u}$ is clearly incorrect.[29] The 957 cm^{-1} band[29] agrees more favorably with our $1b_{3u}$ calculated frequency. B3LYP/6-31G(d,p) result for $4a_u$ is 27 cm^{-1} higher than experimental frequency.[29] However, we believe that the experimental assignment in this case is correct, which would represent the second example of a significant deviation between B3LYP/6-31G(d,p) and experiment for a low-frequency mode.

In summary, our B3LYP/6-31G(d,p) calculation largely supports the vibrational assignment by DW.[29] There are only few vibrational frequencies with significant nitrogen-character, such as $9b_{3g}$, where the use of our scaling factors does not yield frequencies that accurately reproduce experimental results. Due to the small number of these modes, it is unnecessary, however, to calculate a separate set of scaling factors that would account for the nitrogen-motion in the molecule. We have also suggested reassignment of certain vibrational frequencies based on our calculated results, observed intensity values, and

comparison with the anthracene vibrational spectrum.

Dibenzo[a,c]anthracene and Dibenzo[a,c]phenazine

Few experimental vibrational spectroscopy data are available for dibenzo[a,c]anthracene. Raman, IR and fluorescence spectra were reported by Périn-Roussel *et al.*[33] Schraber measured Raman spectra of several polycyclic aromatic compounds including dibenzo[a,c]anthracene.[34] Orr *et al.*[35] and Cannon *et al.*[36] have also recorded the IR spectrum of dibenzo[a,c]anthracene. We present the first DFT calculation of the dibenzo[a,c]anthracene vibrational frequencies (Table 5.4). Comparison of the scaled harmonic frequencies with the experimental infrared values is impeded by the fact that the authors did not tabulate experimental results.[33,35,36] We, therefore, compare only the high-intensity experimental infrared bands with our scaled harmonic frequencies.

We have calculated harmonic frequencies of dibenzo[a,c]phenazine, and the ^{15}N isotope-substituted dibenzo[a,c]phenazine (Table 5.4). In our calculation, the only significant isotope shifts, 20 cm^{-1} and 13 cm^{-1}, appear in $10b_2$ and $18a_1$ respectively. Therefore, just as in case of $9b_{3g}$ of phenazine, we report the experimental values for the $10b_2$ and $18a_1$ modes are different from the B3LYP/6-31G(d,p) results. Otherwise, the B3LYP/6-31G(d,p) frequencies are in favorable agreement with the experimental values.

To our knowledge, Raman spectrum of dibenzo[a,c]phenazine has not been reported; and apparently there are only two reports of the IR vibrational spectrum.[37] Our assignment of the experimental frequencies is listed in Table 5.4. Since no IR polarization data is available, we have based our assignment solely on comparison of the experimental and

Table 5.4. Dibenzo[a,c]anthracene and Dibenzo[a,c]phenazine Frequencies (cm^{-1}) and Calculated IR Intensities (in Parentheses)

dibenzo[a,c]anthracene					dibenzo[a,c]phenazine					
B3LYP/6-31G(d,p)[a]				experiment	B3LYP/6-31G (d,p)[a]					experiment
ν	raw	SF[b]	scaled	Refs. 33-36	ν	raw	SF[b]	scaled	^{15}N[c]	Ref. 37
					A_1					
35	244 (0.26)	1	241	247	33	237 (1.34)	1	234	233	
34	333 (0.11)	1	328	330	32	347 (0.66)	1	343	342	
33	415 (0.15)	1	409		31	413 (1.9)	1	408	407	
32	587 (11.2)	1	579		30	585 (10.34)	1	578	574	574
31	640 (0.67)	1	632		29	631 (6.1)	1	623	615	616, 615
30	710 (0.58)	1	701		28	711 (1.53)	1	702	697	
29	777 (0.19)	1	767		27	775 (0.98)	1	765	759	766, 764
28	824 (0.82)	1	814	810	26	830 (8.72)	1	820	815	816
27	1037 (0)	2	1009	1011	25	1029 (1.84)	2	1001	1001	
26	1050 (4.76)	2	1022		24	1062 (20.39)	2	1033	1032	1039
25	1091 (0)	2	1062		23	1095 (6.12)	2	1065	1064	1066
24	1139 (0.06)	2	1108		22	1137 (4.44)	2	1106	1106	1106, 1107
23	1188 (0.22)	2	1156		21	1177 (0.49)	2	1145	1143	1145
22	1205 (5.89)	2	1172		20	1193 (6.82)	2	1160	1160	
21	1237 (0)	2	1204		19	1262 (5.73)	2	1228	1226	1225, 1226
20	1275 (2.7)	2	1240	~1240	18	1298 (3.34)	2	1263	1249	1268, 1269
19	1296 (2.56)	2	1261	1255	17	1308 (13.48)	2	1272	1272	
18	1345 (1.18)	2	1311		16	1363 (0.43)	2	1326	1323	
17	1374 (0.02)	2	1337		15	1388 (100.77)	2	1351	1351	1344
16	1410 (0.51)	2	1372	1360	14	1397 (11.95)	2	1359	1358	1358, 1359
15	1444 (0.61)	2	1405		13	1449 (9.95)	2	1409	1406	1402
14	1473 (15.21)	2	1433	1436	12	1483 (0.01)	2	1443	1443	
13	1491 (3.91)	2	1451		11	1513 (1.45)	2	1472	1471	

Table 5.4 in continued on the next page.

Table 5.4. (*continued*)

dibenzo[a,c]anthracene					dibenzo[a,c]phenazine					
B3LYP/6-31G(d,p)[a]				experiment	B3LYP/6-31G (d,p)[a]					experiment
ν	raw	SF[b]	scaled	Refs. 33-36	ν	raw	SF[b]	scaled	^{15}N[c]	Ref. 37
12	1517 (0.18)	2	1476		10	1544 (42.7)	2	1502	1501	1500
11	1557 (14.85)	2	1515		9	1599 (5.43)	2	1555	1554	
10	1613 (1.1)	2	1569		8	1621 (0.17)	2	1577	1576	
9	1620 (0.25)	2	1577		7	1661 (12.57)	2	1616	1616	1614
8	1663 (0.22)	2	1618		6	3186 (12.66)	3	3046	3046	
7	3179 (0.54)	3	3039		5	3198 (14.74)	3	3057	3057	
6	3183 (4.67)	3	3043		4	3199 (12.89)	3	3058	3058	
5	3194 (31.06)	3	3053		3	3216 (27.6)	3	3075	3075	
4	3202 (48.72)	3	3061	~3060 ?[d]	2	3224 (22.25)	3	3082	3082	
3	3206 (1.85)	3	3065		1	3228 (17.94)	3	3086	3086	
2	3225 (18.49)	3	3083							
1	3231 (28.42)	3	3089							
					B_2					
33	159 (0.26)	1	157		32	149 (0.25)	1	147	147	
32	320 (0.93)	1	316	314	31	333 (1.09)	1	329	327	
31	458 (0.1)	1	452		30	457 (0)	1	451	449	
30	549 (0.18)	1	542		29	568 (0.13)	1	561	558	
29	606 (0.05)	1	598		28	628 (0.06)	1	620	616	
28	693 (0.38)	1	684		27	631 (2.82)	1	623	623	
27	904 (0.65)	1	892		26	698 (2.18)	1	689	687	687
26	976 (0.03)	1	963		25	912 (0.09)	1	900	894	
25	1024 (1.01)	2	996		24	998 (5.71)	1	985	979	
24	1084 (3.21)	2	1055	~1050	23	1026 (0.83)	2	998	998	
23	1158 (0.29)	2	1126		22	1075 (1.91)	2	1046	1046	

Table 5.4 is continued on the next page.

Table 5.4. *(continued)*

dibenzo[a,c]anthracene					dibenzo[a,c]phenazine					
	B3LYP/6-31G(d,p)[a]			experiment		B3LYP/6-31G (d,p)[a]				experiment
ν	raw	SF[b]	scaled	Refs. 33-36	ν	raw	SF[b]	scaled	$^{15}N^{c}$	Ref. 37
22	1167 (0.36)	2	1136		21	1151 (0.05)	2	1120	1120	
21	1198 (1.32)	2	1166		20	1158 (8.3)	2	1126	1125	1126
20	1237 (0.64)	2	1204		19	1191 (2.84)	2	1159	1159	
19	1263 (1.81)	2	1229		18	1256 (2.72)	2	1222	1220	
18	1319 (2.92)	2	1284		17	1270 (0)	2	1236	1230	
17	1338 (0.11)	2	1302		16	1331 (11.65)	2	1295	1292	1306
16	1360 (2.04)	2	1323	1326	15	1364 (0.01)	2	1327	1325	
15	1392 (1.28)	2	1354	~1350	14	1392 (4.59)	2	1355	1352	
14	1479 (6.81)	2	1439	1446	13	1491 (30.46)	2	1451	1450	1448
13	1498 (4.37)	2	1458		12	1506 (0.01)	2	1465	1465	1465
12	1537 (9.91)	2	1496	~1490	11	1538 (8.49)	2	1496	1496	1492
11	1633 (0.26)	2	1589	1593	10	1590 (4.31)	2	1547	1528	1544
10	1655 (1.61)	2	1610		9	1637 (0.34)	2	1593	1593	
9	1668 (0.01)	2	1623		8	1668 (0.79)	2	1623	1623	
8	1687 (0.13)	2	1642		7	1676 (1.83)	2	1631	1630	
7	3172 (1.01)	3	3033		6	3184 (2.69)	3	3044	3044	
6	3182 (0.74)	3	3042		5	3186 (1.25)	3	3046	3046	
5	3189 (33.43)	3	3049		4	3199 (40.61)	3	3059	3059	
4	3195 (44.35)	3	3054	3054	3	3211 (1.53)	3	3070	3070	
3	3203 (0.28)	3	3062		2	3213 (13.59)	3	3072	3072	
2	3212 (0)	3	3071		1	3226 (16.43)	3	3084	3084	
1	3223 (50.66)	3	3081							

Table 5.4 is continued on the next page.

Table 5.4. (*continued*)

dibenzo[a,c]anthracene					dibenzo[a,c]phenazine					
B3LYP/6-31G(d,p)[a]				experiment	B3LYP/6-31G (d,p)[a]					experiment
v	**raw**	**SF[b]**	**scaled**	**Refs. 33-36**	**v**	**raw**	**SF[b]**	**scaled**	**$^{15}N^{c}$**	**Ref. 37**
					A_2					
17	63	4	62	63	16	73	4	72	71	
16	109	4	108		15	125	4	123	123	
15	230	4	227	219	14	239	4	235	233	
14	291	4	287	298 ?[d]	13	307	4	302	300	
13	461	4	453		12	464	4	456	456	
12	552	4	543		11	564	4	555	554	
11	568	4	559		10	572	4	563	562	
10	706	4	695	698	9	728	4	716	715	
9	767	4	755		8	792	4	780	779	
8	786	4	773		7	810	4	797	797	
7	798	4	785		6	835	4	822	819	
6	868	4	855		5	900	4	886	885	
5	883	4	869		4	902	4	888	888	
4	910	4	895		3	986	4	970	970	
3	965	4	949		2	1013	4	997	997	
2	997	4	981		1	1016	4	1000	1000	
1	1003	4	987							

Table 5.4 is continued on the next page.

Table 5.4. *(continued)*

dibenzo[a,c]anthracene					dibenzo[a,c]phenazine					
B3LYP/6-31G(d,p)[a]				experiment	B3LYP/6-31G (d,p)[a]					experiment
ν	raw	SF[b]	scaled	Refs. 33-36	ν	raw	SF[b]	scaled	^{15}N[c]	Ref. 37
					B_1					
16	70 (0.29)	4	69		15	84 (1.5)	4	83	82	
15	99 (1.03)	4	97	82	14	112 (68.81)	4	110	110	
14	181 (0.18)	4	178		13	185 (4.12)	4	182	181	
13	314 (0.34)	4	309	298 ?[d]	12	332 (0.02)	4	327	325	
12	426 (0.73)	4	419		11	436 (4.59)	4	429	427	
11	439 (0.68)	4	432		10	459 (42.7)	4	452	451	439
10	483 (7.57)	4	475		9	505 (0.21)	4	497	494	
9	561 (3.02)	4	552		8	574 (30.04)	4	565	564	555
8	737 (19.95)	4	725	~725	7	748 (48)	4	736	736	
7	776 (0.11)	4	763		6	793 (5.68)	4	780	780	744, 745
6	788 (110.32)	4	775	~765	5	799 (109.53)	4	786	787	784
5	879 (1.74)	4	865		4	903 (12.24)	4	888	888	871
4	905 (32.49)	4	891	~885	3	990 (0.73)	4	975	975	
3	971 (2.17)	4	956	~950	2	993 (2.96)	4	977	977	976, 975
2	984 (3.67)	4	969		1	1015 (23.85)	4	999	999	
1	1001 (0.19)	4	985							

[a] this work; [b] Scaling factors: 1 = 0.987, 2 = 0.973, 3 = 0.956, 4 = 0.984; [c] scaled harmonic frequencies of ^{15}N dibenzo[a,c]phenazine;

[d] ?: tentative assignment.

calculated frequency and intensity values.

In summary, we have calculated the vibrational harmonic frequencies for dibenzo[a,c]anthracene and dibenzo[a,c]phenazine. The scaled frequencies shown in Table 5.4 are in good agreement with experimental results and have aided in the assignment of several experimental vibrational bands.

Conclusion

We have performed B3LYP/6-31G(d,p) calculation of vibrational frequencies of several polycyclic aromatic compounds and their heterocyclic analogs. We have obtained a set of scaling factors based on comparisons between experimental and calculated frequencies of phenanthrene and anthracene. These scaling factors were applied to the calculated harmonic vibrational frequencies of phenanthrene, anthracene, phenazine, dibenzo[a,c]anthracene, and dibenzo[a,c]phenazine. As a result, we were able to generate scaled harmonic frequencies that are in good agreement with the experimental values. In the case of phenazine, the modes that showed significant isotope shifts required a different scaling factor in order to match experimental values. However, there were only few such modes and, therefore, we did not develop a separate set of scaling factors for the aromatic heterocycles investigated here. Owing to a limited amount of experimental data for dibenzo[a,c]anthracene and dibenzo[a,c]phenazine, we were not able to fully test the validity of our calculated results. We showed, however, that the B3LYP/6-31G(d,p) calculations

successfully reproduced experimental frequencies of phenanthrene, anthracene, and phenazine; we, therefore, believe that our calculations of vibrational frequencies of dibenzo-molecules are accurate as well.

References and Notes

(1) R. G. Parr, Yang, W. *Density-Functional Theory of Atoms and Molecules*; Oxford University Press: Oxford, U. K., **1989**.

(2) Labanowski, J. K.; Andzelm, J. W., Ed. *Density Functional Methods in Chemistry*; Springer-Verlang: Berlin, **1991**.

(3) Hohenberg, P.; Kohn, W. *Phys. Rev.* **1964**, *B136*, 864-876.

(4) Kohn, W.; Sham, L. J. *Phys. Rev.* **1965**, *A137*, 1617-1620.

(5) Martin, .J. M. L.; El-Yazal., J.; François, J-P.; *J. Phys. Chem.* **1996**, *100*, 15358-15367.

(6) Birks, J. B., Ed. *Organic Molecular Photophysics*; John Wiley & Sons: London, **1975**; Vol.2.

(7) Murrell, J. N. *The Theory of the Electronic Spectra of Organic Molecules*; Methuen & Co LTD: London, **1963**; Ch. 6.

(8) Akiyama, I.; Li, K. C.; LeBreton, P. R.; Fu, P. P.; Harvey, R. G. *J. Phys. Chem.* **1979**, *83*, 2997-3003.

(9) Schmidt, J. *Chem. Phys.* **1977**, *66*, 828.

(10) Marcus, R. A.; Sutin, N. *Biochimica et Biophysica Acta* **1985**, *811*, 265-322.

(11) Jaguar version 3.5, Schrödinger Inc.: Portland, OR, **1999**.

(12) Becke, A.D. *J. Chem. Phys.* **1993**, *98*, 5648-5652.

(13) Lee, C.; Yang, W.; Parr, R. G. *Phys. Rev.* **1988**, *B37*, 785-789.

(14) Becke, A. D. *Phys. Rev.* **1989**, *A38*, 3098-3100.

(15) Vosko, S. H.; Wilk, L.; Nusair, M. *Can. J. Phys.* **1980**, *58*, 1200-1211.

(16) Bree, A.; Solven, F.G.; Vilkos, V. V. B. *J. Mol. Spec.* **1972**, *44*, 298-319.

(17) Canè, E.; Miani, A.; Palmieri, P.; Tarroni R.; Trombetti, A. *Spectroscop. Acta* **1997**, *A53*, 1839-1851.

(18) Warren, J. A.; Hyes, J. M.; Small, G. J. *Chem Phys.* **1986**, *102*, 323-336.

(19) Cyvin, S. J.; Neerland, G.; Bruvoll, J.; Cyvin, B. N. *Spectrosc. Lett.* **1981**, *14*, 37-45.

(20) Rougeau, N.; Flament, J. P.; Youkharibache, P.; Gervais, H. P.; Berthier, G. *J. Mol. Struct., (THEOCHEM)* **1992**, *254*, 405-428.

(21) Bakke, A.; Cyvin, B. N.; Whitmer, J. C.; Cyvin, S. J.; Gustavsen, J. E.; Klaeboe, P. *Z. Naturforsch* **1979**, *A34*, 579-584.

(22) Neerland, G.; Cyvin, B. N.; Brunvoll, J.; Cyvin, S. J.; Klaeboe, P. *Z. Naturforsch* **1980**, *A35*, 1390-1394.

(23) Szczepanski, J.; Vala, M.; Talbi, D.; Parisel, O.; Ellinger, Y. *J. Chem. Phys.* **1993**, *98*, 4494-4511.

(24) Schettino, V.; Neto, N.; Califano, S. *J. Chem. Phys.* **1966**, *44*, 2724-2734.

(25) Witt, K.; Mecke, R. *Z. Naturforsch* **1967**, *22A*, 1247-1254.

(26) Räsänen, J.; Stenman, F.; Penttinen, E. *Spectrochim. Acta* **1973**, *A29*, 395-403.

(27) Bolotnikova, T. N. *Izv. Akad. Nauk SSSR, Ser. Fiz.* **1959**, *23*, 29-31.

(28) Neto, N.; Scrocco, M.; Califano, S. *Spectroschim. Acta* **1966**, *A22*, 1981.

(29) Durnick, T. J.; Wait, S. C. Jr. *J. Molec. Spectr.* **1972**, *42*, 211-226.

(30) Neto, N.; Ambrosino, F.; Califano, S. *Spectrochim. Acta* **1964**, *A20*, 1503-1516.

(31) Radziszewski, J. G.; Michl, J. *J. Chem. Phys.* **1985**, *82*, 3527-3533.

(32) Mitchell, M. B.; Smith, G. R.; Guillory, W. A. *J. Chem. Phys.* **1981**, *75*, 44-48.

(33) Périn-Roussel, O.; Jacquignon. P.; Saperas, B.; Viallet, P. *C.R.Acad. Sc. Paris, Série* **1953**, *C274*, 1593.

(34) Schrader, B. *Appl. Spectrosc.* **1991**, *45*, 1230-1232.

(35) Orr, S. F. D.; Thompson, H. W. *J. Chem. Soc.* **1950**, 218-221.

(36) Cannon, C. G.; Sutherland, G. B. B. M. *Spectrochim. Acta* **1951**, *A4*, 373-395.

(37) Nujol mull and KBr disc IR spectra were recorded by K. Tanabe and T. Tamura at National Institute of Material and Chemical Research (NIMC), Japan. Spectra are available at aist.go.jp.

Chapter 6

X-ray Crystallographic Study and *ab initio* Calculations of the Molecular Geometry of Dibenzo[a,c]phenazine

Acknowledgments:

Many thanks to Michael Day and Lawrence Henling at the Beckman Institute X-ray Crystallography Laboratory. Some of this work was done at the Molecular Simulation Center at Caltech.

Introduction

The main objective of my thesis research has been to obtain electron-transfer reorganization energies, λ, of isolated molecules; the experimental values of λ have been extracted from the fine structure analyses of photoelectron spectra (see Chapters 2 and 3 for detailed discussion). Throughout this work, *ab initio* calculations (i.e., density functional theory) have been successfully used to aid the assignments of the ionization bands, and the vibrational modes. Reorganization energies have been also calculated from the single point energy values and have been found to be in favorable agreement with the experimental results.[1] The success of an *ab initio* calculation greatly depends on how accurately a particular level of theory can reproduce a molecular geometry (e.g, how well the calculated bond lengths and angles compare to the experimental values from X-ray crystallographic studies). It has been established that *ab initio* calculation methods, such as DFT, coupled with extended basis sets are more rigorous at predicting correct geometries than Hartree-Fock or any semiclassical method (the latter methods do not take into account the electron correlation effect).[2]

Among the systems that have been studied are polycyclic aromatic molecules containing nitrogen. These molecules are often employed as redox active components in donor-bridge-acceptor models of chemical and biological ET processes.[3] Surprisingly, few X-ray crystal structures of these molecules are available for comparisons with calculated geometries. This motivated us to obtain an X-ray crystal structure of dibenzo[a,c]phenazine (DBP) (one of the molecules extensively studied in Chapter 2), thereby allowing a

comparison of the experimental molecular geometry with *ab initio* calculation results. By doing this, we hoped to show any deficiencies of the computational method that has been used throughout this work, which may result in inaccurate optimized geometries and single point energy values.

Materials and Methods

Synthesis of DBA

9,10-phenanthrenequinone (Aldrich), 1,2-diaminobenzene (Aldrich) and dry methanol (Aldrich) were used without further purification. NMR spectra were obtained on a Varian Mercury 300 FT spectrometer operating at 300 Hz. A sample of 4.80 mmol (1.00 g) of 9,10-phenanthrenequinone was placed into 500 ml flask equipped with a reflux condenser and a magnetic stir bar. Methanol (200 ml) was added to the flask and the mixture was slowly heated and stirred for 30 min. 4.80 mmol (520 mg) of 1,2-diaminobenzene were added to the reaction mixture which was further heated to reflux for 1 h. The yellow precipitate was collected on a Büchner funnel and dried in a vacuum desiccator. The product, DBP (1.25 g, 93%), was purified either by vacuum sublimation or recrystallization from MeOH/CH_2Cl_2 or DMSO. ^{1}H-NMR (DMSO-d_6): δ 9.3 (dd, 2H, J = 8.2 Hz), 8.8 (dd, 2H, J = 7.6 Hz), 8.4, 8.0 (AA'BB', 4H), 7.9 (m, 4H); ^{13}C NMR (DMSO-d_6): δ 141.5, 141.3, 131.4, 130.8, 130.5, 129.2, 129.0, 128.2, 125.5, 123.6. Analytical: calculated values for $C_{20}H_{12}N_2$: C, 85.69; H, 4.31; N, 10.00; experimental values for $C_{20}H_{12}N_2$: C, 85.90; H, 4.10; N, 9.91.

Table 6.1. Crystal Data and Structure Refinement for DBP

Empirical formula	$C_{20}H_{12}N_2$
Formula weight	280.32
Crystallization solvent	Vacuum sublimation
Crystal habit	Thin plate
Crystal size	0.370 x 0.296 x 0.011 mm^3
Crystal color	Pale yellow
Preliminary photos	Rotation
Type of diffractometer	CCD are detector
Temperature	98K
θ range for 4869 reflections used in lattice determination	2.26 to 27.81°
Unit cell dimensions	a = 5.1818(19) Å b = 14.361(5) Å c = 17.977(7) Å
Volume	1337.7(8) $Å^3$
Z	4
Crystal system	Orthorhombic
Space group	$P2_12_12_1$
Density (calculated)	1.392 Mg/m^3
F(000)	584
Data collection program	Bruker Smart
θ range for data collection	1.81 to 28.40°
Completeness to θ = 28.40°	94.4%
Index ranges	$-6 \leq h \leq 6, -18 \leq k \leq 18, -22 \leq l \leq 23$
Data collection scan type	ω scans at 3φ settings
Data reduction program	Bruker SAINT v 6.2
Reflections collected	15373
Independent reflections	3085 [R_{int} = 0.1332]
Absorption coefficient	0.083 mm^{-1}
Primary solution method	Direct methods
Secondary solution methods	Direct methods
Hydrogen placement	Difference Fourier map
Refinement method	Full matrix least-squares on F^2
Data/restraints/parameters	3085/0/247
Treatment of hydrogen atoms	Unrestrained
Goodness-of-fit on F^2	1.502
Final R indices [$I>2\sigma(I)$, 2344 reflections]	R1 = 0.0521, wR2 = 0.1023
R indices (all data)	R1 = 0.0723, wR2 = 0.1061
Type of weighting scheme used	Sigma
Weighting scheme used	$w = 1/\sigma^2(Fo^2)$
Max shift/error	0.000
Average shift/error	0.000
Absolute structure parameter	-4(4)
Largest diff. peak and hole	0.224 and -0.274 e. $Å^{-3}$

X-ray Crystallography

Thin pale yellow needles of DBP were formed by vacuum sublimation. One of these needles was used to cut a small crystal (0.370 x 0.296 x 0.011 mm^3) employed in the X-ray study. Diffraction data were collected using a Bruker SMART 1000 CCD area detector at 98 K with graphite monochromated MoKα radiation (λ = 0.71073 Å). Crystal data and the details of data collection and structure determination are given in Table 6.1. Unit cell parameters were obtained by least-squares refinement of the 4869 reflections in the range $2.26 \leq \theta \leq 27.81°$: 15373 reflections were collected for the $1.81 \leq \theta \leq 28.40°$ range; of these,

Table 6.2. Atomic Coordinates ($x10^4$) and Equivalent Isotropic Displacement Parameters ($Å^2 x10^3$) for DBP

atoms	x	y	z	U_{eq}
N(1)	-1817(5)	978(1)	4740(1)	22(1)
N(2)	-2272(4)	-150(1)	3456(1)	21(1)
C(1)	1804(6)	533(2)	5853(1)	27(1)
C(2)	3613(6)	342(2)	6380(2)	28(1)
C(3)	5297(6)	-412(2)	6281(2)	28(1)
C(4)	5136(6)	-943(2)	5646(1)	26(1)
C(5)	4919(5)	-2034(2)	4249(1)	22(1)
C(6)	4788(5)	-2526(2)	3595(1)	25(1)
C(7)	2870(5)	-2339(1)	3076(2)	24(1)
C(8)	1091(5)	-1644(2)	3215(1)	22(1)
C(9)	-5766(5)	803(2)	3037(2)	23(1)
C(10)	-7351(5)	1560(2)	3136(2)	27(1)
C(11)	-7078(6)	2133(2)	3769(2)	27(1)
C(12)	-5256(6)	1953(2)	4292(2)	27(1)
C(13)	3317(5)	-754(1)	5093(1)	21(1)
C(14)	3151(5)	-1306(1)	4400(1)	19(1)
C(15)	1234(5)	-1114(1)	3870(1)	19(1)
C(16)	-537(5)	-324(1)	3980(1)	18(1)
C(17)	-3846(5)	597(1)	3567(1)	21(1)
C(18)	-3589(5)	1159(1)	4210(1)	22(1)
C(19)	-314(5)	233(1)	4635(1)	21(1)
C(20)	1606(5)	9(1)	5199(1)	22(1)

Table 6.3. Hydrogen Coordinates (x 10^4) and Isotropic Displacement Parameters ($Å^2$ x 10^3) for DBP

	x	y	z	U_{iso}
H(1)	640(60)	987(16)	5901(15)	32(8)
H(2)	3590(60)	646(15)	6813(15)	30(7)
H(3)	6530(50)	-568(13)	6655(13)	13(6)
H(4)	6260(60)	-1418(14)	5595(14)	30(8)
H(5)	6200(50)	-2193(12)	4592(13)	11(6)
H(6)	6020(60)	-2934(15)	3487(15)	33(8)
H(7)	2840(60)	-2655(14)	2606(15)	26(7)
H(8)	-320(50)	-1541(14)	2870(13)	14(6)
H(9)	-5890(60)	418(14)	2590(14)	30(7)
H(10)	-8720(60)	1732(15)	2769(14)	30(7)
H(11)	-8120(60)	2649(15)	3817(15)	28(7)
H(12)	-5010(50)	2327(14)	4738(13)	20(6)

3085 independent reflections were recorded (R_{int} = 0.1332). The reflection data were

Table 6.4. Anisotropic Displacement Parameters ($Å^2$ x10^4) for DBP

Atoms	U^{11}	U^{22}	U^{33}	U^{23}	U^{13}	U^{12}
N(1)	262(12)	115(9)	292(11)	27(7)	6(10)	-24(9)
N(2)	235(12)	119(9)	269(11)	35(7)	-16(9)	-25(8)
C(1)	329(16)	176(13)	288(15)	3(10)	7(12)	-28(12)
C(2)	392(17)	199(12)	258(14)	-14(11)	-1(12)	-70(12)
C(3)	287(16)	252(12)	289(15)	72(11)	-69(12)	-44(12)
C(4)	263(15)	184(12)	318(15)	71(10)	-5(12)	-25(12)
C(5)	187(14)	177(12)	303(14)	69(10)	6(11)	4(11)
C(6)	238(15)	145(11)	357(15)	18(10)	49(12)	3(11)
C(7)	284(15)	151(11)	278(14)	-11(10)	31(12)	-28(10)
C(8)	212(14)	184(12)	262(14)	35(10)	1(11)	-39(10)
C(9)	251(15)	166(11)	283(15)	50(10)	6(11)	-47(10)
C(10)	218(15)	258(13)	344(15)	112(11)	-8(12)	-7(11)
C(11)	258(15)	153(12)	390(16)	54(11)	49(12)	27(11)
C(12)	295(16)	150(12)	349(15)	15(10)	48(12)	-4(11)
C(13)	244(14)	128(10)	260(13)	31(9)	6(11)	-54(10)
C(14)	207(14)	111(10)	263(13)	46(8)	19(11)	-35(10)
C(15)	203(14)	109(10)	245(13)	44(9)	23(10)	-25(9)
C(16)	203(14)	101(10)	248(12)	44(9)	2(10)	-41(9)
C(17)	219(14)	115 (10)	289(14)	39(9)	19(10)	-31(9)
C(18)	223(14)	142(11)	296(14)	46(10)	27(11)	-42(10)
C(19)	232(14)	123(10)	261(13)	31(9)	28(11)	-21(10)
C(20)	251(15)	139(11)	255(12)	42(9)	19(11)	-58(10)

corrected for Lorentz and polarization effects.

The structure of DBP was solved with direct methods SHELXS-97[4] and refined using full matrix least-squares method SHELXL-97,[5] minimizing $\sum w(|Fo|-|Fc|)^2$, where $w = 1/\sigma^2(Fo^2)$. Carbon and nitrogen atoms were refined with anisotropic (and hydrogen atoms with isotropic) temperature factors. Refinement of F^2 was performed against all reflections. The atomic coordinates and equivalent isotropic displacement parameters for nonhydrogen atoms are found in Table 6.2, where U_{eq} is defined as the trace of the orthogonalized U^{ij} tenzor, $U_{eq} = \frac{1}{3}\sum i \sum j U_{ij}\ a_i^* a_j^* \mathbf{a}_i \mathbf{a}_j$. The atomic coordinates and equivalent isotropic displacement parameters for hydrogens are set out in Table 6.3. Anisotropic displacement parameters for nonhydrogen atoms are listed in Table 6.4. All of crystallographic data have been deposited at the CCDC, 12 Union Road, Cambridge CB2 1EZ, UK and copies can be obtained on request, by quoting the publication citation and the deposition number 142042.

Computational Details

Geometry optimization calculations were carried out using the Jaguar 3.5 package.[6] Two *ab initio* methods were used. One of them, B3LYP, consists of the hybrid exchange functional proposed by Becke[7] and the Lee-Yang-Parr[8] correlation functional. The former is a linear combination of the local density approximation, Becke's gradient correction,[9] and the Hartree-Fock exchange energy based on Kohn-Sham orbitals.[10] The other method is local Møller-Plesset second-order perturbation theory (LMP2).[11] The 6-31G(d,p) basis was used throughout the calculation.

Figure 6.1. Molecular structure of DBP indicating the atomic numbering scheme. The thermal ellipsoids have been drawn at 50% probability level.

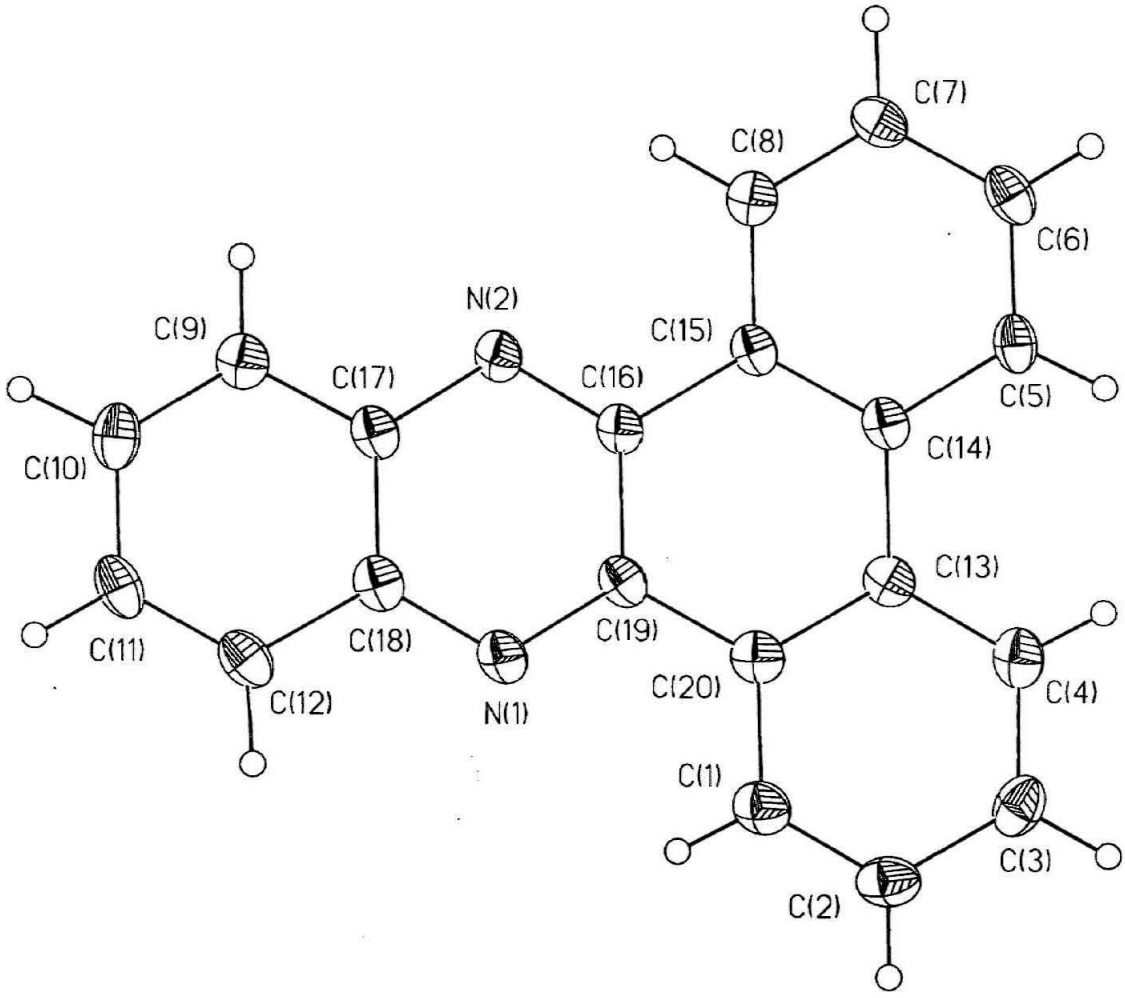
C(7)
C(8)
C(6)
N(2)
C(9)
C(15)
C(17)
C(16)
C(5)
C(10)
C(14)
C(13)
C(11)
C(18)
C(19)
C(4)
C(12)
N(1)
C(20)
C(1)
C(3)
C(2)

Figure 6.2. Unit cell contents of DBP showing the unit cell boundaries.

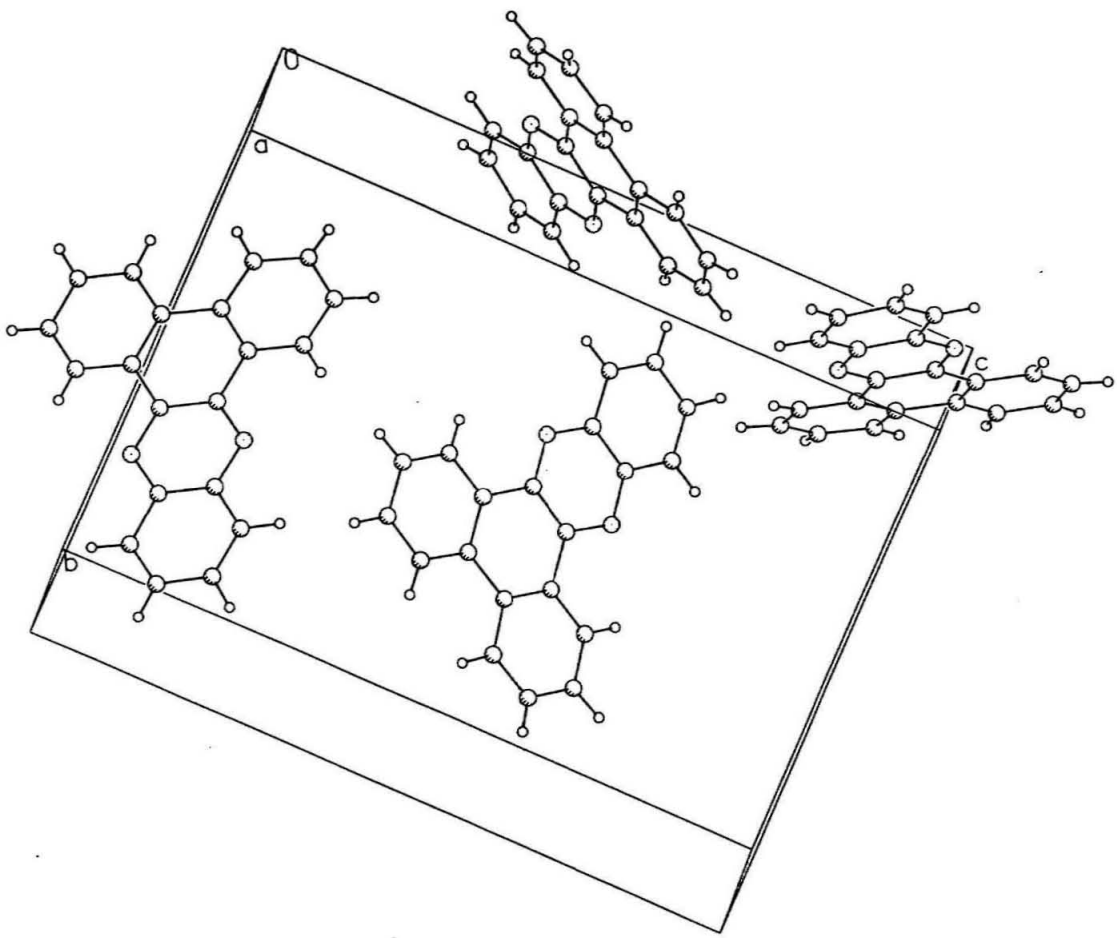
a
c

Results and Discussion

X-ray Crystal Structure

The DBP crystal structure is shown in Figure 6.1. DBP crystallizes in an orthorhombic $P2_12_12_1$ space group with four molecules in the unit cell (Figure 6.2). Figure 6.3 shows four distinct stacking arrangements of DBP molecules along the *a*-axis. Such structural types have been classified in the case of fused-ring aromatic hydrocarbons[12] and diazapyrenes.[13] Gavezzotti and Desiraju have identified these structural types as herring bone (HB), sandwich-herringbone (SHB), β, and γ structures based on the relative orientation of molecular planes in the crystal with respect to the shortest cell axis (SCA).[12] When SCA is less than 5.4 Å, the structural type is HB; β structures are identified by SCA<4.0 Å; and γ structures are characterized by 4.6<SCA<4.0 Å. In the SHB structures the molecular pairs are organized in an HB fashion. Examples of an HB structure are benzene[14] and naphthalene;[15] pyrene molecules are arranged according to an SHB structural type;[16] tribenzopyrene molecules crystallize in a β structure;[17] and the arrangement of coronene molecules is an example of a γ structure.[18] Kiraji *et al.* showed that geometrical parameters developed by Gavezzotti and Desiraju[12] are applicable to heteroaromatic complexes, such as diazapyrenes.[13]

DBP molecules arrange themselves in a distorted SHB-type structure, where the planes of the molecules in the same molecular pair are not strictly parallel to each other. Also, the planes of the molecules in the different molecular pairs are almost perpendicular to each other. One other example of such an orientation is 1:12 benzperylene, where the normal

Figure 6.3. View of DBP along the *a*-axis showing the stacking of molecules.

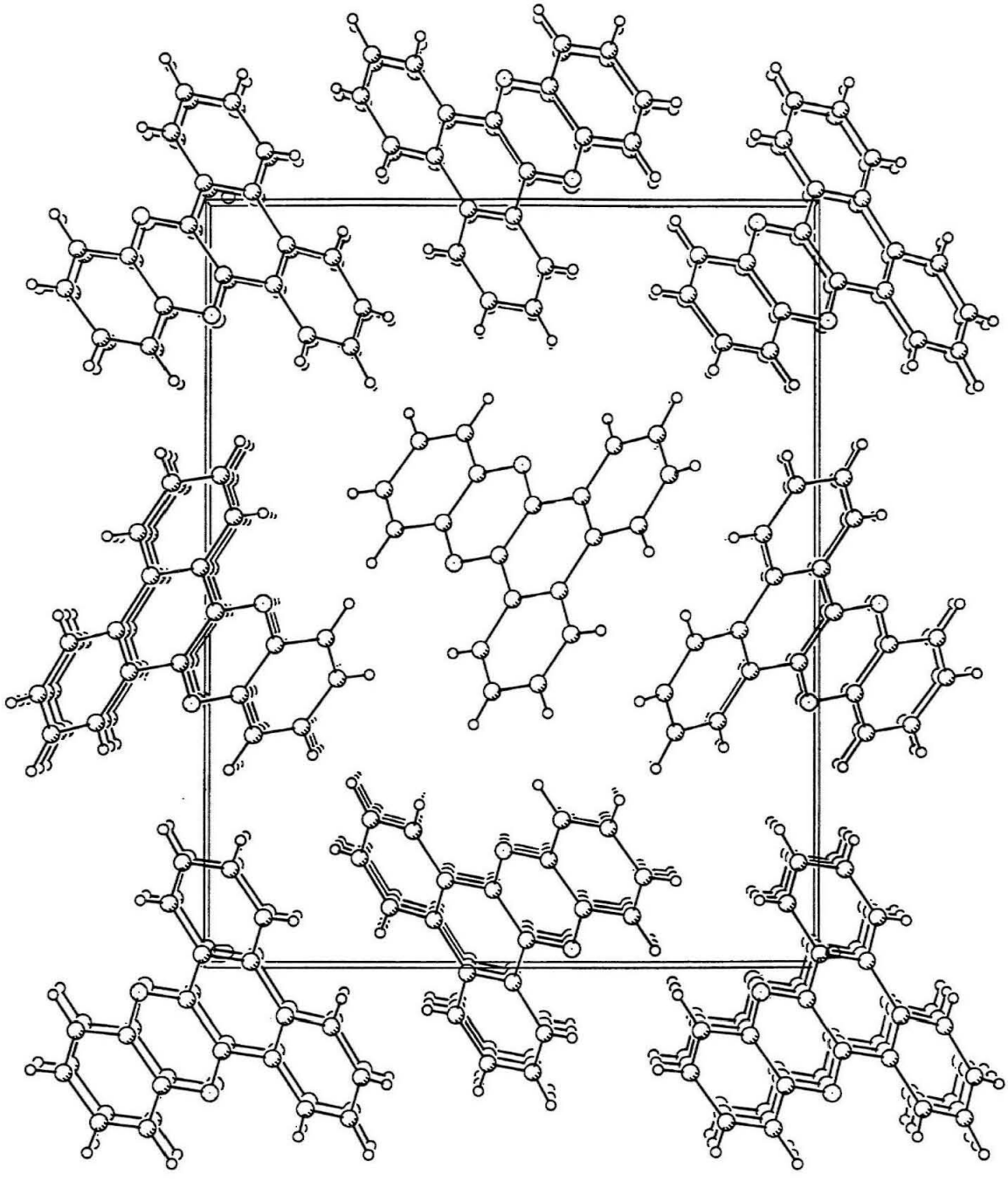

projection of two parallel molecules demonstrates that their alignment is not collinear.[19] In the normal projection these two molecules are related by a center of symmetry, which defines the distance between them. Unlike 1:12 benzperylene, DBP molecules are located a significant distance from one another. It is hard to estimate this distance, because molecules in the molecular pair are not parallel (i.e., they are not related by a center of symmetry). The arrangement of DBP molecules observed here is most likely due to nitrogen lone-pair steric repulsion.

Needles of DBP elongate along [010]. Needles of α-phenazine also elongate along [010].[20,21] The allotrope of α-phenazine is β-phenazine; its needles elongate along [001].[21] In this work we were able to obtain only one allotrope of dibenzo[a,c]phenazine.

Molecular Structure

Bond lengths and angles obtained from X-ray studies and the *ab initio* calculation are set out in Table 6.5. Calculated C-C and C-N bond lengths are in excellent agreement with experimental values: the difference is in the range 0.004-0.020 ± 0.002-0.004 Å. The worst agreement is found between the calculated and experimental values for C-H bonds (0.10-0.20 ± 0.02-0.03 Å). Due to the nature of the X-ray diffraction experiment, it is hard to measure the exact positions of hydrogen atoms and thus accurately determine the bond lengths between hydrogen atoms and other atoms in the molecule. We find no significant differences between the B3LYP and LMP2 results, although the former calculation gives slightly better bond lengths.

Experimentally observed C-C-C and C-C-H angles agree well with calculated results:

Table 6.5. Experimental and Calculated Bond Lengths (Å) and Angles (Deg) of DBP

	X-ray	B3LYP/6-31G(d,p)	LMP2/6-31G(d,p)
bonds			
$R_{N(1)-C(19)}$	1.337(3)	1.329	1.326
$R_{N(1)-C(18)}$	1.349(3)	1.353	1.375
$R_{N(2)-C(16)}$	1.327(3)	1.329	1.327
$R_{N(2)-C(17)}$	1.362(3)	1.353	1.374
$R_{C(1)-C(2)}$	1.362(4)	1.385	1.381
$R_{C(1)-C(20)}$	1.400(3)	1.408	1.415
$R_{C(1)-H(1)}$	0.89(3)	1.084	1.082
$R_{C(2)-C(3)}$	1.401(4)	1.402	1.411
$R_{C(2)-H(2)}$	0.89(3)	1.086	1.083
$R_{C(3)-C(4)}$	1.377(4)	1.387	1.384
$R_{C(3)-H(3)}$	0.95(2)	1.086	1.084
$R_{C(4)-C(13)}$	1.397(4)	1.411	1.418
$R_{C(4)-H(4)}$	0.90(3)	1.084	1.081
$R_{C(5)-C(6)}$	1.374(4)	1.387	1.383
$R_{C(5)-C(14)}$	1.417(3)	1.411	1.418
$R_{C(5)-H(5)}$	0.93(2)	1.084	1.081
$R_{C(6)-C(7)}$	1.389(4)	1.402	1.411
$R_{C(6)-H(6)}$	0.89(3)	1.086	1.084
$R_{C(7)-C(8)}$	1.382(3)	1.385	1.381
$R_{C(7)-H(7)}$	0.96(3)	1.086	1.083
$R_{C(8)-C(15)}$	1.402(3)	1.408	1.415
$R_{C(8)-H(8)}$	0.97(3)	1.084	1.082
$R_{C(9)-H(10)}$	1.373(3)	1.375	1.374
$R_{C(9)-H(17)}$	1.408(4)	1.422	1.426
$R_{C(9)-H(9)}$	0.98(2)	1.085	1.083
$R_{C(10)-C(11)}$	1.411(4)	1.423	1.428
$R_{C(10)-H(10)}$	1.00(3)	1.086	1.084
$R_{C(11)-C(12)}$	1.357(4)	1.375	1.374
$R_{C(11)-H(11)}$	0.92(3)	1.086	1.084
$R_{C(12)-C(18)}$	1.438(3)	1.422	1.425
$R_{C(12)-H(12)}$	0.97(2)	1.085	1.083
$R_{C(13)-C(20)}$	1.422(3)	1.418	1.401
$R_{C(13)-C(14)}$	1.478(3)	1.474	1.489
$R_{C(14)-C(15)}$	1.404(3)	1.418	1.400
$R_{C(15)-C(16)}$	1.473(3)	1.465	1.476
$R_{C(16)-C(19)}$	1.428(3)	1.439	1.445
$R_{C(17)-C(18)}$	1.416(3)	1.434	1.412
$R_{C(19)-C(20)}$	1.456(4)	1.465	1.480

Table 6.5 is continued on the next page.

the average difference is 0.50 ± 0.17 deg. The worst agreement between B3LYP and

Table 6.5. (*continued*)

	X-ray	B3LYP/6-31G(d,p)	LMP2/6-31G(d,p)
angles			
∠ C(19)N(1)C(18)	116.8(2)	117.9	116.9
∠ C(16)N(2)C(17)	116.7(19)	117.9	117.0
∠ C(2)C(1)C(20)	121.8(3)	120.8	120.6
∠ C(2)C(1)C(1)	123.1(18)	121.3	121.3
∠ C(20)C(1)H(1)	115.2(19)	117.9	118.2
∠ C(1)C(2)C(3)	119.8(3)	119.5	119.5
∠ C(1)C(2)H(2)	120.0(18)	120.2	120.3
∠ C(3)C(2)C(2)	119.8(17)	120.3	120.2
∠ C(2)C(3)C(4)	119.7(3)	120.3	120.2
∠ C(2)C(3)H(3)	120.6(13)	120.1	120.1
∠ C(4)C(3)H(3)	119.7(13)	119.6	119.7
∠ C(13)C(4)C(3)	121.6(3)	121.4	121.2
∠ C(13)C(4)C(4)	120.7(17)	120.1	120.3
∠ C(3)H(4)H(4)	117.7(17)	118.4	118.4
∠ C(6)C(5)C(14)	120.8(2)	121.4	121.2
∠ C(6)C(5)H(5)	118.3(13)	118.4	118.5
∠ C(14)C(5)H(5)	120.9(13)	120.1	120.3
∠ C(5)C(6)C(7)	120.8(2)	120.3	120.2
∠ C(5)C(6)H(6)	119.4(18)	119.6	119.7
∠ C(7)C(6)H(6)	119.6(18)	120.1	120.1
∠ C(8)C(7)C(6)	119.7(2)	119.5	119.5
∠ C(8)C(7)H(7)	119.5(16)	120.2	120.3
∠ C(6)C(7)H(7)	120.7(16)	120.3	120.2
∠ C(7)C(8)C(15)	120.5(2)	120.8	120.5
∠ C(7)C(8)H(8)	119.8(13)	121.3	121.3
∠ C(15)C(8)H(8)	119.5(13)	117.9	118.2
∠ C(10)C(9)C(17)	120.1(2)	119.9	119.8
∠ C(10)C(9)H(9)	120.9(16)	122.1	122.2
∠ C(17)C(9)H(9)	118.9(16)	117.9	118.0
∠ C(9)C(10)C(11)	120.4(2)	120.7	120.5
∠ C(9)C(10)H(10)	122.4(14)	120.0	120.1
∠ C(11)C(10)H(10)	117.3(14)	119.3	119.3

Table 6.5 is continued on the next page.

experimental results is found in the case of C-N-C angles, while the LMP2 calculation gives better agreement with experiment. A difference of three degrees between experimental and

Table 6.5. *(continued)*

	X-ray	B3LYP/6-31G(d,p)	LMP2/6-31G(d,p)
∠ C(12)C(11)C(10)	121.1(2)	120.7	120.6
∠ C(12)C(11)H(11)	119.7(17)	120.0	120.1
∠ C(10)C(11)H(11)	119.2(17)	119.3	119.3
∠ C(11)C(12)C(18)	119.9(2)	119.9	119.8
∠ C(11)C(12)H(12)	123.9(15)	122.1	122.2
∠ C(18)C(12)H(12)	116.3(15)	117.9	118.0
∠ C(41)C(3)C(20)	118.4(2)	117.8	118.1
∠ C(4)C(13)C(14)	122.3(2)	122.1	121.7
∠ C(20)C(13)C(14)	119.3(2)	120.1	120.2
∠ C(15)C(14)C(5)	118.2(2)	117.8	118.1
∠ C(15)C(14)C(13)	120.5(2)	120.1	120.1
∠ C(5)C(14)C(13)	121.3(2)	122.1	121.8
∠ C(14)C(15)C(8)	120.0(2)	120.2	120.5
∠ C(14)C(15)C(16)	120.1(2)	120.1	120.5
∠ C(8)C(15)C(16)	119.8(2)	119.7	119.0
∠ N(2)C(16)C(19)	122.4(2)	121.3	121.7
∠ N(2)C(16)C(15)	118.1(2)	118.9	118.9
∠ C(19)C(16)C(15)	119.4(2)	119.8	119.4
∠ N(2)C(17)C(18)	120.8(2)	120.8	121.3
∠ N(2)C(17)C(9)	119.3(2)	119.8	119.0
∠ C(18)C(17)C(9)	119.9(2)	119.3	119.7
∠ N(1)C(18)C(17)	122.1(2)	120.8	121.3
∠ N(1)C(18)C(12)	119.3(2)	119.8	119.0
∠ C(17)C(18)C(12)	118.6(2)	119.3	119.7
∠ N(1)C(19)C(16)	121.1(2)	121.3	121.8
∠ N(1)C(19)C(20)	118.5(2)	118.9	118.9
∠ C(16)C(19)C(20)	120.3(2)	119.8	119.3
∠ C(1)C(20)C(13)	118.8(2)	120.2	120.5
∠ C(1)C(20)C(19)	121.0(2)	119.7	119.0
∠ C(13)C(20)C(19)	120.2(2)	120.1	120.5

calculated values is found for the C(20)C(1)H(1) angle. Once again, the exact experimental positions of hydrogen atoms are not known, which may explain the apparent differences between calculated and experimental values. Moreover, according to the calculation DBP is planar, while the crystal structure shows that it is slightly nonplanar with C(1) and H(1) atoms placed above the molecular plane. There are no significant differences between B3LYP and LMP2 angle calculations, although LMP2 results are in a slightly better

agreement with experimental values.

Conclusion

DBP crystallizes in an orthorhombic $P2_12_12_1$ space group and exhibits an SHB-type structure. The presence of nitrogen lone pairs yields a different arrangement of molecules in a unit cell from that observed in the case of other policyclic aromatic compounds. There is little difference in the results obtained from B3LYP and LMP2 calculations; the DFT method, however, requires less computer time, and was used successfully in my thesis work. Calculated B3LYP and LMP2 bond lengths and angles are in excellent agreement with the experimentally observed values. Therefore, disagreements between experimental and calculated values of reorganization energies in Chapters 2 and 3 likely are not attributable to inaccurate optimized geometries; rather, they must be associated with the problems of calculating single point energies for the open shell systems.[2]

References

(1) (a) Amashukeli, X; Winkler, J. R.; Gray, H. B.; Gruhn, N. E.; Lichtenberger, D. L. *J. Phys. Chem.* **2002**, in press. (b) Amashukeli, X; Gray, H. B.; Gruhn, N. E.; Lichtenberger, D. L. in preparation.

(2) Labanowski, J. K.; Andzelm, J. W. *Density Functional Methods in Chemistry*; Springer-Verlag: New York, **1991**.

(3) Balzani, V., Ed. *Electron Transfer in Chemistry*; Wiley-VCH Verlang GmbH: D-69469 Weinheim, Germany, **2001**; Vols. 1-5.

(4) Shelderick G. M. *SHELXS-97;* University of Göttingen: Germany **1997**.

(5) Shelderick G. M. *SHELXL-97;* University of Göttingen: Germany **1997**.

(6) Jaguar version 3.5, Schrödinger Inc.: Portland, OR, **1999**.

(7) Becke, A.D. *J. Chem. Phys.* **1993**, *98*, 5648-5652.

(8) Lee, C.; Yang, W.; Parr, R. G.; *Phys. Rev.* **1988**, *B37*, 785-789.

(9) Becke, A. D. *J. Chem. Phys.* **1988**, *88*, 1053-1062.

(10) Kohn, W.; Sham, L. J. *Phys. Rev.* **1965**, *A137*, 1617-1620.

(11) Møller, C.; Plesset, M. S. *Phys. Rev.* **1934**, *46*, 618-622.

(12) (a) Desiraju, G. R.; Gavezzotti, A. *J. Chem. Soc., Chem. Commun.* **1989**, 621-623; (b) Gavezzotti, A.; Desiraju, G. R. *Acta Cryst.* **1988**, *B44*, 427-434.

(13) Kiralj, R.; Kojić-Prodić, B.; Piantanida, I.; Žinić, M. *Acta Cryst.* **1999**, *B55*, 55-69.

(14) Bacon, G. E.; Curry, N. A.; Wilson, S. A. *Proc. R. Soc. London Ser.* **1964**, *A279*, 98-110.

(15) Brock, C. P.; Dunitz, J. D. *Acta Cryst.* **1982**, *B38*, 2218-2228.

(16) Hazell, A. C.; Larsen, F. K.; Lehmann, M. S. *Acta Cryst.* **1972**, *B28*, 2977-2984.

(17) Roberts, P. J.; Ferguson, G. *Acta Cryst.* **1977**, *B33*, 1244-1247.

(18) Fawcett, J. K.; Trotter, J. *Proc. R. Soc. London Ser.* **1965**, *A289*, 366-376

(19) White, J. G. *J. Chem. Soc.* **1948**, 1398-1408.

(20) Woźniak, K.; Kariuki, B.; Jones, W. *Acta Cryst.* **1991**, *C47*, 1113-1114.

(21) Herbstein, F. H.; Schmidt, G. M. J. *Acta Cryst.* **1955**, *8*, 399-405.